Ultrawide Bandgap Ferroelectric Scandium Aluminum Nitride: Epitaxy, Characterization, and Emerging Device Applications

by

Jiangnan Liu

A dissertation submitted in partial fulfillment
of the requirements for the degree of
Doctor of Philosophy
(Electrical and Computer Engineering)
in the University of Michigan
2026

Doctoral Committee:

Professor Zetian Mi, Chair
Associate Professor John Heron
Professor Mackillo Kira
Professor Di Liang
Associate Professor Zheshen Zhang

Jiangnan Liu

liujn@umich.edu

ORCID iD: 0000-0002-1763-7302

© Jiangnan Liu 2026

Acknowledgements

I would like to first express my deep gratitude to my PhD advisor, Professor Zetian Mi, for his endless guidance and support throughout my doctoral study. His sharp scientific insight, encouragement to move one step forward, and the high standards for research have greatly shaped my development as a researcher. Challenges are one of the nature of research, and there were time when I was struggling with the projects. However, Professor Mi always shows great support through these times by encouraging me to develop independent thinking while having in-depth discussions to go through the details whenever needed. All these discussions have equipped me with a better understanding of the field, from materials growths to device physics.

I also thank my committee members, who are also great collaborators throughout the past years, Professor Mack Kira, Professor Di Liang, Professor Zheshen Zhang, and Professor John Heron, for providing valuable feedback and thorough evaluation of this dissertation to help strengthen the depth of the studies. Beyond this, we had lots of great discussions on the projects, and I learned a lot in diverse fields from these experts.

When I started my PhD, I was very fortunate to have several great mentors, Dr. Walter Shin, Dr. Ping Wang, Dr. Ding Wang, and Dr. Yuanpeng Wu. They were so experienced and knowledgeable that I can quickly get familiar with the III-nitrides growth and fabrication. Every time I went to them to ask questions or for help, they were always supportive and gave great suggestions, and this also shaped me as a mentor when I became more senior in the group. I also appreciate all the current and past Mi group members, Dr. Xianhe Liu, Dr. David Laleyan, Dr. Danhao Wang, Dr. Huabin Yu, Dr. Yakshita Malhotra, Dr. Ayush Pandey, Dr. Ishitiaque Navid, Dr. Jungwook Min, Dr. Reddeppa Maddaka, Dr. Peng Zhou, Dr. Bingxing Zhang, Dr. Kejian Li, Dr. Zhengwei Ye, Dr. Jie Zhang, Dr. Md Tanvir Hasan, Dr. Shubham Mondal, Dr. Yixin Xiao, Dr. Songtao Tang, Abdur-Raheem Al-Hallak, Yifu Guo, Yuyang Pan, Md Mehedi Hasan Tanim, Samuel Yang, Yiran Li, Mingtao Hu, Rui Xu, Yu Zheng, Rui Shen, Yuanxiang Xu, Minming He, Huiyun Yang, Dalei Jiang, Yuyang Chen and Shiyu Zhang for the support in both research work

and personal life during my PhD life. Thanks to all the fellows, I had a really good time working with you.

This dissertation covers a wide range of topics from materials to photonic and electronic applications, and it would be impossible to finish these works without the great teamwork with the amazing collaborators from both UofM and other universities/institutions, including Dr. You Wu, Dr. Matthias Florin, Dr. Cody Patterson, Dr. Qiannan Wen and Dr. Weiwei Jiang from Prof. Mack Kira's group, Dr. Shuai Liu, Dr. Kareem Hariri and Yuheng Zhang from Prof. Zheshen Zhang's group. Dr. Omar Al-Khazragy, Dr. Mengyue Xu, Minming He, Yang Lan from Prof. Di Liang's group, Pat Kezer from Prof. John Heron's group, Jason Manasa and Jeremy Shen from Prof. Robert Hovden's group, Wenhao Peng and Hersh Desai from Prof. Amir Mortazawi's group, Kelotchi Figueroa Nieves, Akosua Boampong, Alexander McFarland, Yuchen Kan and Zhaohan Jiang from Prof. Parag Deotare's group, Dr. Suhan Son and Dr. Chuangtang Wang from Prof. Liuyan Zhao's group, Dr. Yuan Xu and Prof. Nanfang Yu from Columbia University, Dr. Mo Soltani and Dr. Anshuman Singh from Raytheon BBN Technologies, Pierre-Luc Thériault and Prof. Stéphane Kéna-Cohen from Polytechnique Montréal, Dr. Andrew Allerman, Dr. Andy Michael Armstrong and Dr. Brianna Alexandra Klein from Sandia National Lab, Ye Lin, Xiaotong Xu, Junhao Lin and Dr. Hanwool Lee from University of Illinois, Urbana-Champaign, Dr. Heng Zhang, Dr. Tasos Koulouklidis, Simon Anglhuber and Prof. Rupert Huber from University of Regensburg, Dr. Junn Keat and Prof. Michael Johnston from University of Oxford, Dr. John Niroula, Patrick Darmawi-Iskandar and Prof. Tomás Palacios from Massachusetts Institute of Technology, Haochen Wang, Prof. Chris G. Van de Walle from University of California, Santa Barbara, among many other fantastic collaborators.

I also acknowledge the staff at the facilities at the University of Michigan, including Dr. Sandrine Martin, Dr. Vishva Ray, Tony Sebastian, Brian Armstrong, Jorge Barreda, Terre Briggs, Jeremey Schwartz, Shawn Wright, Katharine Beach, Casey Jackson, Svetlana Kiriushechkina, Myles McKenna, Dr. Robert Nidetz and Matthew Oonk from Lurie Nanofabrication Facility (LNF) and Dr. Kai Sun, Dr. Haiping Sun and Dr. Tao Ma from Michigan Center for Materials Characterization (MC^2). Also, a special thanks to the magic Dennis Schweiger from LNF, who always has a great solution when we get stuck with any hardware.

I have also been fortunate to take courses with many great professors such as Prof. Zhaohui Zhong, Prof. Jay Guo, Prof. Elaheh Ahmadi, Prof. Pallab Bhattacharya, Prof. Xudong Fan, Prof.

Max Shtein and Prof. Fred Terry, from whom I not only have broadened my knowledge, but also have learned how to be a good instructor.

I would also like to thank the staff from the ECE department, Kristen Fenton, Trasa Burkhardt, Hannah Wiles, Mackenzie Smith, Lisa Armstrong, Jeffrey Horosko, Catharine June, Michael Lee, Mark Schefer, Ann Stals and Alexandra Thebaud, who provided lots of help throughout my PhD life.

Finally, I want to express my gratitude to my family, for their endless and selfless help and encouragement throughout my life and constant support as well as understanding with all my decisions. I am also grateful to my friends for their companion and help in different stages of my life. It has always been a great pleasure to meet all of you.

Table of Contents

Acknowledgements ii

List of Tables ix

List of Figures x

Abstract xvii

Chapter 1 Introduction 1

1.1 III-nitride semiconductors 1

1.1.1 Bandgaps of III-nitride 1

1.1.2 Crystal structure of III-nitrides 2

1.1.3 Polarizations in III-nitride 3

1.2 Scandium-doped Aluminum Nitride (ScAlN) 5

1.2.1 Ferroelectricity in ScAlN 5

1.2.2 Enhanced Second-order Nonlinearity in ScAlN 10

1.3 Dissertation Overview 12

Chapter 2 Native Oxynitride Layer-Assisted Leakage Current Suppression and Coercive Field Reduction in Nitride Ferroelectrics 15

2.1 Introduction 15

2.2 ScAlN Growth and Device Characterization Technique 16

2.3 Device Applications with Oxynitride Layer Incorporation 22

2.4 Conclusion 25

Chapter 3 Impact of Scandium Doping on the Second-order Optical Nonlinearity in Epitaxial Aluminum Nitride 26

3.1 Introduction 26

3.2 Epitaxial Growth of ScAlN 27
3.3 Second-order Optical Nonlinear Characterization of ScAlN 29
3.4 Conclusion 34
Chapter 4 Second-order Optical Nonlinearity in Scandium-doped Gallium Nitride 35
4.1 Introduction 35
4.2 Epitaxial Growth of ScGaN 36
4.3 Optical Bandgap Characterization of ScGaN 37
4.4 Second-order Optical Nonlinear Characterization of ScGaN 38
4.5 Conclusion 39
Chapter 5 Hybrid ScAlN/Si_3N_4 Platform for Low-Loss Integrated Photonics 40
5.1 Introduction 40
5.2 Materials Growth and Characterizations 42
5.3 Device Design and Numerical Simulation 43
5.4 Device Fabrication and Measurements 45
5.5 Conclusion 51
Chapter 6 Low Sheet Resistance ScAlN/GaN Heterostructures for High-performance Electronics 52
6.1 Introduction 52
6.2 Heterostructure Growth and Characterizations 54
6.3 Hall Measurement at Room Temperature 56
6.4 Temperature-dependent Hall Measurement 58
6.5 Band Diagram Simulations 59
6.6 Conclusion 60
Chapter 7 High-temperature Stable ScAlN/GaN High-Electron Mobility Transistors 62
7.1 Introduction 62
7.2 High Current ScAlN/GaN HEMTs Fabrication 63

7.3 Temperature-Dependent Device Characterizations 64

7.4 Conclusion 68

Chapter 8 High-Temperature Memory Devices Based on Ferroelectric ScAlN/AlGaN/GaN HEMTs 69

8.1 Introduction 69

8.2 Fabrication of Ferroelectric ScAlN/AlGaN/GaN HEMTs 71

8.3 Operational Principle of Ferroelectric ScAlN/AlGaN/GaN HEMTs 73

8.4 Memory Performance of Ferroelectric HEMTs under High Temperature 77

8.5 Multi-Bit Capacity of Ferroelectric ScAlN/AlGaN/GaN HEMTs 79

8.6 Conclusion 82

Chapter 9 E-mode GaN HEMT with ScAlN/ScN Charge Trap-Coupled Ferroelectric Gate Stacks 83

9.1 Introduction 83

9.2 E-mode GaN HEMT Device Structure and Fabrication 85

9.3 Operation Switching from D-mode to E-mode 86

9.4 E-mode Stability Testing 88

9.5 Conclusion 90

Chapter 10 Ferroelectric ScAlN coupled Al-rich AlGaN-channel HEMT 92

10.1 Introduction 92

10.2 Integration of Ferroelectric ScAlN to $Al_{0.50}Ga_{0.50}N$-channel HEMT 94

10.3 Device Characterization 96

10.4 Conclusion 100

Chapter 11 Summary and Outlook 101

11.1 Summary 101

11.2 Future Works 102

11.2.1 Sc-rich ScAlN Epitaxy with low loss 102

11.2.2 Novel Rare-earth Dopants to III-nitrides 103

11.2.3 Quantum Engineering in ScAlN 103

11.2.4 Improved Device Performance of ScAlN/GaN HEMTs 104

11.2.5 Contact Resistance Reduction by Contact Engineering in AlGaN-channel HEMTs 104

Bibliography 106

List of Tables

Table 1.1: Lattice parameters a, c and u of AlN, GaN and InN.[13, 14] 3

Table 1.2 Spontaneous polarization (P_{SP}), piezoelectric coefficients (e_{ij}) and elastic constants C_{ij} of wurtzite AlN, GaN and InN.[15] 4

Table 1.3: Ferroelectric characteristics comparison between ScAlN and HfO_2, BTO and PZT. Data from [40-43]. 10

Table 3.1: Refractive index of ScAlN at varying scandium concentrations. The data is given at the second harmonic wavelength (λ = 633 nm) and pump wavelength (λ = 1266 nm). 30

Table 3.2: d_{31} and d_{33} values of ScAlN and their ratios to AlN at varying scandium concentrations. 32

Table 5.1: Confinement Factors for Fundamental TE and TM Modes. 45

List of Figures

Figure 1.1 Energy bandgap and lattice constants of the III-nitride alloys [8]. 2

Figure 1.2 Crystal structure illustration of (a) hexagonal close-packed [11], and (b) wurtzite lattices [12]..... 2

Figure 1.3 Schematic of the free energy F as a function of the polarization P of (a) paraelectric materials with a parabola shape and (b) ferroelectric materials with a double well separated by the energy barrier ΔE. 6

Figure 1.4: (a) Structural illustration of the ScAlN with different polarization states of wurtzite metal-polar, wurtzite nitrogen-polar and non-polar layered hexagonal.[21] (b) Theoretical calculations on energy per formula unit as a function of polarization at 300 K, and (c) switching barrier height at 0 K and 300 K for Sc doping levels from 5% to 20%.[33] 8

Figure 1.5: MBE-grown (Sc)AlN samples characterizations. (a) XRD 2θ-ω scan of with ScAlN (002) peaks next to the AlN peaks around 36°. (b) Atomic-force microscopy images showing roughness < 1 nm.[35] 9

Figure 1.6: Illustration of the second-order optical nonlinear processes of (a) SHG, (b) SFG, and (c) DFG. Two horizontal lines represent the energy levels, and the length of arrow is proportional to the photon energy..... 11

Figure 2.1: (a) Schematic of the native oxynitride layer etching process upon contact with TMAH developer. (b) XRD 2θ scans of surface-protected and surface-damaged samples, along with the GaN substrate. (c) XPS survey spectrum of the samples. (d) High-resolution XPS spectra of the Al 2p core level. (e, f) SEM, AFM images of the surface-damaged (e) and surface-protected samples (f)..... 18

Figure 2.2: Schematic of the memristor fabrication processes. (a) Without PMMA protection. (b) With PMMA protection. 19

Figure 2.3: Ferroelectric properties of ScAlN capacitors. (a) *J-E* loops measured by a triangular waveform with 10 ms period at ±65 V maximum bias. (b) Coercive field of surface-protected and surface-damaged devices extracted from *J-E* loops. (c) Comparison of leakage current density at the coercive field extracted from AC *J-E* loops for MBE-grown ScAlN. (d) Typical butterfly *C-V* curves measured at 2 MHz. (e) Electric-field-dependent PUND measurements. (f) Representative *P-E* loops measured at 12.5 kHz. (g) Transient PUND results measured with pulse width of 0.025 ms. (h) Representative *I-V* curves recorded after negative or positive poling. (i) Comparison of V_{BD}/V_{SW} and E_c performance with other MBE-grown ScAlN memristors. 20

Figure 2.4: (a) Schematic illustration of the ferroelectric capacitor. (b) STEM and corresponding EDS element mappings of the ScAlN/GaN heterostructure. (c) Quasi-static *I-V* measurements of surface-protected and surface-damaged devices. (d) Poole-Frenkel fitting of the negative-bias OFF state data from (c). (e) Schematic of a biological synapse. (f) Potentiation and depression behavior of the conductance in response to different electrical pulses, analogous to synaptic plasticity. (g) Hardware neural network configuration using ScAlN memristors for fully connected layers. (h) Schematic of the VGG-8 network architecture used for CIFAR classification and synaptic weight emulation. (i) Comparison of test accuracy on the CIFAR dataset using ScAlN capacitors with linear and nonlinear properties, alongside an ideal device. 24

Figure 3.1: (a) Illustration of the structure of the measured samples. ScAlN with 10%, 20% and 30% Sc concentration grown on sapphire wafers with a thin AlN buffer layer. (b) Atomic force microscopy image scanning the surface of the $Sc_{0.20}Al_{0.80}N$ with surface roughness 1.5 nm. (c) X-ray diffraction pattern of AlN and $Sc_{0.20}Al_{0.80}N$ thin film with AlN buffer layer. (d) The cross-sectional transmission electron microscopy characterization on the single crystalline ScAlN film. 29

Figure 3.2: (a) Experimental setup for measuring the second-order nonlinear optical response of the samples. The setup includes a half-wave plate ($\lambda/2$) to control the polarization of the incident light, lenses to focus and collimate the beam, shortpass filters to remove the fundamental frequency, a linear polarizer to analyze the polarization of the second harmonic signal, and a detector to measure the SHG intensity..... 29

Figure 3.3: (a) Generated second harmonic pulses energy as a function the pump pulses energy for films of different concentrations. The values of the fitted slopes (Δ) are very close to the theoretical values of 2 for the second harmonic generation. Second-harmonic generation polarimetry data for different Sc concentration for TM (b) and TE (c) polarizations with a pump wavelength of 1266 nm and an incidence angle of 60 degrees. For comparison purposes, these plots are normalized to show the amplitude of the SHG electric field divided by the square of the incident electric field and the ScAlN film thickness. The solid lines correspond to the nonlinear transfer matrix fits..... 31

Figure 3.4: Dependence of the second-order nonlinear coefficients d_{ij} of ScAlN on scandium concentration. The red triangle and blue square symbols represent the value of the d_{31} and d_{33} nonlinear coefficient respectively. The values are obtained by averaging over multiple measurements. The error bars show the standard deviation. Note that the error bars for d_{31} are smaller than the markers. 32

Figure 3.5: (a) TM-polarized and (b) TE-polarized second-harmonic generation polarimetry data for films grown on different substrates and measured in reflection configuration. The film grown directly on Si with 30% Sc content in this comparison (red marker) was grown by sputtering. The incidence angle for these measurements was 67.5 degrees. The data represents the amplitude of the electric field at the second-harmonic frequency normalized by the square of the incident electric field and the ScAlN film thickness. The solid lines represent the fitted patterns. The strength of the signal cannot be directly interpreted in terms of the strength of the nonlinearity because of the different reflectivity of Al and Si. (c) d_{31} and (d) d_{33} coefficients for films with different substrates. The values represent the average extracted nonlinear coefficients for

multiple measurements and the error bar represents the standard deviation of the extracted values. The error bars are smaller than the markers for d_{31}. 34

Figure 4.1: (a) Structural illustration of the epitaxial ScGaN/AlN on sapphire used in this study. (b) X-ray diffraction pattern on the 2θ-ω scan on the grown samples with Sc compositions of 20%, 30% and 40%. 37

Figure 4.2: Extracted optical bandgap E_g with 10%- 40% Sc incorporation. 38

Figure 4.3: (a) Extracted d_{31}, and (b) d_{33} values in ScGaN with Sc composition up to 35%. 39

Figure 5.1: Materials characterization of ScAlN. (a) Crystal structure illustration of Sc-alloyed AlN. (b) Atomic force microscope imaging of the ScAlN surface showing a roughness of 1.2 nm. (c) Cross-sectional STEM and EDS mappings of the Si_3N_4/ScAlN/AlN/Sapphire structure. 43

Figure 5.2: Waveguide design and simulated optical characteristics. (a) Geometry and dimensions for Si_3N_4-ScAlN hybrid guiding structure. Fundamental TE_{00} (b) and TM_{00} (c) mode distributions (|E|) in a ring configuration. (d) Group index (n_g) for the modes shown in (b) and (c). Bending loss (e) and confinement factor within ScAlN (f) for the TE_{00} mode with respect to bending radius for different thicknesses of Si_3N_4 at a guide width of 2.8 μm. 44

Figure 5.3: Fabrication of the Si_3N_4–ScAlN photonic chips. (a) Fabrication flow of the monolithically integrated Si_3N_4-ScAlN waveguides. (b) False-colored scanning electron microscopy (SEM) image of the device after Si_3N_4 etching showing a smooth sidewall. (c) False-colored cross-sectional SEM of the fabricated waveguide. 46

Figure 5.4: Optical loss characterization of the circular microring resonator. (a) Microscope image of the fabricated Si_3N_4-ScAlN microring resonator ($R = 200\ \mu$m, $w_B = 2.8\ \mu$m). (Scale bar) (b) Normalized transmission spectrum for TE polarization for 1550 to 1630 nm. Fitted highest Q_i resonances for TE (c) and TM (f) polarizations, with $Q_i = 3.02 \times 10^5$ and $Q_i = 2.85 \times 10^5$ corresponding to propagation losses of $\alpha = 1.16$ dB/cm and $\alpha = 1.23$ dB/cm respectively. Fitted Q_i trend with wavelength for TE (d) and TM (g) polarizations. Fitted Q_i distributions for TE (e) and TM (h) polarizations. 47

Figure 5.5: Optical loss characterization of the Euler racetrack microring resonator. (a) Normalized transmission spectrum from 1590 nm to 1630 nm for TE polarization, with highest Q_i resonance highlighted and Euler-bend racetrack resonator ($R_{eff} = 125\ \mu$m, $w = 2.6\ \mu$m) inset. (b) Fitted highest intrinsic quality factor resonance for TE polarization, with $Q_i = 3.35 \times 10^5$ corresponding to a propagation loss of $\alpha = 1.03$ dB/cm. Dots: experiment data. Solid line: fitting. (c) Fitted Q_i trend with wavelength for TE polarization. (d) Fitted Q_i distribution for TE polarization. 49

Figure 5.6: Benchmarking of intrinsic quality factors. Comparison of the intrinsic quality factor of the hybrid ScAlN/Si_3N_4 microring demonstrated in this work with other reported monolithic ScAlN resonators of various Sc compositions. 50

Figure 6.1: (a) Illustration of the grown GaN/ScAlN/AlN/GaN sample structure with varying $Sc_{0.15}Al_{0.85}N$ thicknesses of 0, 4, 12, 15 and 24 nm. (b) Atomic force microscopy image of the

heterostructure with 24 nm ScAlN barrier showing rms roughness 1.4 nm. The height color bar is 6 nm. (c) X-Ray diffraction pattern of the 2θ–ω scan on the heterostructure showing (002) peaks of GaN substrate and the epitaxial ScAlN barrier. (d) The XRD rocking curve scan on the ScAlN (002) peak with 370 arcsec linewidth. (e) Transmission electron microscope imaging on the all-epitaxial ScAlN barrier/AlN interlayer/GaN channel grown by MBE with atomically sharp and clear interface. 55

Figure 6.2: The Hall measurement with van der Pauw configuration on epitaxial GaN/ScAlN/AlN/GaN HEMT samples. (a) Electron carrier mobility. (b) 2DEG sheet carrier density. (c) Sheet resistance of different ScAlN barrier thicknesses. Open circles in (b) represents a separate batch of samples with varying ScAlN barrier thicknesses. 57

Figure 6.3:The temperature-dependent Hall measurement with Ti/Au contact on the HEMT structure with 15 nm $Sc_{0.15}Al_{0.85}N$ barrier. (a) Electron mobility. (b) 2DEG sheet carrier density. (c) Sheet resistance in the temperature range of 10 K to 300 K. 59

Figure 6.4: Calculation results by solving Schrödinger and Poisson equations self-consistently. (a) Band diagram of the GaN/ScAlN/AlN/GaN with the electron wavefunction plotted within the well. (b) Extracted 2DEG carrier density by integrating the carrier distribution, showing the 2DEG density can reach more than 7×10^{13} cm^{-2} when ScAlN barrier is thick enough. 60

Figure 6.5: Benchmark of sheet carrier concentration n_s and electron mobility of this work with other reported ScAlN/GaN heterostructure data with sheet resistance contour line labeled. 61

Figure 7.1: (a) Schematic illustration of ScAlN/GaN HEMT. (b) The fabrication process flow. (c) Current-voltage characteristics of different distances on TLM pattern. (d) Resistance versus distance curves at RT. 64

Figure 7.2: Drain current density, I_D versus drain-to-source voltage, V_{DS} characteristic curves of a device were measured by varying gate-to-source voltages, V_{GS} from -15 V (off-state) to 1 V (on-state) in -2 V increments at (a) RT and (b) 700 K. The on-resistances, R_{on} of 1.48 Ω·mm and 4.17 Ω·mm were measured at V_{GS} = 1 V for device tested at RT and 700 K, respectively. (c) Transfer curve in log-scale (black curve) and gate-leakage current (red curve) were measured at a fixed V_{DS} = 5 V. (d) Transfer (in linear scale, black curve) and transconductance, g_m characteristic curves (red curve) measured at RT and 700 K. 66

Figure 7.3: (a) Benchmarking of temperature-dependent normalized drain current of our proposed device with those published and commercially available wide-bandgap transistors. (b) Benchmarking of saturation drain current density as a function of temperature range 573 to 700 K..... 67

Figure 7.4: (a) Variations in g_{mpeak} and R_{on} with temperature. (b) Variations in sheet carrier, n_{2DEG}, 2DEG mobility, μ and sheet resistance, R_{Sh} with temperature measured using the van der Pauw method..... 68

Figure 8.1: Illustration of ferroelectric ScAlN/ AlGaN/GaN HEMTs (a) Schematic of the ferroelectric ScAlN/AlGaN/ GaN HEMT. (b) False-color tilted SEM image of the fabricated ScAlN/AlGaN/GaN HEMTs, showing GaN regrowth contacts and a gate length (L_G) of 1 μm.

(c) Cross-sectional HAADF image and corresponding EDS element maps of the Au/Ni/ScAlN/ AlGaN/GaN gate stack after high-temperature operation at 350 °C, revealing the thickness of each layer and uniform element distribution. (d) High-resolution HAADF-STEM images of the ScAlN/AlGaN and AlGaN/GaN interfaces after operation at 350 °C, revealing well-defined, high quality interfaces with atomic-scale resolution. 72

Figure 8.2: Electrical performance of a representative ferroelectric ScAlN/AlGaN/GaN HEMT at room temperature (a–c) Semi-logarithmic transfer characteristics under various bias conditions: (a) fixed V_{DS} of 0.5 V with $V_{GS,END}$, defined as the final V_{GS} value at the end of the voltage sweep, varying from − 1 to +7 V; (b) fixed V_{DS} of 5 V with $V_{GS,END}$ ranging from − 1 to +7 V; and (c) varying V_{DS} from 0.1 to 10.1 V with a fixed $V_{GS,END}$ of +7 V. (d) Dependence of the memory window (MW) on V_{DS} and V_{GS}, showing stable and large MWs of ∼4 V. (e and f) Subthreshold swing (*SS*) as a function of V_{DS} and V_{GS} during (e) forward sweep and (f) backward sweep. Sub-60 mV/dec SS is achieved during the backward sweep, attributed to the ferroelectric switching of ScAlN. (g) Semi-logarithmic double-sweep transfer characteristics under various VDS, demonstrating a high I_{on}/I_{off} ratio exceeding 108 across a wide range of V_{DS}. (h and i) Output characteristics under different V_{GS} poling: (h) V_{GS} from − 2 to +7 V and (I) V_{GS} from +7 to − 2 V. 76

Figure 8.3: Memory performance of a representative ferroelectric ScAlN/AlGaN/GaN HEMT at room temperature and a high temperature of 250 °C (a) Transfer characteristics of the ScAlN/AlGaN/GaN HEMT with manual DC switching cycles up to 300 cycles at room temperature. (b) Endurance performance at room temperature under manual DC switching. (c) Retention performance at room temperature. (d) Transfer characteristics of the ScAlN/AlGaN/GaN HEMT with manual DC switching cycles up to 100 cycles at 250 °C. (e) Endurance performance at 250 °C. (f) Retention performance at 250 °C. 78

Figure 8.4: Demonstration of the multi-bit capability of the ScAlN/AlGaN/GaN HEMT at room temperature and corresponding energy band diagrams (a) Four distinct current levels obtained by applying different programming gate voltages ($V_{GS,END}$) over 100 cycles of manual DC switching. (b) Distribution of the four well-separated conductance levels over 100 cycles. (c) Energy band diagrams of the ferroelectric ScAlN/AlGaN/GaN HEMT in erase and program states, highlighting nonvolatile modulation of 2DEG density through ferroelectric domain switching in ScAlN 80

Figure 8.5: Benchmarking of the ferroelectric ScAlN/AlGaN/GaN HEMT in this work against recently reported GaN HEMTs and oxide-based FeFETs (a and b) Benchmarks of (a) Ion/Ioff ratio versus *SS* and (b) Ion versus L_G for the ScAlN/AlGaN/GaN HEMT in this work compared to other ferroelectric or ScAlN-containing GaN HEMTs. It is noted that some ScAlN-containing GaN HEMTs do not exhibit ferroelectric hysteresis. (c and d) Benchmarks of (c) *SS* versus I_{on}/I_{off} ratio and (d) MW versus retention for the ScAlN/AlGaN/ GaN HEMT in this work compared to recently reported oxide-based FeFETs. 81

Figure 9.1: (a) Schematic illustration of the ScAlN-gated AlGaN/GaN HEMT with an ultrathin ScN charge trapping layer. (b) Fabrication flow of the AlGaN/GaN HEMT device. (c) TLM measurement results for the AlGaN/GaN 2DEG channel. (d) The counterclockwise *C-V* curve of the ScAlN/ScN/AlGaN/GaN stack confirming the ferroelectricity. (e) Atomic resolution

STEM image showcasing the uniformity of the grown layered material. The structure of each layer in the image matches the expected crystal structure of the material. 86

Figure 9.2: (a) Transfer characteristics of the devices. (b) Extracted V_{th} as a function of the endpoint of forward sweep V_{GS}. 87

Figure 9.3: Schematic band diagram of the HEMT device illustrating the initialization process. (a) during the initialization where V_{GS} is large enough to switch the ScAlN polarization and reduce the barrier height to inject electrons from the 2DEG region into ScN trap layer. (b) V_{GS} withdrawn (= 0 V) after the initialization process and carriers are trapped in the ScN layer due to the switched polarization of ScAlN, lowering the Fermi level to realize a stable E-mode operation. 88

Figure 9.4: Transfer characteristics stability test under a double sweep mode that V_{GS} swept from 0 V to 6 V and back to 0 V with fixed V_{DS} = 10 V. (a) The device experienced 20 cycles of testing after initialization to E-mode operation. (b) The device was tested with waiting time, defined as the time interval between the initialization process and the tests, in a range from 5 seconds to more than 3 days. Insets shown the extracted V_{th} during the stability tests. 89

Figure 9.5: (a-b) Measured output characteristics of the HEMT device with V_{GS} from −2 to 2 V with a 500 mV step (a) before and (b) after the initialization process. (c) Extracted subthreshold slope under various drain current densities. (d) Benchmark plot of *SS* and ON/OFF ratio of our E-mode GaN HEMT with ferroelectric ScAlN gates. 90

Figure 10.1: (a) Schematic illustration of ScAlN/AlGaN HEMT and (b) top-view of SEM image of the proposed device, where the scale bar represents 20 μm. (c) Energy band diagram of the proposed schematic structure with the ground state wave-function illustrated. The solid black curve, dotted green curve, and red dotted curve represent the conduction and valence band energies, Fermi level, and wavefunction, respectively. (d) Illustration of the fabrication process flow. 95

Figure 10.2: (a) Static characteristics of the fabricated ScAlN/AlGaN HEMT at room temperature (RT). (b) Transfer curves (black curve) and gate leakage current (red curve), which were measured at V_{DS} = 5 V. The threshold voltage (V_{th}), defined at 0.01 mA/mm, is represented by the horizontal blue dotted lines. Vertical blue dotted lines are shown to indicate the forward and backward V_{th}. 97

Figure 10.3: (a) Transfer curves for different V_{DS} at RT. Red and black curves represent the transfer curves, which were measured at V_{DS} = 1 and 5 V, respectively. The threshold voltage (V_{th}), defined at 0.01 mA/mm, is represented by the blue dotted line. (b) Subthreshold swing, SS versus drain current density, I_D for both forward and backward gate bias sweeps with different V_{DS}. The V_{GS} step was fixed at 50 mV. The olive dotted line represents the Boltzmann limit. ... 98

Figure 10.4: Transfer characteristics under various (a) V_{GS} steps at 10, 20, 30 and 50 mV, and (b) gate voltage poling paths with the maximum poling voltage $V_{GS,\,max}$ set at –1, 0, 2 and 4 V. 99

Figure 10.5: Variations of drain current (a) and gate leakage current (b) with temperature for different V_{DS}. Red and black curves correspond to measurements performed at V_{DS} = 1 and 5 V, respectively. The on- and off-states are defined for V_{GS} = 1 and −25 V, respectively. 100

Figure 11.1: (a) DFT-calculated Pockels coefficients of ScAlN with various Sc contents. Notably r_{33} can potentially exceeds $LiNbO_3$ at high Sc alloying.[170] (b) SIMS profile of main elements Sc, Al, Ga and impurity elements O and C in the ScAlGaN/GaN multilayer stack, showing 3-4 orders of magnitude lower impurity incorporation than typical ScAlN grown on AlN.[122] ... 103

Abstract

The unique properties of III-nitrides have enabled their diverse applications from LED lighting to high-power and high-frequency electronics. An emerging member in this materials family is scandium aluminum nitride (ScAlN). With controlled Sc incorporation, it maintains non-centrosymmetric wurtzite structure and exhibits dramatically enhanced piezoelectricity, ferroelectricity and optical nonlinearities. Such an enhancement positions ScAlN a compelling platform for next generation filters and sensors for 5G/6G front ends, advanced electronics, and integrated photonics. However, the high-quality growth of ScAlN remains challenging and the device applications remain limited compared with conventional III-nitrides.

The first part of the thesis focuses on the growth of Sc-III-N by molecular beam epitaxy (MBE) and investigation of its fundamental optical properties. A significant enhancement in of second-order nonlinear susceptibility has been revealed with increased Sc concentrations in both AlN and GaN. Furthermore, an ultra-low optical loss hybrid ScAlN/SiN_x photonic platform is demonstrated to extend its applications to quantum photonics. The second part of this thesis exploits the strong polarization of ScAlN, leading to the achievement of record-low sheet resistance in GaN-based high electron mobility transistor (HEMT) structures. Further device demonstrations on the ScAlN-barrier HEMTs unveils its excellent thermal stability in both GaN and AlGaN-channel devices. Finally, a coupled ferroelectric-charge trapping layer (CTL) structure is developed to enable E-mode operations in GaN HEMTs.

Chapter 1 Introduction

1.1 III-nitride semiconductors

Over the past decades, group III-nitrides such as gallium nitride (GaN) and aluminum nitride (AlN), along with their ternary and quaternary alloys including InGaN, InAlN and AlGaN have developed as pivotal semiconductors that support modern optoelectronics, integrated photonics, and high-performance electronics.[1-5] Their wide applications are underpinned with a combination of unique materials properties which will be covered in the following sections.

1.1.1 Bandgaps of III-nitride

One of the critical properties leading III-N a dominant material in light emitting devices such as light-emitting diodes (LEDs) and laser diodes (LDs) is its direct and tunable bandgaps among the binary and alloy compounds. Binary nitrides have a wide energy bandgap range that spans from infrared (IR) of InN (0.7 eV) to ultraviolet (UV) of AlN (6.1 eV),[6, 7] and their alloys can further enable a continuous tuning of the energy bandgap within the entire range through a precise control of the compositions, as shown in Figure 1.1.[8] However, the bandgaps E_g of the alloy compounds do not follow a simple Vegard's law but with a bowing parameter b to compensate the nonlinear relation, as expressed by Eq. 1.1. The bowing parameter for $Al_xGa_{1-x}N$ is generally believed to be a constant of 0.94.[9] However, for In-containing alloys of $In_xGa_{1-x}N$ and $Al_xIn_{1-x}N$, the reported values of b are more scattered and suggesting they are composition-dependent.[10]

$$E_{g,\ A_xB_{1-x}N} = E_{g,\ AN}x + (1-\mathrm{x})E_{g,\ BN} - bx(1-x) \tag{1.1}$$

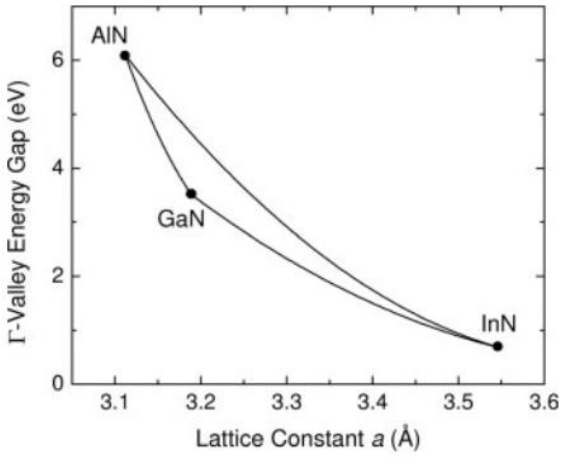


Figure 1.1 Energy bandgap and lattice constants of the III-nitride alloys [8].

1.1.2 Crystal structure of III-nitrides

Most of the III-nitrides tend to crystallize in a wurtzite structure. It can be regarded as a stacking of two hexagonal close-packed (HCP) structures, which is illustrated in Figure 1.2(a).[11] In the interlaced hexagonal lattices, one lattice is composed of group-III elements, including Al, Ga, and In, while the other set of HCP lattice is composed of nitrogen with a separation along the *c*-axis, as shown in Figure 1.2(b).[12] With this structure, one group of atoms are tetrahedrally bonded with the other group of atoms by covalent bond with part of ionicity involved.

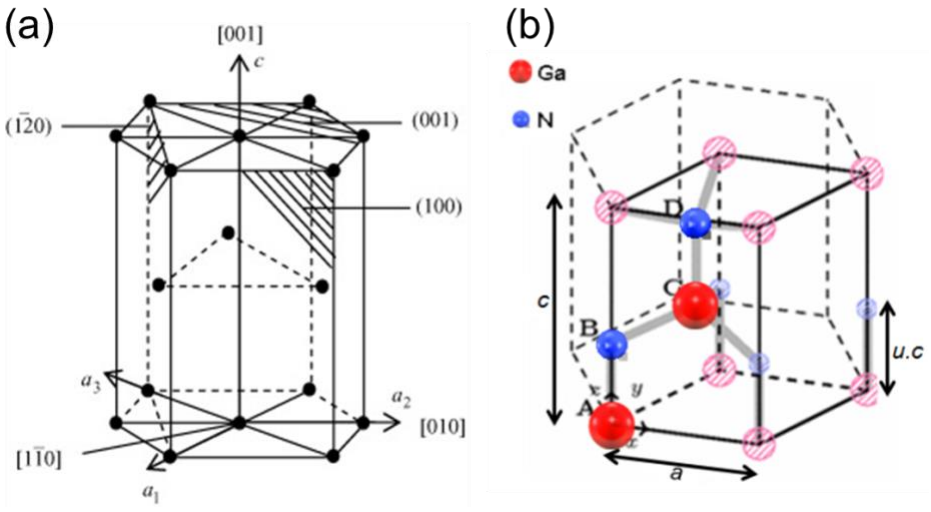


Figure 1.2 Crystal structure illustration of (a) hexagonal close-packed [11], and (b) wurtzite lattices [12].

The wurtzite lattice can be characterized by three crystal parameters: the length between the two hexagonal basal planes (*a*), the distance along the vertical direction (*c*), and the parameter

u that is defined by the ratio of the nearest III-N atoms separation along the *c*-axis to the *c* parameter. The *a*, *c*, and *u* parameters are listed in Table 1.1 and the *a* parameter of the alloys $A_xB_{1-x}N$ can be calculated by the Vegard's law:

$$a_{A_xB_{1-x}N} = a_{AN}x + (1 - x)a_{BN} \quad (1.2)$$

In an ideal tetrahedral arrangement, the *c*/*a* ratio is $\sqrt{\frac{8}{3}} \approx 1.633$. However, for wurtzite III-N, this ratio is less than the ideal value. This deviation further breaks the inversion symmetry and creates a net dipole moment along the stacking *c*-direction.

Table 1.1: Lattice parameters a, c and u of AlN, GaN and InN.[13, 14]

Lattice parameters	AlN	GaN	InN
a (Å)	3.110	3.190	3.544
c (Å)	4.980	5.189	5.718
u	0.3821	0.377	0.379

1.1.3 Polarizations in III-nitride

As discussed in section 1.1.2, the wurtzite structure is composed of an HCP group-III elemental lattice and an HCP nitrogen lattice. Taking GaN as an example, depending on how the two lattices stacked, it can be terminated with either Ga-face or N-face to form Ga-polar and N-polar GaN. The polarity plays another critical role in growth dynamics, surface chemistry, and band alignment, which further affect the performance of nitride-based electronic and photonic devices.

Owing to the non-centrosymmetric structure generated by the deviation from ideal HCP *c*/*a* ratio and the ionicity between the bonds, III-nitrides show a spontaneous polarization (P_{SP}) perpendicular to the *c*-plane with opposite directions for metal-polar and nitrogen-polar materials. Aside from the strong spontaneous polarization, another contribution to the large polarization in the III-nitride heterostructures is the piezoelectric polarization (P_{PE}), which originates from the strain induced by the lattice mismatch between the III-nitrides with different lattice parameters. For example, GaN and AlN have ~2.4% and 4% mismatch along the *a* and *c* directions, respectively, inducing compressed strain in GaN and tensile strain in AlN when forming an AlN/GaN heterostructure. The piezoelectric polarization is defined to be negative for tensile strain

and positive for compressive strain with the direction along the *c*-axis. It can be expressed in Eq. 1.3 as:

$$P_{PE} = e_{31}(\epsilon_1 + \epsilon_2) + e_{33}\epsilon_3 \tag{1.3}$$

where e_{31} and e_{33} are the piezoelectric coefficients and ϵ_i are the strain components, of which can be quantified as:

$$\epsilon_1 = \epsilon_2 = \frac{a_s - a_e}{a_e} \tag{1.4}$$

$$\epsilon_3 = -\frac{2C_{13}}{C_{33}}\epsilon_1 \tag{1.5}$$

where a_s and a_e represents the lattice constant a for substrate and the epitaxial layer on top, respectively and C_{13} and C_{33} are the elastic constants. These parameters are summarized in Table 1.2. The P_{PE} can thus be written as:

$$P_{PE} = 2\left(e_{31} - \frac{C_{13}}{C_{33}}e_{33}\right)\epsilon_1 \tag{1.6}$$

The total polarization is the sum of the two components as expressed in Eq. 1.7, and as will be seen in the following chapters, it is critical for several device applications.

$$P_{tot} = P_{SP} + P_{PE} \tag{1.7}$$

Table 1.2 Spontaneous polarization (P_{SP}), piezoelectric coefficients (e_{ij}) and elastic constants C_{ij} of wurtzite AlN, GaN and InN.[15]

Parameters	AlN	GaN	InN
P_{SP} (C/m^2)	−0.09	−0.034	−0.042
e_{31} (C/m^2)	−0.62	−0.47	−0.45
e_{33} (C/m^2)	1.5	0.81	0.67
C_{11} (GPa)	396	390	223
C_{12} (GPa)	137	145	115
C_{13} (GPa)	108	106	92
C_{33} (GPa)	373	398	224
C_{44} (GPa)	116	105	48

1.2 Scandium-doped Aluminum Nitride (ScAlN)

While GaN, AlN and their alloys largely dominate commercial III-nitride technologies, the composition of the nitride materials is being expanded due to the development of advanced epitaxial techniques. A particular example that draws tremendous attention in the past years is scandium-doped aluminum nitride (ScAlN). Akiyama *et al.* first reported the addition of Sc can reach an order of magnitude increase in the piezoelectric response compared with AlN while the alloys still maintain the wurtzite crystal structure in a certain Sc doping range.[16] This enhancement dramatically improves the electromechanical coupling coefficient, transforming the acoustic micro-electromechanical systems (MEMS), raising the bandwidth and reducing the loss for film bulk acoustic resonators (FBARs) and surface acoustic wave (SAW) filters.[17-20]

The strong enhancement in Sc-doped AlN motivates more studies on its fundamental materials properties and more intriguing characteristics was found including the emergence of ferroelectricity[21, 22] and the improvement on the second-order optical nonlinearities[23], which will be further discussed in this section.

1.2.1 Ferroelectricity in ScAlN

Ferroelectric material is a special group of the pyroelectric material class. Both pyroelectric and ferroelectric materials have permanent spontaneous polarization originating from the non-centrosymmetric structure. However, pyroelectrics have tunable polarizations under temperature variations and the polarization direction in ferroelectric are reversible under the external electric field. Once the polarization is switched, the state will stay robust even without the electric field, provided below the Curie temperature (T_C). The two distinct polarization states enable several unique applications in both electronics and photonics. One example is the ferroelectric random-access memory (FeRAM) that were used in the video games storage and IC cards.[24, 25]

Landau-Devonshire theory has long been successfully used to describe the phase transition from the paraelectric phase to the ferroelectric phase.[26] With the polarization direction being along the *c*-axis in III-nitrides, a one-dimensional (1-D) model can be used to understand the ferroelectric switching in wurtzite ScAlN, where the free energy density F can be expanded to the sixth power term as a function of polarization P as:

$$F_P = \frac{1}{2}aP^2 + \frac{1}{4}bP^4 + \frac{1}{6}cP^6 - EP \tag{1.8}$$

in which a, b, and c are coefficients determined by the ferroelectric crystals. a is a temperature-dependent coefficient that is related to the phase transition temperature (T_0) with the form of $a_0(T - T_0)$. b and c coefficients determine whether the paraelectric-ferroelectric transition is a first-order or a second-order phase transition. EP is the electrostatic term to compensate the materials' response to the applied electric field E.

When the crystal is at a temperature higher than T_0, it behaves as a paraelectric material, stabilizing at a phase with zero polarization. As a result, the free energy density F has a single global minimum at $P = 0$ and the F-P function is parabolic, as illustrated in Figure 1.3(a). As the temperature drops below T_0, the ferroelectric phase will no longer have a stable state at $P = 0$. Instead, the zero-polarization point becomes a local maximum while double minima emerge as two distinct stable phases representing opposite polarizations at $P \neq 0$. The ferroelectric F-P relationship is thus exhibiting as a "double-well" model as illustrated in Figure 1.3(b).

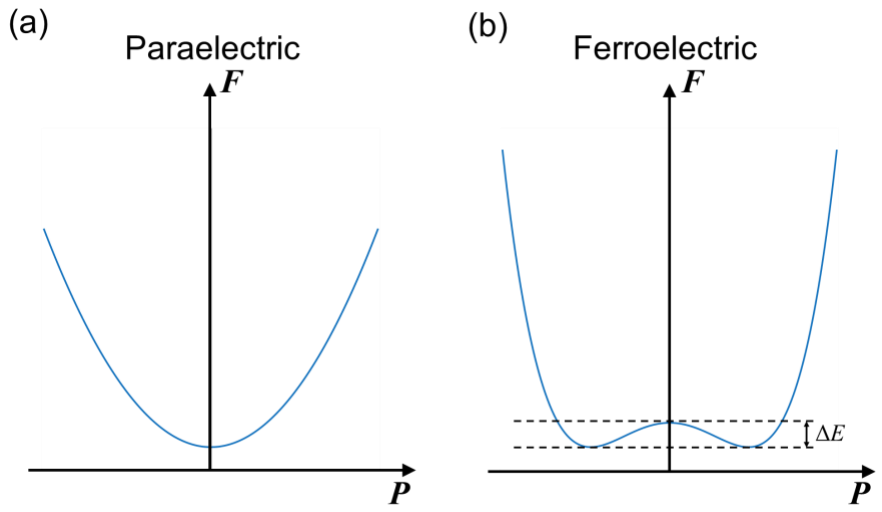


Figure 1.3 Schematic of the free energy F as a function of the polarization P of (a) paraelectric materials with a parabola shape and (b) ferroelectric materials with a double well separated by the energy barrier ΔE.

In the ferroelectric phase under no external field, the two minima correspond to the reversible spontaneous polarizations $\pm P_S$, which can be obtained by solving the derivative of the free energy density to be zero:

$$\frac{\partial F_P}{\partial P} = a_0(T - T_0)P + bP^3 + cP^5 = P(a_0(T - T_0) + bP^2 + cP^4) = 0 \qquad (1.9)$$

since $P = 0$ is a local maximum, the equation can further be simplified to:

$$a_0(T - T_0) + bP^2 + cP^4 = 0 \tag{1.10}$$

solving the equation gives spontaneous polarizations as:

$$P_S = \sqrt{\frac{-b \pm \left(\sqrt{b^2 - 4ba_0(T - T_0)}\right.}{2c}} \tag{1.11}$$

When the ferroelectric crystal is under external electric field ($E \neq 0$), the hysteresis loop (P-E loop) can be calculated from Eq. (1.12):

$$\frac{\partial F_P}{\partial P} = a_0(T - T_0)P + bP^3 + cP^5 - E = 0 \tag{1.12}$$

which can be rearranged to:

$$E = a_0(T - T_0)P + bP^3 + cP^5 = 0 \tag{1.13}$$

Among non-centrosymmetric wurtzite crystals, III-nitrides such as AlN are well-known piezoelectric materials.[27] However, switching the polarity of AlN has long been a challenging task because the barrier ΔE is so high that the electric field required to reverse the polarization is larger than its breakdown field. Although several recent works have demonstrated the ferroelectric switching in AlN by tuning the deposition parameters, the coercive field remains very high (~8 MV/cm) that is relatively close to the breakdown field and requires thicker AlN layer (> 25 nm).[28-30]

Beginning with the extensive research on the piezoelectricity enhancement in AlN by Sc doping, more theoretical studies revealed that the elastic constant reduced, leading to a softer bonding.[31] Meanwhile, the lattice structure gets distorted in a way that the lattice parameters ratio c/a decreased while the u parameter increased.[32] The structural change gets more significant with more Sc incorporation until at a certain point where it gets close to the hexagonal ScN phase. Such structural change also suggests that the doping of Sc can lower the barrier for wurtzite nitrides switching. In 2019, Fichtner *et al.* demonstrated the ferroelectric switching in Sc-doped AlN, opening more opportunities for the piezoelectric nitrides.[21]

In the hexagonal structure, $u = 0.5$ and no spontaneous polarization exists. However, this can be regarded as a middle state during the ScAlN ferroelectric switching from metal-polar to N-polar or vice versa, as illustrated in Figure 1.4(a).[21] It can also be used as a barrier reference point, i.e., the maximum in the double-well barrier model. Wang *et al.* employed the Ginzburg-Landau theory to theoretically model the ScAlN ferroelectric switching.[33] It is confirmed that the doping of Sc can flatten the landscape as shown in Figure 1.4(b) and the calculated barrier will reduce more with higher Sc doping concentrations, as shown in Figure 1.4(c).

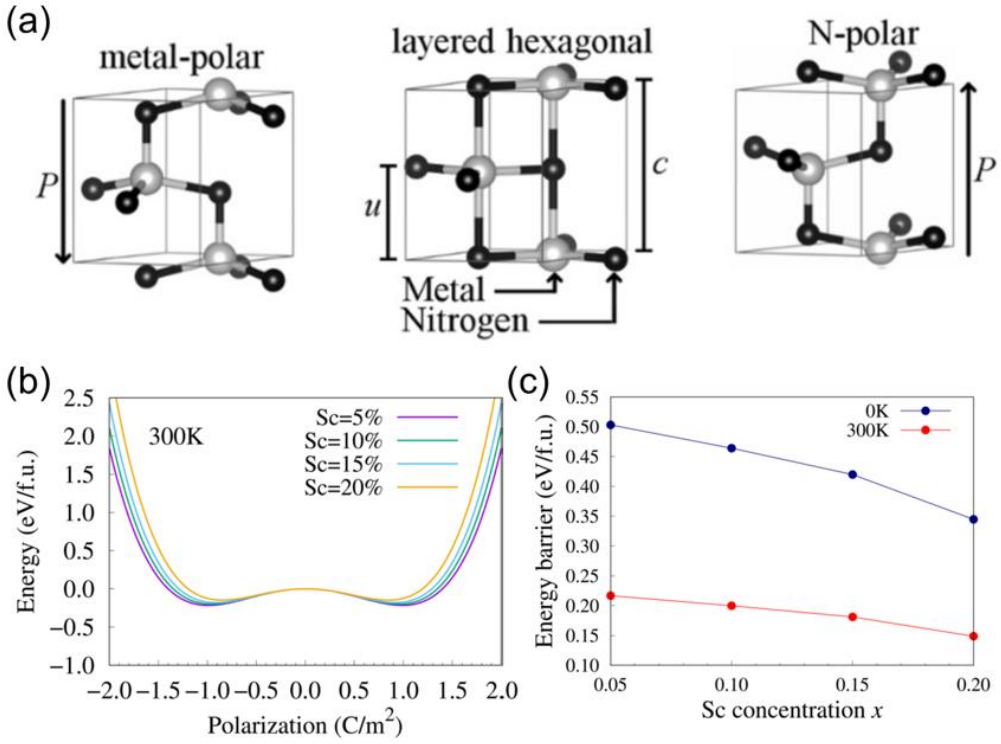


Figure 1.4: (a) Structural illustration of the ScAlN with different polarization states of wurtzite metal-polar, wurtzite nitrogen-polar and non-polar layered hexagonal.[21] (b) Theoretical calculations on energy per formula unit as a function of polarization at 300 K, and (c) switching barrier height at 0 K and 300 K for Sc doping levels from 5% to 20%.[33]

Most of the early work on ScAlN piezoelectric and ferroelectric studies were done in sputtered films, which are cost-effective yet showing more impurities incorporation and polycrystalline features.[34] To improve the crystallinity and phase purity, ScAlN epitaxial growth by molecular beam epitaxy (MBE) and metal-organic chemical vapor deposition (MOCVD) were developed.[3, 22, 35-37] In this thesis, the ScAlN and associated structures were grown by MBE, which has single-crystalline structure and maintains pure wurtzite structure over a wide range of Sc doping level. Representative 2θ-ω X-ray diffraction (XRD) scan for $Sc_xAl_{1-x}N$ film is shown

in Figure 1.5(a) and the full width at half maximum (FWHM) of the (002) planes are 300-400 arcsec. Smooth surface with root mean square (RMS) roughness below 1 nm have been achieved in $Sc_xAl_{1-x}N$ with x up to 38% as shown in Figure 1.5(b).[35] The epitaxial nature of MBE growth also enables a clean and sharp interface between ScAlN and other III-nitrides materials such as GaN and AlN, which is critical to building high performance electronic and photonic devices as we will introduce in the following chapters.

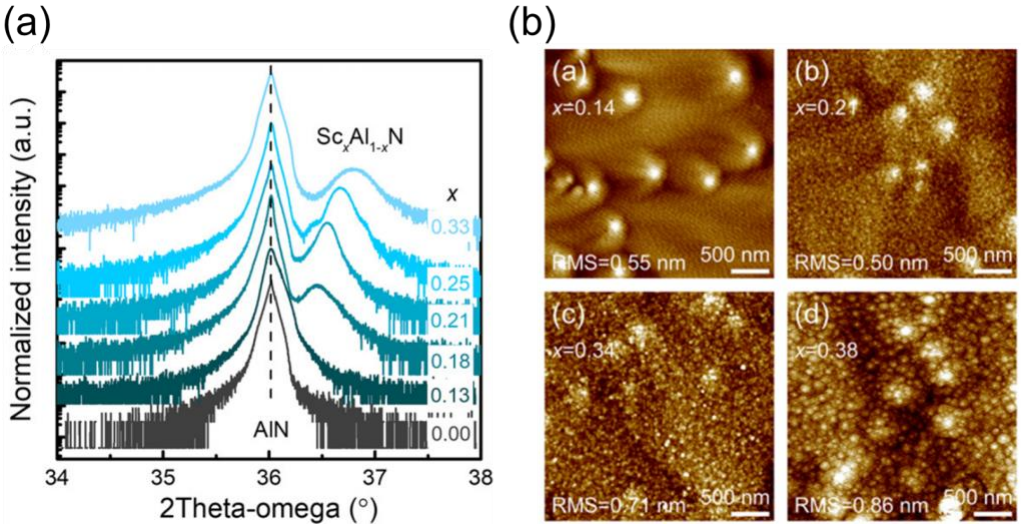


Figure 1.5: MBE-grown (Sc)AlN samples characterizations. (a) XRD 2θ-ω scan of with ScAlN (002) peaks next to the AlN peaks around 36°. (b) Atomic-force microscopy images showing roughness < 1 nm.[35]

Compared with the conventional oxide-based ferroelectric materials, such as hafnium oxide (HfO_2), barium titanate ($BaTiO_3$, BTO) and lead zirconate titanate (PZT), which typically have a lower paraelectric-ferroelectric transition temperature and a complex perovskite structure, ScAlN is stabilized at its wurtzite phase with a Curie temperature exceeding 1000 ˚C.[38, 39] By tailoring the Sc doping level, the coercive field E_c can be adjusted to meet the device design requirements with the strong remnant polarization P_r ~150 μC/cm that could be beneficial for memory devices with better state separation. As a group III-nitride material, it can be seamlessly integrated with the developed (Al)GaN platform in a CMOS-compatible process to boost the optoelectric and power device performance.[1] Table 1.3 below compares ScAlN with other oxide-based materials in terms of ferroelectric properties.

Table 1.3: Ferroelectric characteristics comparison between ScAlN and HfO_2, BTO and PZT. Data from [40-43].

Materials	ScAlN	HfO_2	BTO	PZT
Remnant polaization, P_r ($\mu C/cm^2$)	80-150	10-40	< 30	< 40
Coercive field, E_c (MV/cm)	2-6	0.7-2	< 0.05	< 0.1
Curie temperature, T_C (˚C)	> 1000	~ 500	~ 120	~ 400
CMOS compatibility	Yes	Yes	Yes	No

1.2.2 Enhanced Second-order Nonlinearity in ScAlN

The significant success in optoelectronic applications in III-nitrides has established them as ideal materials for light sources. Combined with their wide bandgap, optical nonlinearity, and piezoelectricity, III-nitrides, especially AlN is considered to be a compelling platform for building integrated photonics, enabling on-chip active functions such as frequency conversion, electro-optic modulation and acousto-optic modulation over a wide range of wavelengths.[44-49]

One of the critical properties to achieve optical signal conversion and modulation in the integrated platform is the second-order optical nonlinearity ($\chi^{(2)}$). It enables several important processes that will not happen in a linear crystal, including second-harmonic generation (SHG), sum-frequency generation (SFG) and difference-frequency generation (DFG) as illustrated in Figure 1.6. For a dielectric material under the optical field E, the induced polarization P can be expanded as a power series:

$$P = \epsilon_0\left[\chi^{(1)}E + \chi^{(2)}E^2 + x^{(3)}E^3 + \cdots\right] \tag{1.14}$$

where ϵ_0 is the permittivity in free space, $\chi^{(1)}$ is the linear susceptibility, $\chi^{(2)}$ and $\chi^{(3)}$ represents second- and third-order nonlinear optical susceptibilities respectively.[50] In a linear optical system, $\chi^{(2)}$ and $\chi^{(3)}$ are zero and the relationship can be simplified to

$$P = \epsilon_0\chi^{(1)}E \tag{1.15}$$

When considering the vector nature, the susceptibility can be expressed as tensors and the second-order term can then be expressed as:

$$\begin{bmatrix} P_x(2\omega) \\ P_y(2\omega) \\ P_z(2\omega) \end{bmatrix} = 2\epsilon_0 \begin{bmatrix} d_{11} & d_{12} & d_{13} & d_{14} & d_{15} & d_{16} \\ d_{21} & d_{22} & d_{23} & d_{24} & d_{25} & d_{26} \\ d_{31} & d_{32} & d_{33} & d_{34} & d_{35} & d_{36} \end{bmatrix} \begin{bmatrix} E_x^2(\omega) \\ E_y^2(\omega) \\ E_z^2(w) \\ 2E_y(w)E_z(w) \\ 2E_x(\omega)E_z(\omega) \\ 2E_x(\omega)E_y(\omega) \end{bmatrix} \tag{1.16}$$

where the d_{ij} components are defined as:

$$d_{ij} = \frac{1}{2}\chi_{ij}^{(2)} \tag{1.17}$$

For the 3 × 6 matrix, the 18 components can be much reduced when considering the symmetry in the crystal. For AlN and ScAlN, which has a wurtzite structure with 6*mm* space group, the tensor can be reduced to:

$$\begin{bmatrix} 0 & 0 & 0 & 0 & d_{31} & 0 \\ 0 & 0 & 0 & d_{31} & 0 & 0 \\ d_{31} & d_{31} & d_{33} & 0 & 0 & 0 \end{bmatrix} \tag{1.18}$$

with all the non-diagonal components to be d_{31} and a diagonal term d_{33} while all other components are zero due to the symmetry.[51]

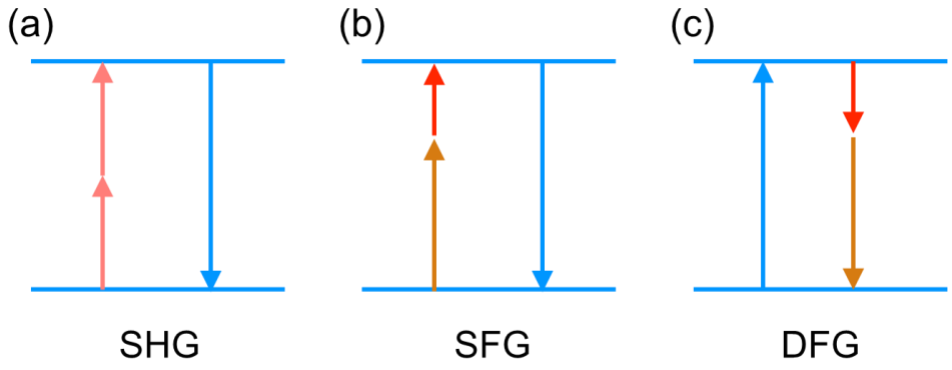


Figure 1.6: Illustration of the second-order optical nonlinear processes of (a) SHG, (b) SFG, and (c) DFG. Two horizontal lines represent the energy levels, and the length of arrow is proportional to the photon energy.

For crystal to manifest non-zero $\chi^{(2)}$, the structure needs to be non-centrosymmetric and as discussed in section 1.1.2, wurtzite has this broken symmetry which is ideal for the second-order nonlinear optical platforms. Several works have built active components on AlN to show its great potential in integrated photonics. Bruch *et al.* achieved second-harmonic generation in AlN microring resonators with conversion efficiency of 17,000 %/W [52] and Xiong *et al.*

demonstrated electro-optic modulation up to 4.5 Gbps [46]. However, compared with the popular $\chi^{(2)}$ materials, such as lithium niobate ($LiNbO_3$, LNO), the second-order optical nonlinear susceptibility is less in AlN.[53] For SHG, the second-harmonic signal intensity with frequency 2ω, $I_{2\omega}$ is proportional to the square of the intensity of the input signal with fundamental frequency ω, I_ω and the effective second-order nonlinear susceptibility ($\chi_{eff}^{(2)}$), i.e. $I_{2\omega} \propto \left[\chi_{eff}^{(2)}\right]^2 I_\omega^2$. Therefore, a higher $\chi_{eff}^{(2)}$ is needed in AlN to further improve the conversion efficiency.

As discussed in previous sections, doping Sc to AlN can drastically enhance the piezoelectricity and induce the ferroelectricity. The main reason for such property is owing to the bonding and structural change in the crystal lattice. According to the bond-charge model [54], which can be used to calculate the nonlinear susceptibility and has been applied to explain the $\chi^{(2)}$ enhancement in boron-doped AlN ($B_xAl_{1-x}N$) [55], this lattice distortion by Sc doping could also induce larger $\chi^{(2)}$ in ScAlN compared with AlN. This is due to the Sc doping on the Al sites can induce local bonding angle variations and increase the susceptibility component projection on the basal plane. This assumption is validated in the experimental measurement by Yoshioka *et al.*, which shows continuous enhancement in $\chi^{(2)}$ with higher Sc doping levels.[56] A detailed investigation on the MBE epitaxial ScAlN $\chi^{(2)}$ show the same trend and will be discussed in the following chapters.

The incorporation of Sc will slightly decrease the bandgap of AlN but remains to be ultrawide that provides a transparency window down to the UV wavelengths.[35] In conjugation with the strong piezoelectricity and the ferroelectricity, ScAlN is emerging as a multi-functional for quantum applications.

1.3 Dissertation Overview

This dissertation aims to present a detailed investigation on epitaxial ScAlN as an emerging ultrawide-bandgap platform for integrated photonics and high-performance electronics. At a relatively early stage of studying ferroelectric nitride, there are several unknowns and challenges associated with the materials and device applications. The following chapters focus on unveiling some of the mysteries and tackling some of the challenges related to ScAlN, from fundamental materials properties to device demonstrations.

Chapter 2 identifies the critical role of the native oxynitride layer on ScAlN in terms of leakage current and switching voltage. By developing a PMMA-based surface protection strategy in the fabrication process, reduced coercive field, suppressed leakage current, and improved breakdown-to-switching voltage ratio have been achieved. The results show the importance of interfacial engineering for nitride ferroelectric devices and enable improved in-memory computing performance.

Chapter 3 investigates the impact of scandium incorporation on the second-order optical nonlinearity of epitaxial ScAlN. Using the second-harmonic generation polarimetry and transfer-matrix modeling, nonlinear coefficients of d_{31} and d_{33} have been quantitatively extracted, establishing a substantial enhancement of nonlinear optical response to provide experimental insights on structure-property relations in ScAlN.

Chapter 4 extends the study of nonlinear optical properties from Sc-doped AlN to Sc-doped GaN and demonstrated that Sc incorporation can enhance the second-order optical nonlinearity to an even higher value compared to ScAlN. The optical bandgap is measured and observed to be increased with Sc doping level. These results provide information to further explore the potential optical and photonic applications of Sc-doped III-nitrides.

Chapter 5 focuses on reducing the optical loss, which is a common limitation in ScAlN-based photonic devices, by introducing a hybrid ScAlN/Si_3N_4 integrated platform. Combined high quality epitaxial film with careful design, this chapter demonstrates low-loss photonic devices that leverage ScAlN for its functionality including nonlinear conversion and piezoelectric coupling while guiding light by silicon nitride with ultralow loss. This approach provides another route toward integrated quantum photonics.

Starting from chapter 6, the dissertation focuses more on the electronics applications of ScAlN. Chapter 6 investigates polarization-engineered ScAlN/GaN heterostructures for low sheet resistance in GaN-based high-electron-mobility transistors (HEMTs). By exploiting the strong polarization induced by ScAlN and the large conduction band offset in ScAlN/GaN heterostructures, a record-low sheet resistance has been achieved in a single-channel structure. This structure enables GaN HEMTs with better performance for RF applications.

Chapter 7 demonstrates utilizing the heterostructure proposed in chapter 6 to realize high-current ScAlN-barrier GaN HEMTs. This chapter evaluates the device performance under high

temperature and shows a robust operation, highlighting the advantages of ScAlN barrier for high power and high temperature electronics.

Chapter 8 integrates ferroelectric ScAlN into GaN HEMT to enable high-tempearture nonvolatile memory functionality. The device physics and memory characteristics are thoroughly examined with stable ferroelectric switching and retention demonstrated under elevated temperatures.

Chapter 9 presents a novel strategy to achieve enhancement-mode operation of GaN HEMTs by coupling ferroelectric ScAlN with a charge-trapping layer of ScN in the gate stack. This provides a new pathway to achieve normally-off operation in GaN power devices while maintaining good stability.

Chapter 10 explores the integration of ferroelectric ScAlN with Al-rich AlGaN-channel HEMTs, extending the ferroelectric engineering to the all-Al(Ga)N structure with higher bandgap channels, which supports better power handling capabilities.

Finally, chapter 11 summarizes the thesis and outlines prospective research directions based on this thesis, including novel rare-earth elements doping in III-nitrides, quantum engineering in ScAlN heterostructures for extreme nonlinearities, and further improvements in III-nitrides-based electronic device performance.

Chapter 2 Native Oxynitride Layer-Assisted Leakage Current Suppression and Coercive Field Reduction in Nitride Ferroelectrics

2.1 Introduction

The incorporation of rare-earth elements, such as scandium (Sc) and yttrium (Y), into the wurtzite III-nitride lattice has given rise to a new class of non-oxide ferroelectric materials.[21, 57-64] Among these compounds, scandium aluminum nitride (ScAlN) has attracted substantial attention due to its large remanent polarization, exceptional thermal stability, and tunable coercive field.[65-69] Epitaxial ScAlN exhibits negligible wake-up effects and imprints, showing significant potential for high-performance memories and logic applications.[59, 67, 70] Furthermore, their wide processing temperature windows and compatibility with silicon-based platforms and III-nitride technology enables seamless integration with existing semiconductor processes.[57, 71] As a result, ScAlN offers significant promises for enhancing the functionality and versatility of ferroelectric systems, which are critical for advancing memristor technologies in hybrid, multifunctional computing architectures.[72]

As research on nitride ferroelectrics progresses toward aggressive device scaling, surface and interfacial effects become increasingly critical.[73-77] This arises from the significantly enhanced surface-to-volume ratio in smaller devices, where the surface region constitutes a substantial portion of the device. Consequently, the electrical performance, reliability, and scalability of ferroelectric devices become highly sensitive to surface chemistry and structural integrity.[78, 79] Most recently, Wang *et. al.* demonstrated improved reliability in ferroelectric ScAlN non-volatile memory by inserting an AlO_x layer at the top surface, offering a promising surface-engineering strategy to enhance the performance of ScAlN-based devices.[80] Due to the high oxygen affinity of Sc and Al, a thin amorphous oxynitride layer, which is approximately 4 nm thick, often spontaneously forms on the ScAlN surface upon air exposure.[81] This native

The content of this chapter has been published on *ACS Applied Energy Materials*. The work is supported by the Army Research Office under Grant No. W911NF2420210, and by the College of Engineering at the University of Michigan.

oxynitride layer serves as a natural insulating barrier, improving the ON/OFF ratio, rectification characteristics, switching voltage, leakage current suppression, and cycling endurance of ScAlN memristors.[22, 74, 82-84] However, this amphoteric amorphous oxynitride layer is highly vulnerable to damage in alkaline environments, such as those encountered during standard photolithography with tetramethylammonium hydroxide (TMAH)-based developers, a challenge that has long been overlooked. Such damage can partially etch or degrade the oxynitride layer, potentially obscuring its beneficial impact on the performance of nitride ferroelectric memristors.[85]

In this chapter, we investigate the impact of the native oxynitride layer on ScAlN ferroelectric memristors. By implementing a polymethyl methacrylate (PMMA)-based surface protection strategy during device fabrication, the native oxynitride layer was preserved throughout the processing, as confirmed by comprehensive material characterizations. The native oxynitride layer-protected device exhibits a 16% reduction in negative switching voltage and 68% decrease in leakage current compared to the surface-damaged device. In addition, the surface-protected device represents a state-of-the-art breakdown voltage to switching voltage (V_{BD}/V_{SW}) ratio of 1.92 for MBE-grown ScAlN memristors. Furthermore, the low leakage current density of 0.29 A cm^{-2} at E_c represents the lowest value reported for MBE-grown ScAlN ferroelectric memristors to our knowledge. These advancements offer a potential pathway to overcome some of the key obstacles limiting the widespread adoption of wurtzite-based ferroelectric memory technologies.

2.2 ScAlN Growth and Device Characterization Technique

The ScAlN/n-GaN heterostructure was epitaxially grown by plasma-assisted molecular beam epitaxy (MBE) using a Veeco GENxplor system. Elemental sources, including scandium (99.999%), aluminum (99.99995%) and gallium (99.99999%), were delivered through independent Knudsen effusion cells. A 120-nm-thick $Sc_{0.21}Al_{0.79}N$ layer was epitaxially grown on a Si-doped n-GaN template. Upon air exposure, a native oxynitride layer spontaneously formed. The grown wafer was then cleaved into two pieces to investigate the impact of developer on the native oxynitride layer: one piece was protected with PMMA on the sample surface, and the other was not.

After a total of 80 s contact with the developer, both samples were cleaned following a standard procedure. X-ray photoelectron spectroscopy (XPS) was performed using a Kratos Axis

Supra$^+$ correlative spectroscopy and imaging system with monochromatic Al K_α and Ag L_α sources. Energy dispersive X-ray spectroscopy (EDS) was used to calibrate the Sc content in ScAlN in a Hitachi SU8000 scanning electron microscope (SEM). Surface morphology was characterized using a Bruker ICON AFM system. X-ray diffraction (XRD) 2θ scans were collected with the Rigaku SmartLab X-ray diffractometer using a Cu K_α source (wavelength of 1.5406 Å). Scanning transmission electron microscopy (STEM) specimens were prepared using a Thermo Fisher Scientific Helios G4 UXe focused ion beam (FIB) system. High-angle annular dark-field (HAADF) STEM images were acquired on a JEOL 3100R05 aberration-corrected STEM operated at 300 kV, with a collection angle range of 59–200 mrad. AC electrical measurements were conducted using a Radiant Precision Premier II ferroelectric tester, with the signal applied through the top electrode. DC measurements were performed using a Keysight B1500 semiconductor parameter analyzer.

The AZ 726 Metal-ion-free (MIF) developer, a TMAH-based chemical with approximately 2.38% TMAH in water and surfactants added for uniform substrate wetting, is used for spray and puddle developer systems. As shown in Figure 2.1(a), during the photoresist development process in device fabrication, the TMAH reacts with the amphoteric, amorphous native oxynitride layer on ScAlN through a hydroxide-mediated dissolution mechanism involving surface oxynitrides and hydroxide ions (OH^-),[85] potentially removing part of the oxynitride layer and causing ferroelectric performance degradation. The (0002) plane X-ray diffraction (XRD) 2θ scan of the ScAlN/GaN heterostructure (Figure 2.1(b)) reveals a distinct wurtzite phase ScAlN peak near 36°, indicating the underlying ScAlN thin film remains undamaged during development.

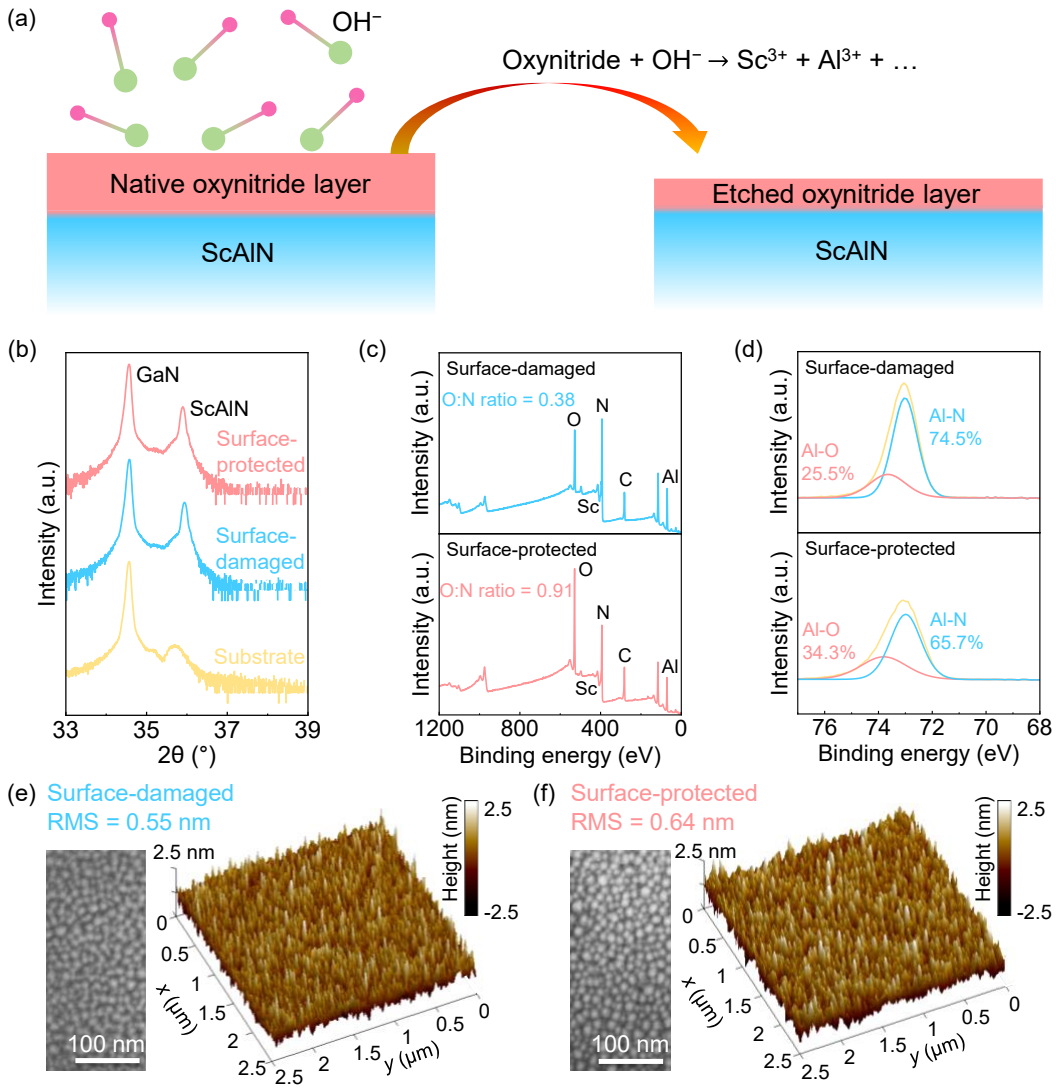


Figure 2.1: (a) Schematic of the native oxynitride layer etching process upon contact with TMAH developer. (b) XRD 2θ scans of surface-protected and surface-damaged samples, along with the GaN substrate. (c) XPS survey spectrum of the samples. (d) High-resolution XPS spectra of the Al 2p core level. (e, f) SEM, AFM images of the surface-damaged (e) and surface-protected samples (f).

Surface-sensitive characterizations further highlight developer-induced surface modifications: X-ray photoelectron spectroscopy (XPS), with a ~10 nm probing depth,[81] indicates a decrease in the oxygen-to-nitrogen (O:N) ratio from 0.91 to 0.38 in surface-damaged samples, suggesting partial oxynitride removal (Figure 2.1(c)). High-resolution XPS spectra (Figure 2.1(d)) reveal a significant decrease in the Al-O bond signal at 73.7 eV upon developer exposure, confirming the important role of the PMMA layer in preserving the native oxynitride

layer. Atomic force microscopy (AFM) and scanning electron microscopy (SEM) (Figure 2.1(e-f)) reveal surface morphology degradation in surface-damaged samples, with AFM indicating finer features in surface-protected samples, as evidenced by a higher root mean square roughness (RMS), and SEM showing pronounced grain boundaries in surface-damaged surfaces, both indicating developer-induced etching of nanoscale features.

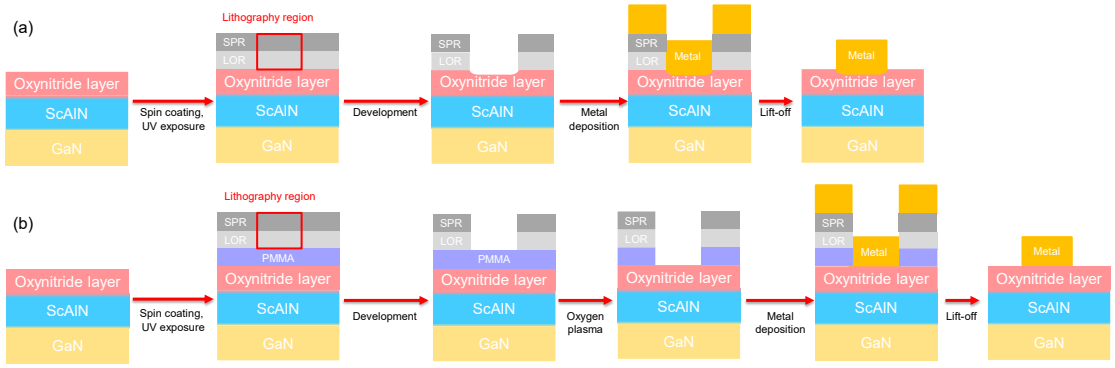


Figure 2.2: Schematic of the memristor fabrication processes. (a) Without PMMA protection. (b) With PMMA protection.

To investigate the correlation between native oxynitride layer damage and ferroelectric device performance, two distinct fabrication processes were designed. In the standard process illustrated in Figure 2.2(a), after material growth and air exposure, samples are cleaned with acetone and methanol under ultrasonication. A bilayer photoresist stack consisting of LOR (lift-off resist) and SPR (positive photoresist) is then spin-coated, with the LOR layer designed to create an undercut for cleaner lift-off. The areas for metal electrodes are patterned using UV exposure through a contact mask and developed with AZ 726 developer, which can partially etch the native oxynitride layer on the exposed ScAlN surfaces. Subsequently, a Ti/Al/Pt metal stack is deposited using electron-beam evaporation, and the electrode is formed through the lift-off process. To preserve the oxynitride layer, an alternative fabrication process (Figure 2.2(b)) includes an additional PMMA layer spin-coated beneath the LOR/SPR stack. During the development step, while the exposed LOR and SPR are removed, the PMMA layer remains intact due to its resistance to the TMAH-based developer, thereby protecting the ScAlN surface from alkaline exposure. The PMMA layer is later removed using oxygen plasma before the electrode deposition. The time interval between PMMA removal and loading the sample into the metal deposition equipment, followed by evacuation to vacuum, is kept within 1 minute.

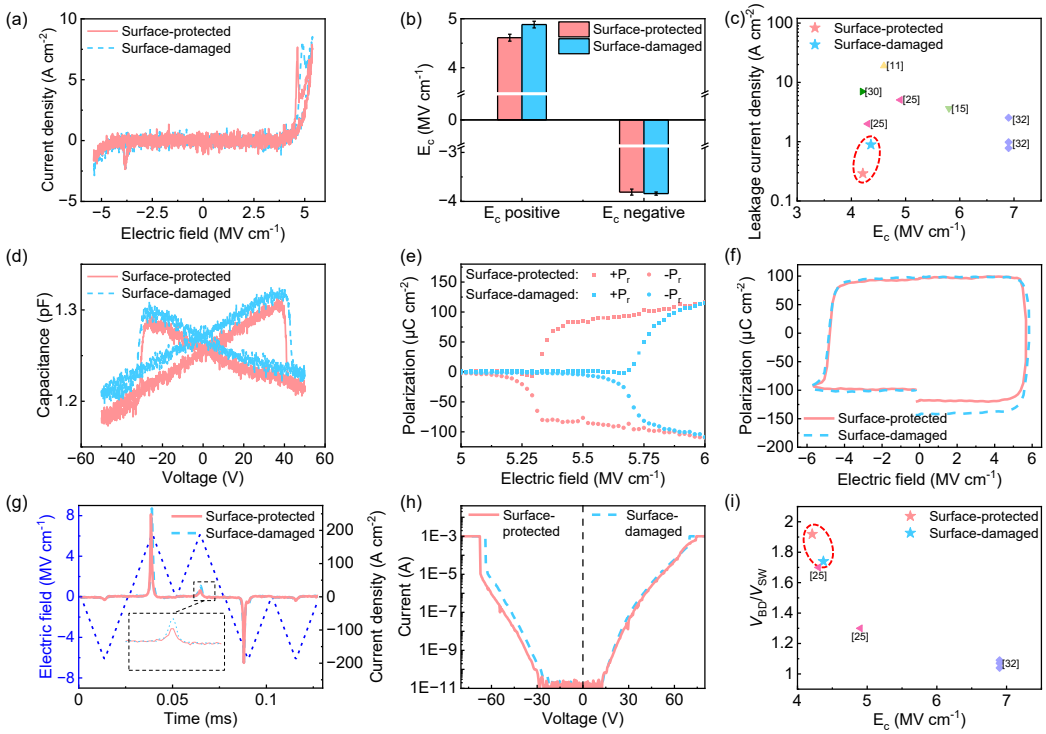


Figure 2.3: Ferroelectric properties of ScAlN capacitors. (a) *J-E* loops measured by a triangular waveform with 10 ms period at ±65 V maximum bias. (b) Coercive field of surface-protected and surface-damaged devices extracted from *J-E* loops. (c) Comparison of leakage current density at the coercive field extracted from AC *J-E* loops for MBE-grown ScAlN. (d) Typical butterfly *C-V* curves measured at 2 MHz. (e) Electric-field-dependent PUND measurements. (f) Representative *P-E* loops measured at 12.5 kHz. (g) Transient PUND results measured with pulse width of 0.025 ms. (h) Representative *I-V* curves recorded after negative or positive poling. (i) Comparison of V_{BD}/V_{SW} and E_c performance with other MBE-grown ScAlN memristors.

To evaluate the ferroelectric characteristics of the memristors, a suite of electrical measurements was conducted, including current–electric field (*J-E*), capacitance–voltage (*C-V*), polarization–electric field (*P-E*) loops and positive-up-negative-down (PUND) measurements. Figure 2.3(a) presents representative AC *J-E* loops, revealing pronounced displacement current peaks that confirm robust ferroelectric switching in both samples. The extracted coercive field (E_c) and corresponding leakage current density from the non-switching branch (Figure 2.3(b-c)) show a significant reduction of leakage in the surface-protected device, achieving a leakage current density of 0.29 A cm^{-2} at E_c. Although the lowest leakage current density of 0.07 A cm^{-2} at E_c was reported in sputtering-grown 250nm ScAlN film,[86] similar or even lower leakage current could be achieved in MBE-grown ScAlN by increasing the thickness of ferroelectric layer or further optimization on the native oxynitride layer quality. The characteristic butterfly-shaped *C-V*

hysteresis loops with dual peaks, as shown in Figure 2.3(d), further confirm ferroelectricity in both devices. The coercive field of the surface-protected device, determined from the peak positions, is lower in both polarities. The upward shift of the *C-V* curve observed in the surface-damaged memristor could be attributed to oxynitride degradation. In a typical ferroelectric stack, the total measured capacitance can be modeled as a series combination of the ferroelectric layer (FE), the interfacial layer (IL), and any parasitic components: $\frac{1}{C} = \frac{1}{C_{IL}} + \frac{1}{C_{FE}} + \frac{1}{C_{parasitic}}$.[82] The capacitance is expressed as $C = \varepsilon\frac{A}{d}$, where C is the capacitance, ε is the dielectric constant, A is the capacitor surface area, and d is the thickness of the insulator between electrodes. Degradation at the interface, such as oxynitride thinning, reduces the interfacial layer thickness, thereby increasing the overall capacitance of the stack.[82] Although the interfacial layer is significantly thinner than the ferroelectric layer, it still contributes to the overall capacitance due to its lower permittivity.[87, 88]

Additionally, electric-field-dependent polarization measurements (Figure 2.3(e)), conducted with a 12.5 kHz triangular waveform using PUND tests, reveal that polarization saturation begins at approximately 5.4 MV cm^{-1} for the surface-protected device and 5.8 MV cm^{-1} for the surface-damaged device, with the latter exhibiting a steeper increase in polarization within the saturation region due to higher leakage currents under high electric fields. *P-E* loops extracted from the electric-field-dependent PUND measurement (Figure 2.3(f)) reveal nearly identical polarization values for both devices, reflecting comparable film quality and intrinsic remanent polarization, while the broader positive-bias loop in the surface-damaged device indicates elevated leakage current induced by partial oxynitride degradation.

Transient PUND measurements at 6.25 MV cm^{-1} with a 0.025 ms pulse width (Figure 2.3(g)) further confirm higher leakage in the surface-damaged device. A preliminary negative pulse is applied to ensure full polarization switching upon the subsequent positive pulse. For P and N pulses, the current response is the sum of switching current and non-switching current, while U and D pulses primarily reflect non-switching (leakage) current. The inset of Figure 2.3(g) clearly shows higher leakage current for the surface-damaged device. To further evaluate the ferroelectric performance, DC measurements were conducted to investigate the breakdown characteristics of the devices. To eliminate contributions from switching current, a negative poling waveform from 0 V to –50 V or a positive poling from 0 V to 50 V was applied before the test. Figure 2.3(h)

presents the *I-V* characteristics under bias sweeps from 0 V to –80 V and 0 V to 80 V. The surface-protected device shows higher breakdown voltage in both directions than the surface-damaged device. Moreover, the surface-protected device, owing to its reduced coercive field, achieves a higher V_{BD}/V_{SW} figure of merit, indicating a broader operational window. A large V_{BD}/V_{SW} ratio of 1.92 is achieved, compared with the V_{BD}/V_{SW} ratio of 1.74 for surface-damaged devices, with $V_{BD} = (V_{BD}^{+} + |V_{BD}^{-}|) / 2$, $V_{SW} = (V_{SW}^{+} + |V_{SW}^{-}|) / 2$, as summarized in Figure 2.3(i). A state-of-the-art V_{BD}/V_{SW} ratio of 2.6 has been reported in devices fabricated via sputtering and scaling down to 0.05 μm diameter.[89] Lateral downscaling in our proposed device is expected to further enhance the V_{BD}/V_{SW} ratio.

To understand how the preserved native oxynitride layer reduces switching voltage and leakage current, we conceptually treat it as an interfacial layer (IL). Using a first-order, single-domain ferroelectric model, the change in switching voltage due to variations in the interfacial layer thickness is given by: $\Delta V_{SW} = \frac{\varepsilon_{FE}}{\varepsilon_{IL}} \Delta t_{IL} (E_{c,intrinsic} - \frac{P_{FE}}{\varepsilon_{FE}})$, where $E_{c,intrinsic}$ is the intrinsic coercive field, and P_{FE} is the polarization of the ferroelectric layer, which can be modeled as a bound sheet charge density at the interfaces of the ferroelectric layer.[80] The term $-\frac{P_{FE}}{\varepsilon_{FE}}$ represents the depolarization field in the ferroelectric layer without polarization charge screening, with this field always opposing the direction of P_{FE}. When $E_{c,intrinsic} - \frac{P_{FE}}{\varepsilon_{FE}} < 0$, the introduction of an interfacial layer leads to a reduction in the switching voltage. This condition is true for ScAlN due to its high remanent polarization and low dielectric constant.[66] By protecting the native oxynitride layer with an additional PMMA layer, a greater t_{IL} remained, thus resulting in a lower switching voltage than the surface-damaged device.

2.3 Device Applications with Oxynitride Layer Incorporation

The surface-protected ScAlN capacitor offers a promising platform for in-memory computing, which relies on a stable native oxynitride layer to enable distinct multilevel conductance states (Figure 2.4(a)). Figure 2.4(b) shows a cross-sectional scanning transmission electron microscopy (STEM) image and energy dispersive X-ray spectroscopy (EDS) mappings for Sc, Al, Ga, and O of the surface-protected device, indicating the presence of a uniform oxynitride layer at the ScAlN surface with minimal interaction with the developer during fabrication. Figure 2.4(c) presents quasi-static *I-V* characteristics from a bipolar ±50 V voltage

sweeps in 100 mV steps, revealing a pronounced conductance change before and after the polarization switching. In the negative-bias region, selecting –27 V as the read voltage significantly suppresses the leakage current by 82%. The surface-protected device exhibits an ON/OFF ratio exceeding 300, which is substantially higher than the value of 60 observed in the surface-damaged counterpart. Additionally, a noticeable reduction in switching voltage is observed, consistent with the results from AC measurements. The rectification ratio, extracted at the point of the maximum ON/OFF ratio, increases from 113 in the surface-damaged device to 1165 in the surface-protected device. This enhancement facilitates selector-free memory array integration, enabling higher density and reduced power consumption.[89, 90] As shown in Figure 2.4(d), the OFF-state leakage characteristics of both devices are well described by the Poole-Frenkel emission model, indicating that trap-assisted electron transport is the dominant leakage mechanism.[83, 91] The slightly steeper slope of the fitting curve for the surface-protected device, indicating a lower relative permittivity than the surface-damaged counterpart, which is consistent with the *C-V* measurements.[91] According to the model, a smaller intercept corresponds to a higher activation energy, which reflects suppressed trap-mediated conduction and improved breakdown strength in the epitaxially grown films.[92] The large memory window enables the device to emulate biological synapses, as depicted in Figure 2.4(e). Figure 2.4(f) illustrates conductance-based weight modulation using two voltage waveform schemes: identical potentiation with a 35 V write pulse and depression with a –28 V erase pulse; and linear potentiation ramping from 30 V to 35 V and depression from –20.5 V to –45 V. The read pulse after each write/erase pulse is 25 V. The pulse width for write, erase and read pulses are 60 ms, 90 ms, and 0.18 s, respectively. Device-level simulations were conducted to assess the applicability of the nitride-based ferroelectric memristor in neuromorphic computing. These simulations utilized multilevel conductance states and were based on the CIFAR-10 dataset with a Visual Geometry Group (VGG-8) architecture, as shown in Figure 2.4(g-i)**.** The conductance states were directly mapped as synaptic weights in a convolutional neural network. Both linear and nonlinear update schemes exhibit rapid accuracy convergence within the first 50 training epochs, followed by gradual saturation. Notably, the device with linear potentiation and depression achieves a classification accuracy of 92.5%, closely approaching the idealized upper bound of 94.5%. These

findings highlight the potential of ScAlN-based memristors for high-accuracy, hardware-efficient neural network implementations.

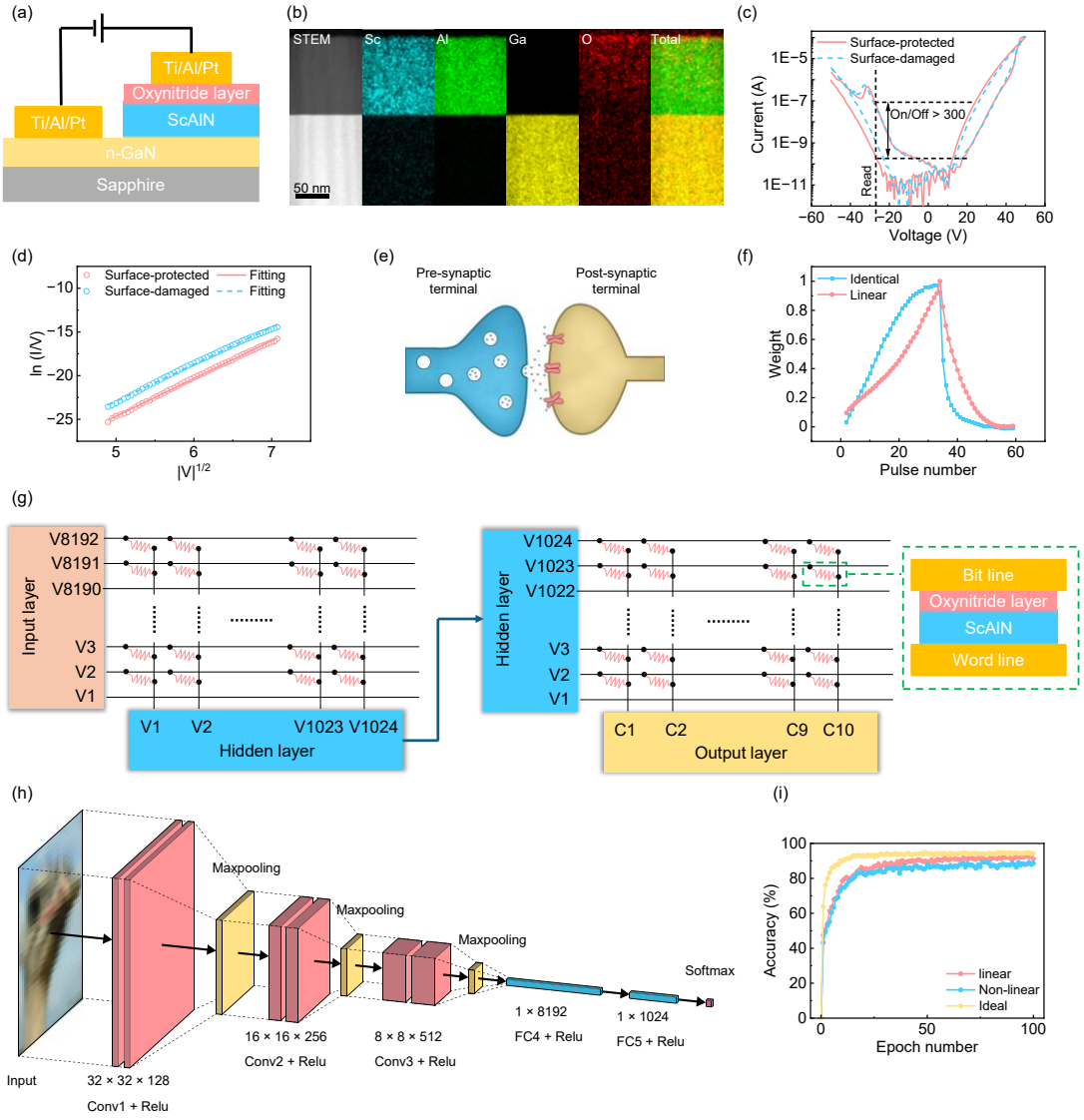


Figure 2.4: (a) Schematic illustration of the ferroelectric capacitor. (b) STEM and corresponding EDS element mappings of the ScAlN/GaN heterostructure. (c) Quasi-static *I-V* measurements of surface-protected and surface-damaged devices. (d) Poole-Frenkel fitting of the negative-bias OFF state data from (c). (e) Schematic of a biological synapse. (f) Potentiation and depression behavior of the conductance in response to different electrical pulses, analogous to synaptic plasticity. (g) Hardware neural network configuration using ScAlN memristors for fully connected layers. (h) Schematic of the VGG-8 network architecture used for CIFAR classification and synaptic weight emulation. (i) Comparison of test accuracy on the CIFAR dataset using ScAlN capacitors with linear and nonlinear properties, alongside an ideal device.

2.4 Conclusion

In summary, by introducing a polymethyl methacrylate (PMMA)-based surface protection approach to preserve the native oxynitride layer during fabrication, its beneficial effect on nitride ferroelectric performance is conclusively demonstrated. Comprehensive ferroelectric measurements confirm that the protected native oxynitride layer contributes to improved device performance in ScAlN/GaN capacitors, making them more suited for non-volatile ferroelectric memory applications. Specifically, compared to surface-damaged counterparts, surface-protected devices exhibit a 16% reduction in coercive field, a 68% decrease in leakage current, and a large VBD/VSW ratio of 1.92, which improves reliability for memory applications. These results provide a promising pathway for integrating nitride-based ferroelectric devices into next-generation data storage and advanced computing systems.

Chapter 3 Impact of Scandium Doping on the Second-order Optical Nonlinearity in Epitaxial Aluminum Nitride

The content of this chapter has been submitted to *Applied Physics Letters*. The work is supported by the Army Research Office under Grant No. W911NF2420210, and by the College of Engineering at the University of Michigan.

3.1 Introduction

Recent research has led to several impressive milestones in integrated photonics using various material platforms.[93-97] The identification of an ideal platform, characterized by CMOS compatibility, low propagation loss, a broad transparency window, and strong optical nonlinearities, remains a key challenge in integrated photonics. Among these desirable properties, strong nonlinear interactions are crucial for numerous photonic applications, including optical switching,[98, 99] frequency conversion,[100, 101] and the generation of quantum states of light.[102] In this context, non-centrosymmetric materials, which facilitate second-order non-linear processes, offer distinct advantages. They possess stronger interactions compared to third-order processes, while maintaining the ability to produce third-order effects through cascaded second-order interactions.[103]

Lithium niobate ($LiNbO_3$) is currently one of the leading platforms for second-order nonlinear integrated photonics.[104] It has a high second-order nonlinearity ($d_{33} \simeq 20$ pm/V and $d_{31} \simeq 3$ pm/V at $\lambda = 1313$ nm)[105] and a wide-transparency window (400 nm to 5 μm).[104] Its use in integrated photonics is nevertheless hindered by fabrication complexity and a lack of direct CMOS compatibility, which is crucial for scalable and cost-effective device manufacturing.[106] Aluminum nitride (AlN) provides a compelling alternative, being CMOS-compatible and possessing a wide transparency window (200 nm to 13.6 μm).[45, 107] However, its relatively

The content of this chapter has been submitted to *Applied Physics Letters*. The work is supported by the Army Research Office under Grant No. W911NF2420210, and by the College of Engineering at the University of Michigan.

low second-order nonlinearity (d_{33} = 3.8−11 pm/V and d_{31} = 0.04−0.3 pm/V at wavelengths around 1 μm) has limited its potential.[51] Meanwhile, gallium-containing nitride alloys such as gallium nitride (GaN) and indium gallium nitride have found widespread use for optoelectronics, but their narrower bandgap limits their usable spectral range, and they tend to have higher propagation losses.[108] Moreover, $LiNbO_3$ is prone to optical damage due to its strong photorefractive effect,[109] whereas ultrawide bandgap III-nitrides are extremely robust and stable under high power operation.

To increase second-order nonlinearities in nitride-based materials, elemental doping with boron (B) or scandium (Sc) has emerged as a promising strategy. Previous studies on sputtered AlN thin films have demonstrated significant enhancements using such substitutions.[55, 56, 110] Specifically, boron substitution in $B_{0.11}Al_{0.89}N$ resulted in a greater than 10-fold increase in d_{31} and a negligible change in d_{33},[55] while scandium substitution in $Sc_{0.36}Al_{0.64}N$ yielded a 64-fold increase in d_{31} and a 12-fold increase in d_{33}.[56] Despite these promising horizons, second-order optical nonlinearities of ScAlN remain under explored. In this chapter, we present the first study of the second-order nonlinear properties of monocrystalline $Sc_xAl_{1-x}N$ thin films, grown by molecular beam epitaxy (MBE), over a range of scandium concentrations ($0 \leqslant x \leqslant 0.30$) at an excitation wavelength of λ =1266 nm. Our results reveal a 17-fold enhancement of the d_{31} nonlinear coefficient compared to AlN. In stark contrast to prior reports, d_{33} exhibits a modest decrease for this range of scandium concentrations. This trend reveals a non-monotonic behavior with the potential for enhancement at higher scandium concentrations. Our observations are based on comprehensive studies of the epitaxial growth, including epitaxial growth of ScAlN on different substrates (sapphire, Si, and Al metal deposited in-situ by MBE on Si), and thorough characterization by both transmission and reflective measurements. In this work, we detail the growth and characterization of ScAlN films, present the measured nonlinear optical coefficients, and discuss our findings in the context of previous studies.

3.2 Epitaxial Growth of ScAlN

Epitaxial $Sc_xAl_{1-x}N$ films were grown using a Veeco GENxplor plasma-assisted molecular beam epitaxy (PA-MBE) system. High-purity scandium (Sc, 5N purity) and aluminum (Al, 6N5 purity) sources were evaporated from effusion cells, while nitrogen was supplied via a radio frequency (RF) plasma-assisted nitrogen source. The composition of $Sc_xAl_{1-x}N$ was precisely

controlled by adjusting the beam equivalent pressure (BEP) ratio of Sc to Al. To investigate the effect of Sc composition on the second-order nonlinearity, a series of 275 nm thick $Sc_xAl_{1-x}N$ films, with Sc compositions ranging from 0% (AlN) to 30% ($Sc_{0.30}Al_{0.70}N$), were grown on double-side polished *c*-plane sapphire wafers with a 150 nm AlN buffer layer, as illustrated by Figure 3.1(a). The buffer layer is used to reduce the lattice mismatch between the sapphire substrate and ScAlN film for better material quality. The thicknesses were chosen to ensure a dominant signal from the $Sc_xAl_{1-x}N$ layer relative to the AlN buffer and were validated with cross-sectional scanning electron microscope. To maintain the non-centrosymmetric wurtzite phase of ScAlN, a nitrogen-rich environment was used during growth, minimizing the formation of undesired phases and Sc-Al intermetallic compounds.[111] The Sc compositions were determined using energy-dispersive X-ray spectroscopy (EDS) on samples grown on GaN/sapphire, eliminating interference from Al signals from the substrate or buffer layer. The surface roughness of the $Sc_{0.20}Al_{0.80}N$ film was characterized by atomic force microscopy (AFM), revealing a root-mean-square roughness of 1.5 nm over a 1 μm × 1 μm area. The characterization result is shown in Figure 3.1(b). X-ray diffraction (XRD) spectra of AlN and $Sc_{0.20}Al_{0.80}N$, plotted in Figure 3.1(c), exhibited sharp peaks, confirming the high crystallinity of the films. Cross-sectional transmission electron microscopy (TEM) analysis of the ScAlN film, as shown in Figure 3.1(d) further corroborated the well-oriented crystal structure.

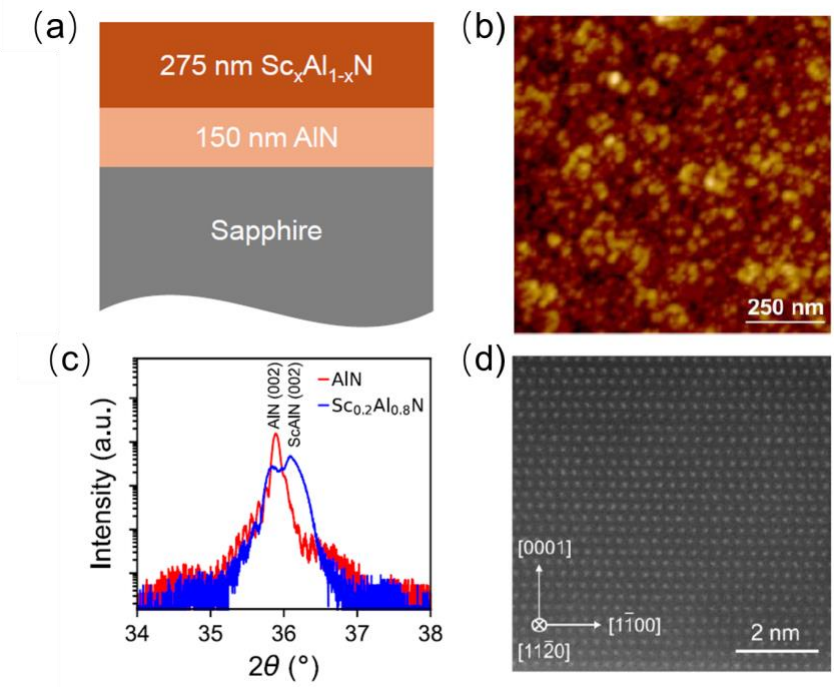


Figure 3.1: (a) Illustration of the structure of the measured samples. ScAlN with 10%, 20% and 30% Sc concentration grown on sapphire wafers with a thin AlN buffer layer. (b) Atomic force microscopy image scanning the surface of the $Sc_{0.20}Al_{0.80}N$ with surface roughness 1.5 nm. (c) X-ray diffraction pattern of AlN and $Sc_{0.20}Al_{0.80}N$ thin film with AlN buffer layer. (d) The cross-sectional transmission electron microscopy characterization on the single crystalline ScAlN film.

3.3 Second-order Optical Nonlinear Characterization of ScAlN

The second-order nonlinearities of our ScAlN samples were characterized using second harmonic (SH) polarimetry. The experimental setup is illustrated in Figure 3.2. In this technique, pulses of linearly polarized light at the fundamental wavelength (λ_0=1266 nm) are incident on the sample at an oblique angle (θ). The transmitted SH signal is collected and spectrally filtered to remove the fundamental wavelength. A calibrated CMOS camera, placed behind a polarization analyzer, measures the generated transverse electric (TE) and transverse magnetic (TM) polarized SH intensities. By rotating a half-wave plate in the incident beam path, the incident polarization is swept, probing the different elements of the second-order susceptibility tensor. Importantly, to extract the nonlinear coefficients from our measurements, we use nonlinear transfer matrix calculations, which fully account for all reflections and the multilayer nature of the samples.[112] Global optimization allows us to find the set of d_{31} and d_{33} parameters that simultaneously reproduce the TE and TM data. We use the undepleted pump approximation given that the conversion efficiency remains well below 1%. The refractive index of MBE-grown ScAlN has been previously reported and has been used to model our films in this study, as listed in Table 3.1 below.

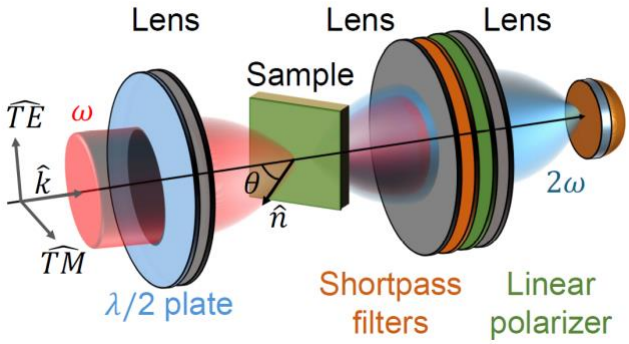


Figure 3.2: (a) Experimental setup for measuring the second-order nonlinear optical response of the samples. The setup includes a half-wave plate ($\lambda/2$) to control the polarization of the incident light, lenses to focus and collimate the beam, shortpass filters to remove the fundamental frequency, a linear polarizer to analyze the polarization of the second harmonic signal, and a detector to measure the SHG intensity.

To confirm the second-order nature of the nonlinearity and extract the nonlinear coefficients of our ScAlN films, we performed second harmonic generation (SHG) power dependence and polarimetry measurements. Figure 3.3(a) shows the quadratic dependence of the TM-polarized SH pulse energy as a function of the TM-polarized pump pulse energy for films with varying scandium concentrations. The observed linear relationship on a log–log scale, with fitted slopes (Δ) close to 2, confirms the quadratic dependence characteristic of a second-order nonlinear process. Furthermore, the SH intensity clearly increases with increasing scandium concentration, suggesting an enhancement of the second-order nonlinearity. This trend is also evident in the polarimetry patterns shown in Figures 3.3(b) and (c) for TM and TE polarizations, respectively, at an incidence angle of 60 degrees. For ease of comparison between samples, these polar plots show the amplitude of the SH electric field, normalized by the square of the incident electric field and the ScAlN film thickness, as a function of the incident polarization angle. The solid curves represent the fitted patterns obtained from our nonlinear transfer matrix simulations. These accurately reproduce the experimental data and enable the extraction of nonlinear coefficients.

Table 3.1: Refractive index of ScAlN at varying scandium concentrations. The data is given at the second harmonic wavelength (λ = 633 nm) and pump wavelength (λ = 1266 nm).

Concentration (%)	$n_{\lambda=633\ \text{nm}}$	$n_{\lambda=1266\ \text{nm}}$
0%	2.06	2.03
10%	2.1	2.07
20%	2.17	2.13
30%	2.27	2.21

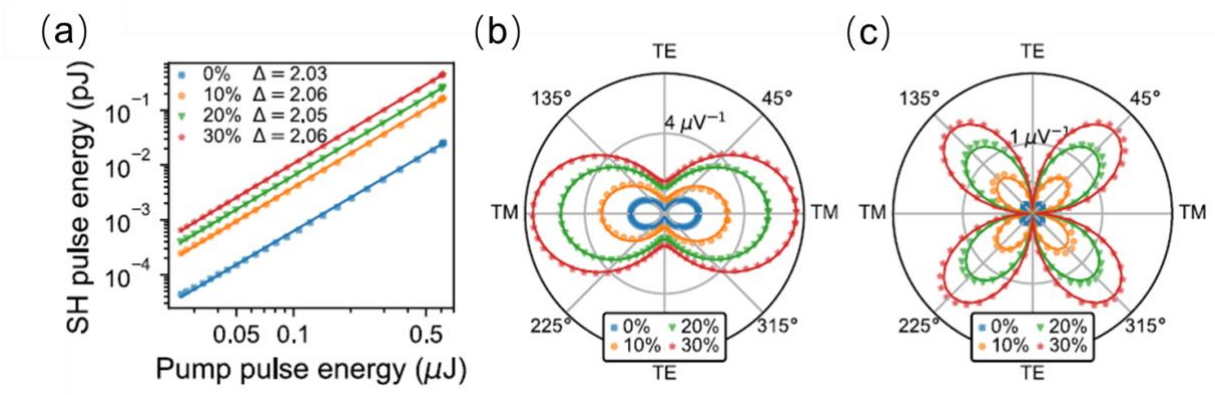


Figure 3.3: (a) Generated second harmonic pulses energy as a function the pump pulses energy for films of different concentrations. The values of the fitted slopes (Δ) are very close to the theoretical values of 2 for the second harmonic generation. Second-harmonic generation polarimetry data for different Sc concentration for TM (b) and TE (c) polarizations with a pump wavelength of 1266 nm and an incidence angle of 60 degrees. For comparison purposes, these plots are normalized to show the amplitude of the SHG electric field divided by the square of the incident electric field and the ScAlN film thickness. The solid lines correspond to the nonlinear transfer matrix fits.

From the SH polarimetry measurements, we extracted the d_{31} and d_{33} nonlinear coefficients for our ScAlN films as a function of scandium concentration. These coefficients reveal the impact of scandium substitution on the second-order nonlinearity of AlN. Figure 3.4 shows the extracted values for d_{31} and d_{33}. Our extracted values for AlN are consistent with those reported in the literature, with both values falling within the range of reported values.[55, 107] The values are also summarized in Table 3.2 along with their ratios to the corresponding coefficients for AlN. Remarkably, the experimentally determined d_{31} exhibits an essentially linear increase with scandium concentration, reaching 2.59 pm/V at 30% Sc concentration. This is a 17-fold in-crease in the d_{31} value compared to AlN. This brings the values of d_{31} to a value comparable to that of $LiNbO_3$ ($d_{31} \simeq 3$ pm/V).[105] This enhancement is particularly significant because ScAlN, unlike $LiNbO_3$, is directly compatible with CMOS fabrication processes. The d_{31} coefficient plays a crucial role in various nonlinear optical applications requiring type-I or type-II interactions like polarization-entangled photon generation [113, 114] or active polarization control [115-117]. Moreover, the fact that the d_{31} coefficient enables interactions involving waves of different polarizations provides additional pathways for achieving phase-matching, since the dispersion of waveguide modes of different polarizations typically exhibits different sensitivities to geometric modifications.[118] The use of these types of interaction, with careful dispersion engineering, has proven effective for applications such as polarization-insensitive parametric amplification [119] and efficient frequency conversion [120, 121].

Table 3.2: d_{31} and d_{33} values of ScAlN and their ratios to AlN at varying scandium concentrations.

Concentration	d_{31} (pm/V)	d_{33} (pm/V)	$d_{31}/d_{31,AlN}$	$d_{33}/d_{33,AlN}$
0	0.15 ± 0.02	3.2 ± 0.3	1	1
10%	0.66 ± 0.06	1.3 ± 0.1	4	0.4
20%	1.81 ± 0.03	0.0 ± 0.5	12	0
30%	2.59 ± 0.04	0.3 ± 1.3	17	0.1

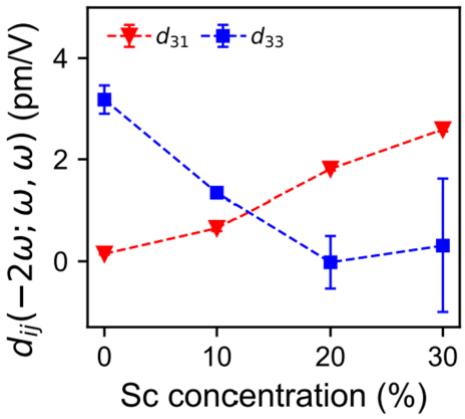


Figure 3.4: Dependence of the second-order nonlinear coefficients d_{ij} of ScAlN on scandium concentration. The red triangle and blue square symbols represent the value of the d_{31} and d_{33} nonlinear coefficient respectively. The values are obtained by averaging over multiple measurements. The error bars show the standard deviation. Note that the error bars for d_{31} are smaller than the markers.

The observed increase in d_{31} with substituent metal concentration has also been reported for sputtered boron- and scandium-substituted AlN.[55, 56, 110] However, the reported enhancement rates (enhancement per % of substituent) for Ref. [56] and Ref. [55] were 2-4 times higher than in this study. Although monocrystalline films grown by MBE generally promise better crystal quality, [122] growing high-quality ScAlN with high scandium content remains challenging as it tends to transition to rock salt phase at higher Sc levels close to 50% [123]. While higher scandium concentrations might further enhance d_{31}, it needs to be balanced with material quality to minimize defect densities and avoid the mixed phase formation of wurtzite and rock salt structures.

At the characterized wavelength of 1266 nm, our measured d_{33} decreases modestly with increasing scandium concentration, accompanied by larger error bars. This rising uncertainty reflects the nature of the SHG measurement in wurtzite crystals like ScAlN: in the TM-polarized

configuration, the in-plane electric field generates the d_{31} contribution to the SHG signal, while the out-of-plane field generates the d_{33} contribution. However, the film's high refractive index causes the out-of-plane field to be much weaker than the in-plane field, so d_{33} contributes less to the overall signal, particularly as Sc content and refractive index further increase. This reduced sensitivity makes it more difficult to extract d_{33} accurately, resulting in greater uncertainty and larger error bars, as shown in Figure 4. To mitigate this, we performed measurements at several angles and implemented a fitting algorithm to ensure consistent d_{31} and d_{33} values across both TM-and TE-polarized data, thereby reducing the impact of experimental noise on the extracted d_{33} values.

This observed d_{33} trend contrasts with the significant (12-fold) increase in d_{33} reported for sputtered ScAlN films with 36% scandium.[56] Given that the measurements were performed on samples grown with different techniques and with different measurement configurations, we also investigated the impact of these parameters. We performed additional measurements on MBE-grown ScAlN on Si (111) with a thin AlN buffer layer and on Si (111) with an aluminum layer for reflection geometry measurements. We also measured a sputtered $Sc_{0.3}Al_{0.7}N$ film in a reflection geometry. The SHG polarimetry measured from these films is plotted in Figure 3.5 (a-b), and the extracted coefficients d_{31} and d_{33} are shown in Figure 3.5 (c-d). These results are qualitatively similar to what we observed with our films grown on sapphire by MBE, showing the same trend for the d_{33}.

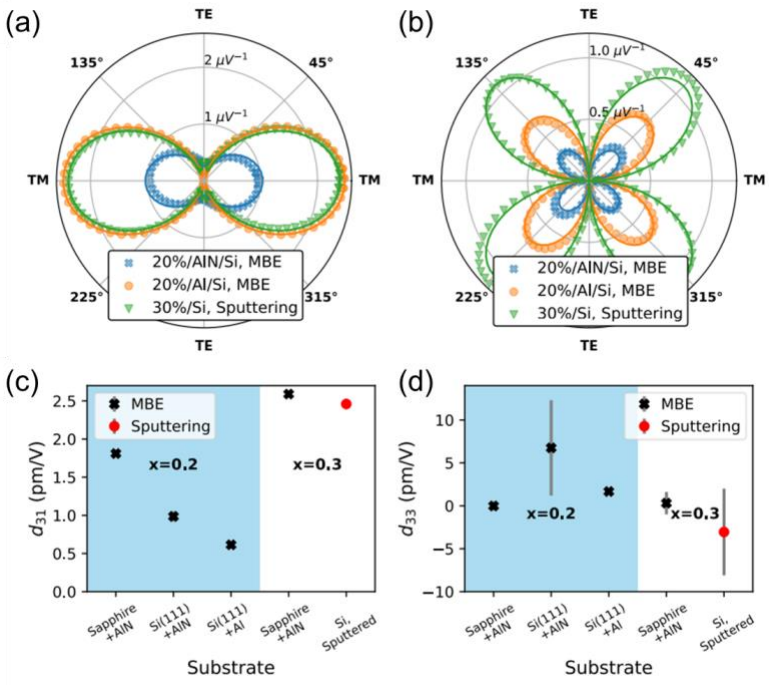


Figure 3.5: (a) TM-polarized and (b) TE-polarized second-harmonic generation polarimetry data for films grown on different substrates and measured in reflection configuration. The film grown directly on Si with 30% Sc content in this comparison (red marker) was grown by sputtering. The incidence angle for these measurements was 67.5 degrees. The data represents the amplitude of the electric field at the second-harmonic frequency normalized by the square of the incident electric field and the ScAlN film thickness. The solid lines represent the fitted patterns. The strength of the signal cannot be directly interpreted in terms of the strength of the nonlinearity because of the different reflectivity of Al and Si. (c) d_{31} and (d) d_{33} coefficients for films with different substrates. The values represent the average extracted nonlinear coefficients for multiple measurements and the error bar represents the standard deviation of the extracted values. The error bars are smaller than the markers for d_{31}.

As a result, several strategies exist to further increase the strength of nonlinearities ScAlN. Our experiments demonstrate a clear correlation between the increase in d_{31} with the higher Sc concentration, corroborating that an even stronger boost in nonlinearity could be achieved when more Sc is alloyed. This could be achieved by tuning the growth conditions to optimize the growth and growing on a more lattice-matched substrate such as GaN. In addition, the creation of superlattice structures offers another potential strategy to increase the nonlinearities attributed to the strong spontaneous and piezoelectric polarizations within III-nitride heterostructures [124], as will be discussed in Chapter 11. These large polarizations can break the symmetry of the quantum well potential, leading to enhanced dipole matrix elements and oscillator strengths in intersubband transitions.[125]

3.4 Conclusion

In conclusion, we have investigated the second-order nonlinear properties of epitaxial ScAlN thin films with varying scandium concentrations. Our results indicate a significant enhancement of the d_{31} nonlinear coefficient, reaching 2.59 pm/V at 30% Sc concentration. Additionally, increasing the d_{33} coefficient appears possible, at either lower wavelengths or higher Sc concentrations than those achieved in our current experimental study. The 17-fold enhancement of d_{31} compared to AlN brings the d_{31} value of ScAlN close to that of lithium niobate, a widely used material for nonlinear optics, while maintaining CMOS compatibility. This makes ScAlN a promising candidate for integrated nonlinear photonic devices such as electro-optic modulators, frequency converters, and sources of entangled photons that rely on off-diagonal elements of the second-order susceptibility. Finally, the observed trend of increasing second-order nonlinearities with scandium content suggests that major improvements may be possible by exploring shorter wavelengths, higher scandium concentrations and heterostructure engineering.

Chapter 4 Second-order Optical Nonlinearity in Scandium-doped Gallium Nitride

4.1 Introduction

Gallium nitride is a pivotal wide bandgap semiconductor for optoelectronic, photonic and electronic applications owing to the direct bandgap of 3.4 eV, high breakdown field, and robust stability to radiation and high temperature.[126-128] By alloying with Al and In, GaN has revolutionized the solid-state lighting and display technology that covers high brightness in UV and visible range.[129] Beyond the light source applications, the wide transparency window from ultraviolet to infrared enables the development of GaN-based integrated passive and active components, such as modulators, frequency converters, and quantum light sources.[130-132] The mature epitaxial growth technology has also enabled such platforms on a variety of common semiconductor substrates, such as silicon, silicon carbide and sapphire.[133-136]

One of the critical characteristics of GaN is its second-order optical nonlinearity. Similar to AlN, GaN also stabilizes at the non-centrosymmetric wurtzite phase, generating an even larger $\chi^{(2)}$ compared with AlN.[137] Several applications have exploited GaN in efficient second-harmonic generation and quantum photonics applications. Additionally, Sc doping in GaN can also flatten the barrier landscape, creating a lower barrier for ferroelectric switching.[138] Wang *et al.* has experimentally demonstrated ferroelectric switching in ScGaN grown by MBE.[61]

As discussed in Chapter 1, the mixing enthalpy determines the ScAlN favors wurtzite structure only with Sc concentrations below ~50%, as calculated by Zhang *et al.* [123] Higher Sc incorporation can generate a pure cubic or a mixed phase, which is less ideal for the applications that exploit the wurtzite structure of III-nitrides. However, theoretical calculations shown that the wurtzite ScGaN can stabilize with Sc concentrations beyond 60%, providing a wider tunable window for its physical properties and may provide a stronger enhancement in its piezoelectricity. Yang *et al.* has recently achieved single-crystalline wurtzite ScGaN films by MBE with Sc concentrations up to 48%.[139]

Chapter 3 has shown that the scandium doping in aluminum nitride can enhance the second-order optical nonlinearity, possibly due to the lattice distortion. Since GaN also stabilizes in a wurtzite phase, it is expected to see a similar enhancement in Sc-doped gallium nitride (ScGaN). In this chapter, we will systematically investigate the impact of Sc-doping in GaN on its second-order optical nonlinearity.

4.2 Epitaxial Growth of ScGaN

To obtain high-quality ScGaN films with controlled thickness, composition and pure phase, we have grown the ScGaN in a plasma-assisted molecular beam epitaxy (PA-MBE). The system is loaded with high purity sources of Sc (99.999% purity), Al (99.99995% purity) and Ga (99.99999% purity). Active nitrogen species are provided by an RF source with 99.9999% nitrogen supplied. To complete a comprehensive study on several critical optical characteristics of the ScGaN films, ScGaN with different Sc compositions were grown on sapphire substrates with a thin layer of aluminum nitride in between to serve as the buffer layer to reduce the lattice mismatch and dislocation density. The AlN layer is thin and has a much wider bandgap compared with GaN, which would minimize the measured signals between the ScGaN and the AlN buffer layer. To achieve a smooth surface in AlN for better epitaxy of ScGaN, AlN was grown under metal-rich conditions. Then, the ScGaN was grown under a nitrogen-rich condition. Similar to ScAlN, the nitrogen-rich environment prevents the formation of intermetallic and promotes the pure wurtzite phase crystallization. The final structure is illustrated in Figure 4.1(a). In-situ reflection high-energy electron diffraction (RHEED) monitoring were used during the growths to confirm the formation of wurtzite ScGaN growth throughout the epitaxy.

The grown samples were then characterized by X-ray diffraction in a Rigaku SmartLab tool equipped with a Cu $K_{\alpha 1}$ source. The 2θ-ω scan results are plotted in Figure 4.1(b) for $Sc_xGa_{1-x}N$ with x= 0.2, 0.3 and 0.4. Within these compositions, as the single ScGaN (002) peak shown in the XRD plot, it is confirmed to be a pure wurtzite structure without mixed phase with other cubic structures not having a composition separation. In this work, the Sc compositions are confirmed by the energy-dispersive X-ray spectroscopy (EDX). Since the substrates are sapphire (Al_2O_3) and AlN, the Sc and Ga signals should solely from the ScGaN.

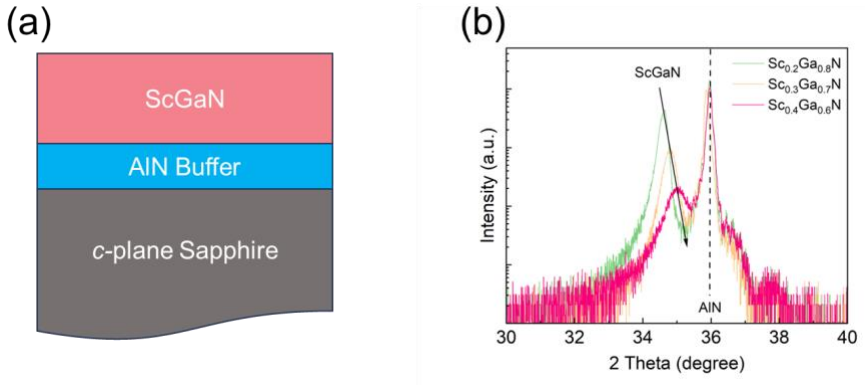


Figure 4.1: (a) Structural illustration of the epitaxial ScGaN/AlN on sapphire used in this study. (b) X-ray diffraction pattern on the 2θ-ω scan on the grown samples with Sc compositions of 20%, 30% and 40%.

4.3 Optical Bandgap Characterization of ScGaN

The wide bandgap shown in GaN is an important property affecting its applications in electronic, photonic, and optoelectronic devices. In ScAlN, it has been found that the Sc-doping will decrease the AlN bandgap slightly.[35] However, the bandgap changing in Sc-doped GaN remains elusive. There are several research investigated the bandgap of ScGaN by photoluminescence or UV-visible transmission, yet the results are rather scattered between the studies.[140, 141] To get the bandgap of ScGaN grown by MBE with a controlled phase and composition, we performed the UV-visible transmission with a home-built optical setup. A broadband UV-visible light source was collimated to the sample mounted on a stage, and the transmitted light was collected by a spectrometer. A reference sample of sapphire substrate with the same thickness of AlN grown on top was measured as well to account for the spectral response of the light source, optics, detectors, and the absorption by the AlN-on-sapphire substrate. The transmission spectrum was then normalized with the reference sample to ensure the measured transmission or absorption are from the top ScGaN layer only.

To extract the optical bandgap, the transmission spectra were converted to an absorption coefficient αhv with Eq. 4.1:

$$\alpha = -\frac{1}{d}\ln T \tag{4.1}$$

where d is the layer thickness, confirmed by cross-sectional SEM as the same method mentioned the Chapter 3, T is the transmission acquired from the measurement. Tauc plots were then

generated by plotting the $(\alpha hv)^2$ as a function of the photon energy hv for each Sc composition. The bandgap can be determined by extrapolating the fitted line to the photon energy axis, on which the intercept is the bandgap E_g. Preliminary results on the extracted bandgaps are plotted in Figure 4.2. A clear increase in the optical bandgap is observed in the ScGaN films with increasing Sc concentrations. This is in contrast with the case in ScAlN, where the bandgaps are reduced with the Sc doping in AlN. This suggests that transparency window of GaN can be further widened with the Sc doping with other properties such as piezoelectricity and ferroelectricity get enhanced at the same time.

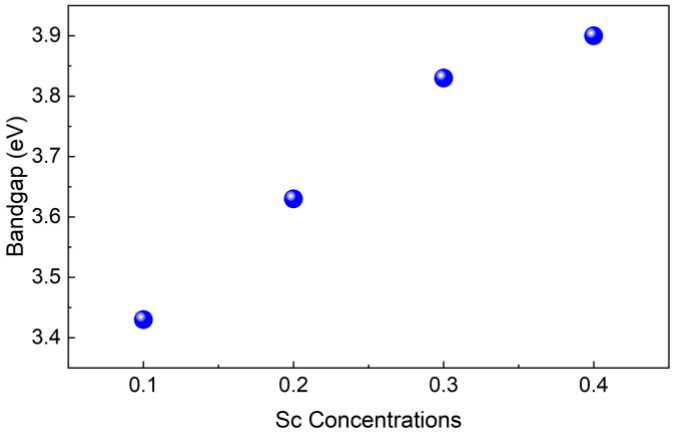


Figure 4.2: Extracted optical bandgap E_g with 10%- 40% Sc incorporation.

4.4 Second-order Optical Nonlinear Characterization of ScGaN

To further investigate the second-order optical nonlinearity in ScGaN, we used the same method introduced in Chapter 3 to quantify the $\chi^{(2)}$ of ScGaN. A set of samples have similar structure as shown in Figure 4.1(a) were used for the measurement with thicker ScGaN films grown to amplify the signal ratio of ScGaN over the AlN buffer layer. A fundamental laser with wavelength at 1266 nm was used to generate 633 nm second-harmonic signals. Transmission geometry was used and the SHG intensity was recorded as a function of input polarization and sample azimuth to fit the nonlinear susceptibilities. Same as ScAlN and AlN, ScGaN crystal has the 6*mm* space group and the effective coefficients are reduced to two terms, d_{31} and d_{33}.

The tested samples have Sc compositions up to 35% and the fitted d_{31} and d_{33} values are plotted below in Figure 4.3. Note the preliminary analysis assumed ScGaN have similar refractive

index to GaN, as reported in the Ref. [142]. It is shown that there is a continuous increase of d_{31} with higher Sc doping, and when doping level is at 35% Sc, a ~2.5 enhancement can be observed in d_{31} compared to GaN, reaching 6.2 pm/V. The mechanism behind such enhancement may be similar to ScAlN and BAlN where there is larger projection of the susceptibility terms on the basal plane, contributing an increased d_{31} yet less effective for d_{33} where the trend is less monotonic with a transition near zero within a medium level Sc concentration and have a sudden increase with higher Sc incorporation around 35%.

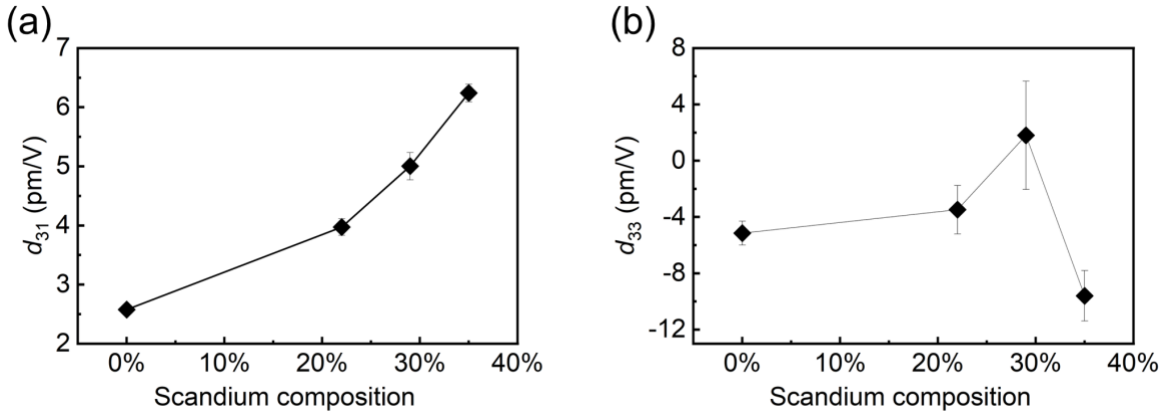


Figure 4.3: (a) Extracted d_{31}, and (b) d_{33} values in ScGaN with Sc composition up to 35%.

4.5 Conclusion

In this chapter, we have confirmed that the second-order optical nonlinearity can be enhanced not only in ScAlN, not extend to the ScGaN, with an additional benefit of larger optical bandgap to widen the operating wavelength range. Additionally, the d_{31} values are even larger than ScAlN and $LiNbO_3$, suggesting huge potential in its applications in quantum photonics. By leveraging the strong $\chi^{(2)}$ shown in ScGaN, we expect its further powerful integration with the lighting and high-power electronics that have been well-established on the GaN platform.

Chapter 5 Hybrid ScAlN/Si_3N_4 Platform for Low-Loss Integrated Photonics

5.1 Introduction

With the extensively studied optical nonlinearity studied in Chapter 3, we explore further applications of ScAlN in integrated photonics. Integrated photonics has been developed as an emerging field to integrate diverse optical and photonic functionalities, including light generation, modulation, sensing, filtering, and computing, onto a compact platform with footprints scaled down to the order of optical wavelengths.[143-145] The fundamental performance of these integrated photonic devices is critically dictated by the choice of material platforms. Silicon nitride (Si_3N_4) has garnered significant attention and developed into a superior candidate, particularly for passive components and nonlinear optical applications that exploit third-order nonlinearity.[146, 147] Its compatibility with established CMOS fabrication process enables seamless integration with electronic components while supporting high-volume manufacturing. Furthermore, it exhibits exceptionally low optical loss,[148] boasting intrinsic quality factors (Q_i) on the order of 10^7 in microring resonators and propagation losses as low as 0.1−1 dB/m across a wide transparency window from the visible to the mid-infrared.[149] This ultra-low loss is essential for reducing signal attenuation over extended optical paths and fostering high-Q resonant cavities crucial for narrow-linewidth lasers [150, 151], filters [152, 153], and comb generation [154, 155]. However, a significant limitation of Si_3N_4 stems from its centrosymmetric crystal structure, which inherently causes the absence of second-order ($\chi^{(2)}$) nonlinear optical effects, preventing efficient electro-optic modulation and second harmonic generation required by active functionalities.

Alternatively, extensive research on lithium niobate ($LiNbO_3$) has been conducted for high-performance active photonic components due to its pronounced second-order optical nonlinearity and electro-optic coefficients.[53, 156] These properties enable efficient light modulation [157-159], second harmonic generation [101, 160, 161], and optical parametric oscillation [162, 163],

The content of this chapter has been submitted to *ACS Photonics*. The work is supported by the Army Research Office under Grant No. W911NF2420210 and National Science Foundation under Grant No. 2435166, No. 2326780, No. 2330310, and No. 2317471, and by the College of Engineering at the University of Michigan.

making it integral to the high-speed modulators in optical communication systems. While traditional bulk $LiNbO_3$ devices were large and challenging to integrate, recent advancements in thin-film lithium niobate (TFLN) technology have enabled highly confined waveguides and compact devices. However, there are several challenges associated with $LiNbO_3$. Direct epitaxial growth of thin TFLN has been limited by the crystalline quality and thickness control. Therefore, most early works on $LiNbO_3$ devices were built upon bulk substrate, posing challenges for compact integration. Despite techniques such as smart cut that have been developed to produce TFLN, challenges remain in achieving high-quality and uniform films across a large area.[164] Additionally, the absence of $LiNbO_3$'s direct CMOS compatibility often requires complex heterogeneous integration schemes in the fabrication process. Furthermore, $LiNbO_3$ typically exhibits higher propagation loss than Si_3N_4, limiting its prospect in loss-sensitive quantum photonics applications. These inherent trade-offs have consistently spurred the development of other material platforms that can offer second-order nonlinear properties and active functionalities while maintaining full CMOS-compatibility and low optical loss.

In this context, aluminum nitride (AlN) has gained increasing interest. AlN is stable in the non-centrosymmetric wurtzite structure and naturally possesses piezoelectric properties and second-order optical nonlinearity.[44, 165] While primarily known for its applications in deep-UV optoelectronics and high-power electronics, its piezoelectricity and optical properties also position it as a competitive platform for integrated photonics.[46, 47, 166, 167] However, the intrinsic second-order nonlinearity of AlN is relatively weak, limiting the efficiency of nonlinear optical processes.

Building upon AlN, scandium aluminum nitride (ScAlN) has emerged as a particularly promising platform for high-performance integrated photonics. Alloying scandium (Sc) into the AlN lattice, as illustrated in Fig. 5.1(a), offers a unique pathway to significantly enhance its properties via material engineering.[59, 72] ScAlN maintains the wurtzite crystal structure over a wide range of Sc compositions up to about 50%, before transitioning to a cubic phase.[168] The incorporation of Sc has led to the emergence of ferroelectricity, and a dramatic increase in both piezoelectricity and, more importantly in terms of photonic applications, the second-order optical nonlinearity.[16, 22, 23, 56, 76, 169] Experimental studies have shown that ScAlN exhibits the second-order nonlinearity an order of magnitude stronger than its pure AlN counterpart. This enhanced property paves a robust path for highly efficient second harmonic generation and

cascaded second-order processes for comb generation. Additionally, the emergence of ferroelectricity and greatly enhanced piezoelectricity in ScAlN allows for highly efficient electromechanical transduction, enabling the design of integrated acousto-optic devices for high-speed modulation, frequency shifting, and optical filtering. Recent studies have also suggested that ScAlN can achieve a large electro-optical coefficient, potentially exceeding 50 pm/V at high Sc compositions to surpass that of the conventional $LiNbO_3$ platform.[124, 170] These outstanding electro-optic and nonlinear optical properties collectively position ScAlN as a superior platform for next-generation high-speed optical modulators, frequency converters, and quantum optical sources to propel optical communication and computing into a new era. Despite the significant potential of ScAlN, prior efforts in developing passive and active components on this platform have predominantly relied on sputtered ScAlN films. While sputtering offers good deposition rates, it often results in polycrystalline films with higher scattering losses and reduced *Q* factor.[171] In this work, we address this limitation by developing a hybrid Si_3N_4 and ScAlN platform, wherein single crystalline ScAlN is epitaxially grown by molecular beam epitaxy to achieve lower loss, yielding an intrinsic *Q*-factor of more than 3×10^5, significantly higher than previously reported values for monolithic ScAlN platforms.[110, 171] The meticulously designed hybrid structure aims to combine the ultra-low loss characteristics of Si_3N_4 with the powerful nonlinearity and enhanced piezoelectricity provided by ScAlN.

5.2 Materials Growth and Characterizations

The fabrication begins with a sapphire (Al_2O_3) substrate serving as the bottom cladding layer. A 90 nm AlN layer is grown on the sapphire substrate to facilitate the growth of epitaxial ScAlN, which is critical for minimizing dislocation density and consequently reducing optical loss in the active material. A 200 nm layer of $Sc_{0.1}Al_{0.9}N$ is then epitaxially grown by plasma-enhanced molecular beam epitaxy (PA-MBE) plasma-enhanced molecular beam epitaxy (PA-MBE) under ultra-high vacuum to minimize the impurity incorporation and provide good crystallinity for enhanced optical properties. Atomic force microscopy characteristic as shown in Figure 5.1(b) reveal a surface roughness of 1.2 nm. The scandium incorporation into the AlN lattice introduces distortion in the lattice and modifies the growth dynamics compared with AlN, leading to an increased surface roughness. Further cross-sectional transmission electron microscopy (TEM) and energy dispersive X-ray spectroscopy (EDX) as shown in Figure 5.1(c) clearly show uniform scandium incorporation in the ScAlN layer.

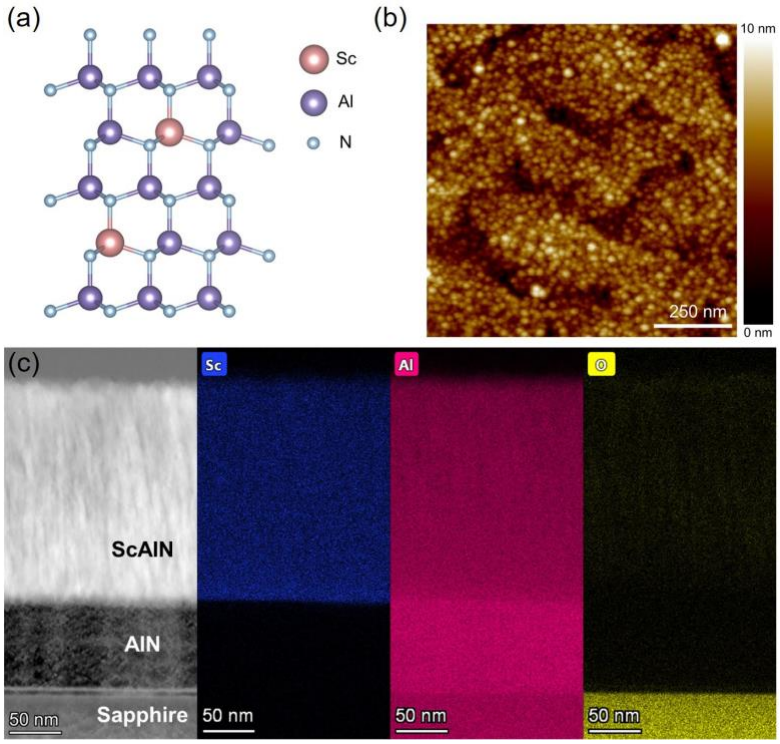


Figure 5.1: Materials characterization of ScAlN. (a) Crystal structure illustration of Sc-alloyed AlN. (b) Atomic force microscope imaging of the ScAlN surface showing a roughness of 1.2 nm. (c) Cross-sectional STEM and EDS mappings of the Si_3N_4/ScAlN/AlN/Sapphire structure.

5.3 Device Design and Numerical Simulation

A major barrier to the widespread adoption of ScAlN is dictated by loss stemming from two sources, material absorption of ScAlN and scattering due to sidewall roughness arising from the etching resistivity. The design presented in this paper, shown in Figure 5.2(a), mitigates the first source by controlling the wave's confinement within the ScAlN layer and side-steps the second by leaving the ScAlN un-etched. This design integrates low-loss Si_3N_4 with ScAlN and AlN to form a hybrid waveguide that can take advantage of the superior properties of ScAlN while reducing loss, thereby rendering it a promising platform for all-rounder PICs.

An important design consideration for the hybrid structure is the ratio of the etched Si_3N_4 layer thickness to the thickness of the slab layer of III-N materials. Due to the higher index of ScAlN and AlN in comparison with Si_3N_4, a significant portion of the light is confined within the slab layer. This is qualitatively manifested by the simulated mode profiles of the fundamental TE and TM modes as shown in Figure 5.2 (b) and (c) respectively. Quantitatively, the confinement factor in ScAlN is plotted in Figure 5.2 (f), with a comparison of material confinement factors for TE and TM polarization shown in Table 5.1. The group index of the fundamental modes as shown in Figure

5.2(d) and confinement factors are determined in COMSOL Multiphysics. The definition of confinement factor is shown below where $\iint_X dA$ represents an integral over a 2D region X and $\iint dA$ represents a 2D integral over all space.

$$\Gamma_X = \frac{\iint_X |E|^2 dA}{\iint |E|^2 dA} \tag{5.1}$$

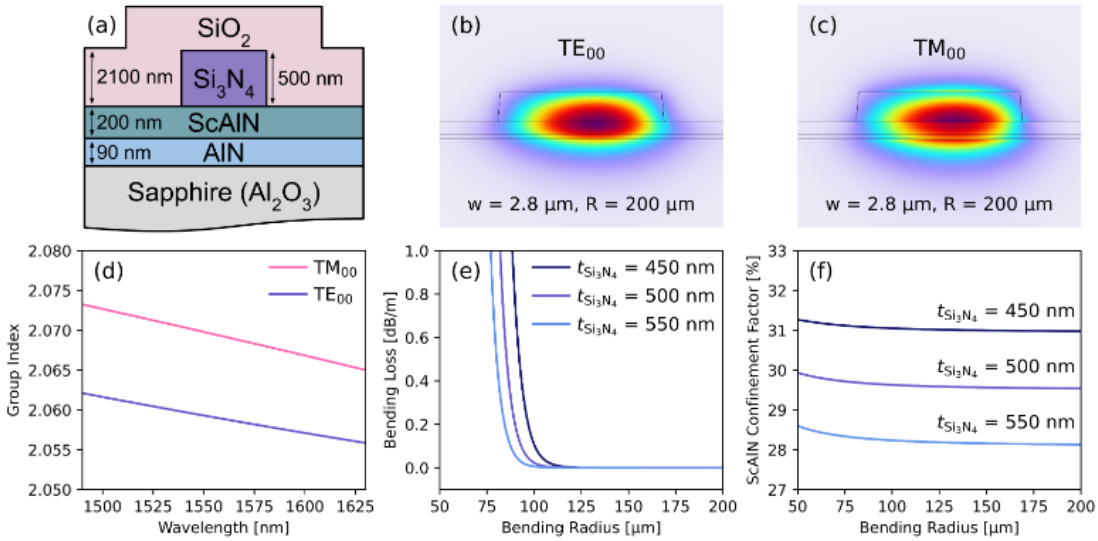


Figure 5.2: Waveguide design and simulated optical characteristics. (a) Geometry and dimensions for Si_3N_4-ScAlN hybrid guiding structure. Fundamental TE_{00} (b) and TM_{00} (c) mode distributions (|E|) in a ring configuration. (d) Group index (n_g) for the modes shown in (b) and (c). Bending loss (e) and confinement factor within ScAlN (f) for the TE_{00} mode with respect to bending radius for different thicknesses of Si_3N_4 at a guide width of 2.8 μm.

ScAlN layer being only less than half as thick as the Si_3N_4 layer (200 nm versus 500 nm). Table 5.1 shows that the confinement of the fundamental TE mode within the ScAlN layer alone is around 60% that of the Si_3N_4 layer, while its physical thickness is only 40% of that of Si_3N_4. This confinement is further increased with a reduction in Si_3N_4 thickness, albeit coming at the cost of increased bending loss. Since the III-N layer is un-etched, no lateral confinement is present in those layers, allowing for lateral leakage of the mode during strong bending. The interplay between the thickness of Si_3N_4, confinement within the ScAlN layer, and loss is a key parameter of this structure subject to optimization. Some of these dynamics displayed in Figs. 5.2(e) and (f) illustrate the effect of Si_3N_4 thickness on bending loss and confinement across a range of bending radii. The fabricated devices discussed in the following sections keep the thickness of Si_3N_4 at 500 nm, providing a confinement factor of $\Gamma_{ScAlN} \approx 30\%$ for the fundamental TE mode.

Even though the higher index of ScAlN serves to increase confinement within the ScAlN layer for TE modes, a more complex dynamic nonetheless emerges for the TM modes, suggesting reduced confinement within the ScAlN layer for TM modes compared to TE modes, as evidenced in Table 1. This is because the sub-wavelength nature of the ScAlN and AlN layers form a light inverse slot mode, which may increase scattering loss from greater interaction with the waveguide boundary while reducing material absorption due to reduced confinement with the layers with higher propagation loss.

Table 5.1: Confinement Factors for Fundamental TE and TM Modes [a].

Polarization	$\Gamma_{Si_3N_4}$	Γ_{ScAlN}	Γ_{AlN}
TE_{00}	47.4%	29.5%	8.6%
TM_{00}	45.0%	23.0%	7.8%

[a] For $\lambda = 1550$ nm, $w = 2.8$ μm

5.4 Device Fabrication and Measurements

To fabricate the monolithically integrated Si_3N_4-ScAlN photonic chips, we employ a recently developed amorphous silicon (a-Si) hardmask dry etching technique, enabling high-selectivity and smooth-etched Si_3N_4 waveguides.[172] The full fabrication flow is illustrated in Figure 5.3(a). The process begins with the MBE-grown ScAlN film on 2-inch single-crystal AlN-on-Al_2O_3 wafer. On top of this substrate, a 500-nm-thick stoichiometric Si_3N_4 layer is deposited via low-pressure chemical vapor deposition (LPCVD), followed by the deposition of a 700-nm- thick a-Si layer as hardmask. Electron beam lithography (EBL) is then performed using MaN-2405 resist, with a beam current of 2 nA, a step size of 8 nm, and exposure dose of 700 $\mu C/cm^2$. After resist development, a thermal reflow process is applied on a hotplate to smooth the resist edges and reduce line-edge roughness. The resulting resist pattern is first transferred to the a-Si hardmask via reactive ion etching (RIE) using HBr and He gases. After removing the residual resist, the pattern is etched into the underlying Si_3N_4 layer using RIE with a gas mixture of C_4F_8, CF_4, and He. This etch yields waveguides with smooth and nearly vertical sidewalls. The a-Si hardmask is subsequently removed using XeF_2 vapor etching, and a SiO_2 top cladding is deposited by plasma-enhanced chemical vapor deposition (PECVD). As only the Si_3N_4 layer is patterned and etched to define the waveguide, the underlying ScAlN and AlN layers remain intact, avoiding direct etching

of these hard-to-etch materials. The scanning electron microscopy (SEM) image in Figure 5.3(b) confirms the smooth waveguide sidewalls, indicative of low optical propagation loss. As discussed in the numerical simulations, the rib-like waveguide geometry, shown by the cross- sectional SEM image in Figure 5.3(c), enables tight optical mode confinement within the ScAlN layer, while simultaneously benefiting from the low optical loss provided by the high-quality Si_3N_4 waveguides.

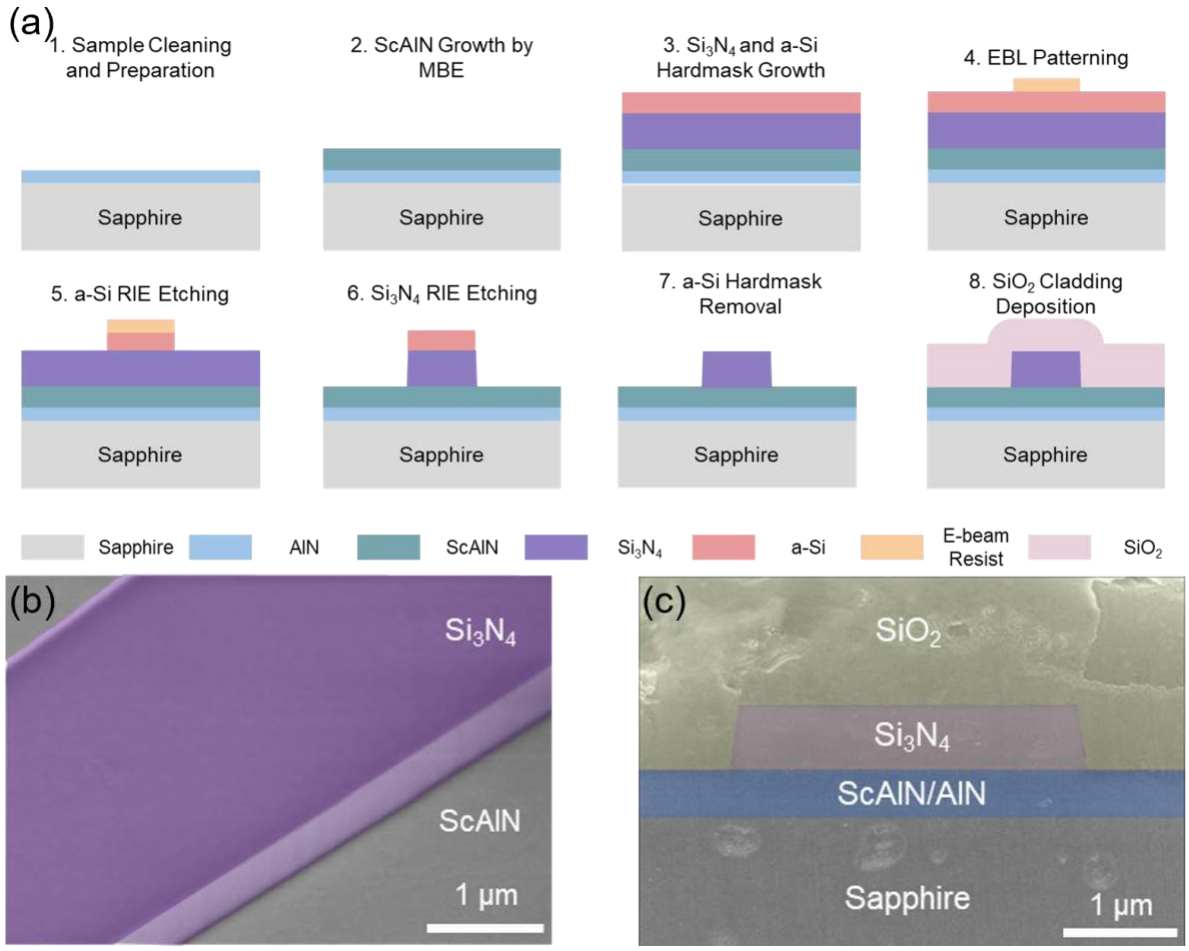


Figure 5.3: Fabrication of the Si_3N_4–ScAlN photonic chips. (a) Fabrication flow of the monolithically integrated Si_3N_4-ScAlN waveguides. (b) False-colored scanning electron microscopy (SEM) image of the device after Si_3N_4 etching showing a smooth sidewall. (c) False-colored cross-sectional SEM of the fabricated waveguide.

We characterize the propagation loss of the fabricated Si_3N_4-ScAlN microring resonators by measuring their optical transmission spectra using a standard fiber-to-chip edge coupling setup. A narrow-linewidth tunable laser source (TSL-770) is coupled into the chip via a lensed fiber and guided into the microring resonator. The transmitted light is then collected by another lens fiber, detected by a low-noise photodetector (Newport 1811), and read out using an oscilloscope. Figure

5.4(a) shows the microscope image of a fabricated microring resonator with a radius of R = 200 μm and a waveguide width of w_R = 2.8 μm. The straight bus waveguide is single-point coupled to the microring with a gap of 500 nm. To ensure good phase matching with the fundamental resonance mode of the microring, the bus waveguide width is set to w_B = 2.0 μm. The measured normalized transmission spectra for TE modes are presented in Figure 5.4(b).

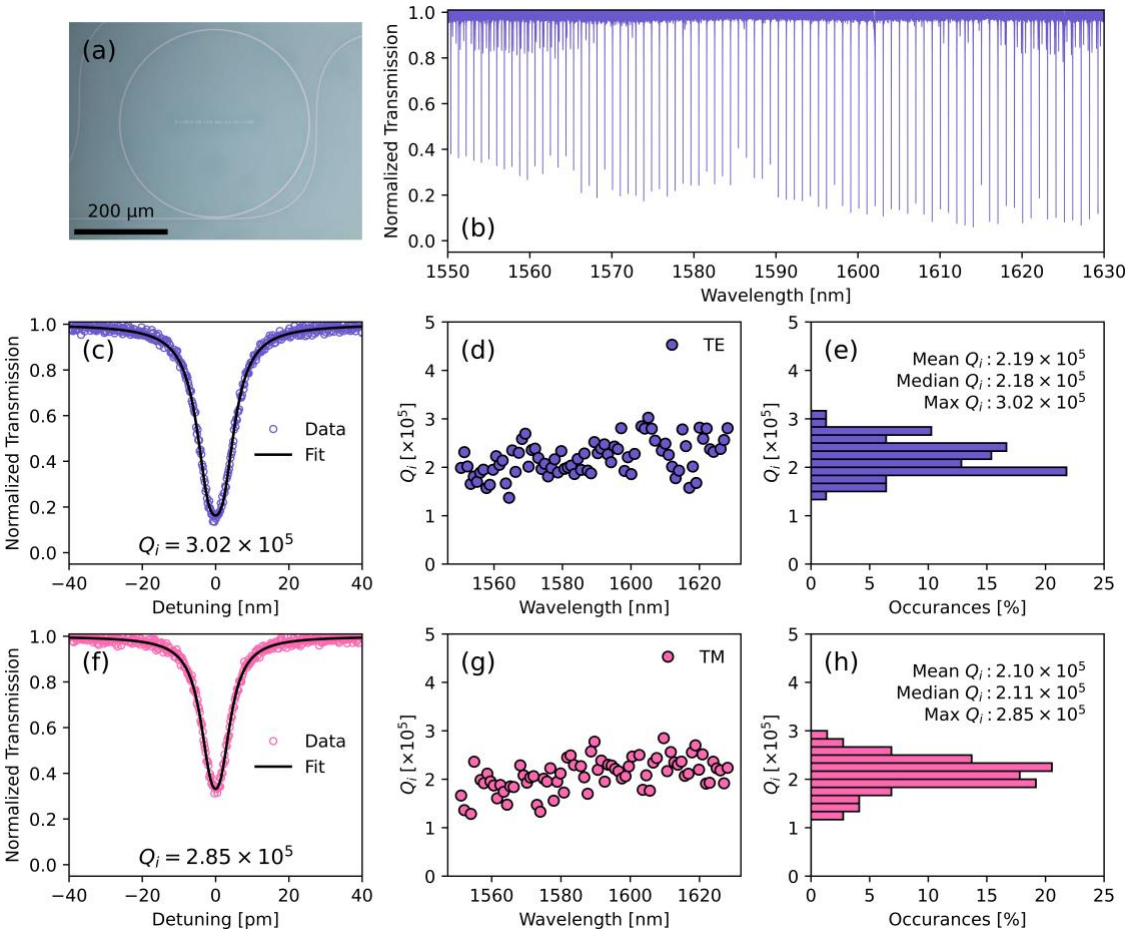


Figure 5.4: Optical loss characterization of the circular microring resonator. (a) Microscope image of the fabricated Si_3N_4-ScAlN microring resonator (R = 200 μm, w_B = 2.8 μm). (Scale bar) (b) Normalized transmission spectrum for TE polarization for 1550 to 1630 nm. Fitted highest Q_i resonances for TE (c) and TM (f) polarizations, with $Q_i = 3.02 \times 10^5$ and $Q_i = 2.85 \times 10^5$ corresponding to propagation losses of α = 1.16 dB/cm and α = 1.23 dB/cm respectively. Fitted Q_i trend with wavelength for TE (d) and TM (g) polarizations. Fitted Q_i distributions for TE (e) and TM (h) polarizations.

We then extract the Q factors by fitting each resonance in the measured transmission spectra, following a similar procedure to that reported in Ref. [172] and [173]. We assume that all resonances operate in the under-coupled regime ($Q_i < Q_c$), where Q_i accounts for all intrinsic losses, including material absorption and scattering loss, and Q_c denotes the coupling Q factor associated with waveguide-to-resonator coupling loss. Fig. 5.4(c) shows an example of the fitted high-Q

resonance for the TE_{00} mode near λ_0 = 1605.1 nm, yielding a high Q_i = 3.02 × 10^5. The corresponding propagation loss is calculated using Eq. 5.2:

$$\alpha = \frac{2\pi n_g}{Q_i \lambda_0} \tag{5.2}$$

where the group index is n_g = 2.06, resulting in a propagation loss of α = 1.16 dB/cm. Figure 5.4(d) summarizes all extracted Q_i values across the 1550-1630 nm wavelength range, each fitted with a goodness-of-fit (R-square) exceeding 95%. The statistical distribution of the extracted Q_i factors is presented in Figure 5.4(e), showing a mean high Q_i = 2.19 × 10^5. For TM modes, the max Q_i reaches 2.85 × 10^5 (in Figure 5.4(f)) near λ_0 = 1609.7 nm, corresponding to a propagation loss of α = 1.23 dB/cm. Figs. 5.4(g) and 5.4(f) show the corresponding extracted Q_i values and their statistical distribution, with a mean Q_i = 2.10 × 10^5. Compared with the previously reported maximum Q_i of approximately 1.5 × 10^5 for pure ScAlN waveguides, our consistently high-Q factors highlight the robustness of monolithic Si_3N_4-ScAlN design and the fabrication process, enabled by both the high crystalline quality of the MBE-grown ScAlN film and the low-loss etching of the Si_3N_4 waveguides. To further reduce optical loss in the microring resonator, we implement a Euler racetrack design consisting of two straight waveguide sections connected by 180° adiabatic Euler bends at both ends.[174, 175] The straight waveguide segments confine the optical mode in the waveguide center, thereby minimizing interaction with the sidewalls and reducing scattering loss compared to conventional circular microrings. The Euler bends provide an adiabatic curvature transition between the straight and curved sections to help suppress the mode mismatch induced coupling from fundamental to higher-order modes typically associated with larger optical loss. An optical microscope image of the fabricated Euler racetrack microresonator is shown in the inset of Figure 5.5(a). The effective bending radius of the Euler curves is R_{eff} = 125 μm, offering a balance between negligible bending loss (as shown in Figure 5.2(e)) and a compact footprint. We design the straight waveguide sections with a length of L_s = 450 μm, resulting in a total cavity length of L = 2041 μm. The bus and resonator waveguides share identical width (w_B = w_R = 2.6 μm) and remain straight in the coupling region to naturally satisfy the perfect phase-matching condition over a broad wavelength range. Together with the adiabatic Euler bends, this configuration enables efficient excitation and low-loss propagation of the fundamental modes within the resonator. The bus-to-resonator gap is g = 600 nm with a coupling length of L_c = 50 μm.

Figure 5.5(a) shows the normalized transmission spectrum of the TE modes in the Euler racetrack microresonator operating in the slightly over-coupled regime ($Q_i > Q_c$). Owing to the incorporation of long straight waveguide sections, the max intrinsic quality factor improves to $Q_i = 3.35 \times 10^5$, as evidenced by the fitted resonance shown in Fig. 5.5(b). At the resonance wavelength of $\lambda_0 = 1616.97$ nm with a group index of $n_g = 2.05$, the calculated propagation loss $\alpha = 1.03$ dB/cm. This low propagation loss compares favorably with the 1–2 dB/cm of single-mode silicon waveguides on the well-established commercial 220-nm silicon-on-insulator (SOI) platform [176, 177] that have enabled some of the most advanced PICs for emerging applications in high-speed data centers and optical communications. The demonstrated performance of our hybrid Si_3N_4-ScAlN platform thus offers competitive low-loss characteristics suitable for next-generation integrated photonics, while also featuring additional functionalities including high $\chi^{(2)}$ nonlinearity, ferroelectricity, and piezoelectricity. It is also evident from Figure 5.5(c) and (d) that this high quality factor is not an outlier, as corroborated by a tight distribution of high intrinsic quality factors that exhibits a large mean value of $Q_i = 2.94 \times 10^5$, indicating the robustness of the low-loss performance of these Si_3N_4-ScAlN PICs.

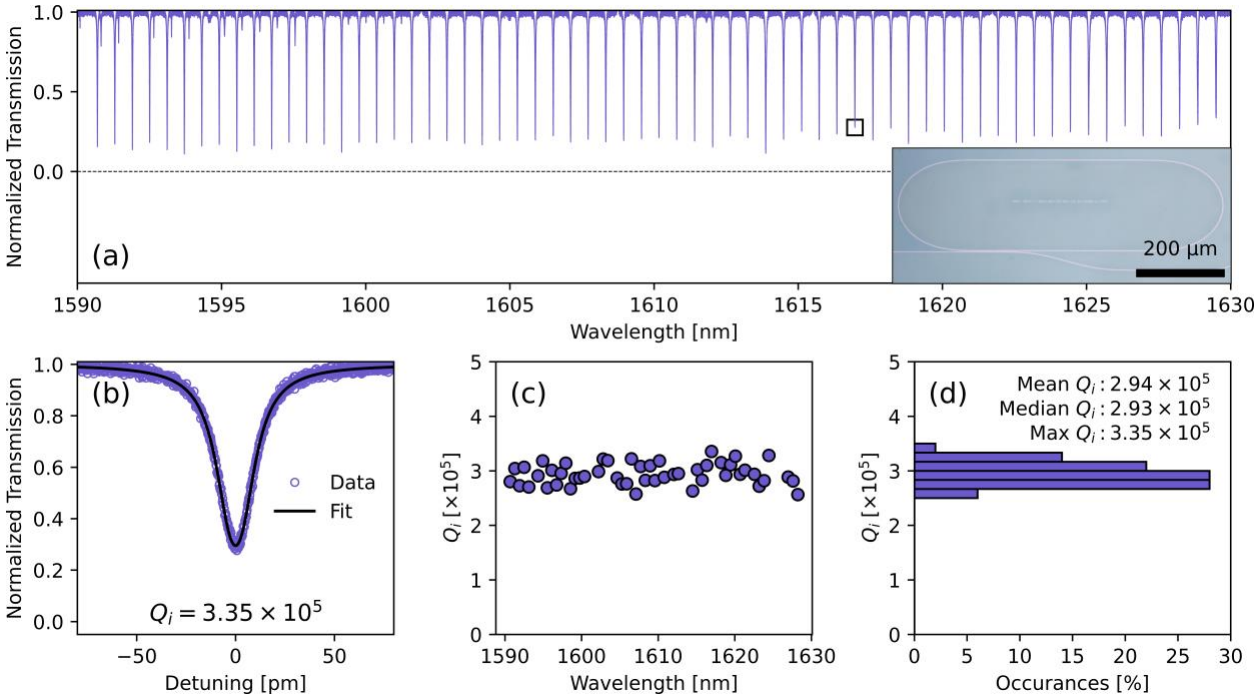


Figure 5.5: Optical loss characterization of the Euler racetrack microring resonator. (a) Normalized transmission spectrum from 1590 nm to 1630 nm for TE polarization, with highest Q_i resonance highlighted and Euler-bend racetrack resonator ($R_{eff} = 125$ μm, $w = 2.6$ μm) inset. (b) Fitted highest intrinsic quality factor resonance for TE polarization, with

$Q_i = 3.35 \times 10^5$ corresponding to a propagation loss of $\alpha = 1.03$ dB/cm. Dots: experiment data. Solid line: fitting. (c) Fitted Q_i trend with wavelength for TE polarization. (d) Fitted Q_i distribution for TE polarization.

Figure 5.6 compares the Q-factor of ring resonators based on the hybrid ScAlN/Si_3N_4 structure with those of monolithic ScAlN platforms, [23, 110, 170, 171, 178-182] showing a clear reduction in terms of propagation loss in the hybrid device. To date, most of the ScAlN-based photonic devices demonstrated focus on the operation in the telecom band near 1550 nm. However, the ultrawide bandgap of ScAlN provides a transparent window over a broad wavelength range down to the UV wavelengths. This positions ScAlN as a good candidate for UV applications and offers an additional benefit over other platforms such as $LiNbO_3$, which have longer cutoff wavelengths. When operating at a shorter wavelength, the device will be more sensitive to the scattering loss, as has been shown in AlN devices.[183] The scattering loss originates from the defects in the materials as well as the waveguide sidewall roughness. In the hybrid structure, since ScAlN remains un-etched, the sidewall scattering loss will be limited by the Si3N4 guiding layer, which shows ultra low roughness. Therefore, at shorter wavelengths, the hybrid structure is expected to be much less sensitive to the scattering loss induced by the sidewall roughness. The advantage will be clearer when extending to higher Sc compositions, where the etching would be more challenging, inducing worse waveguide profiles.

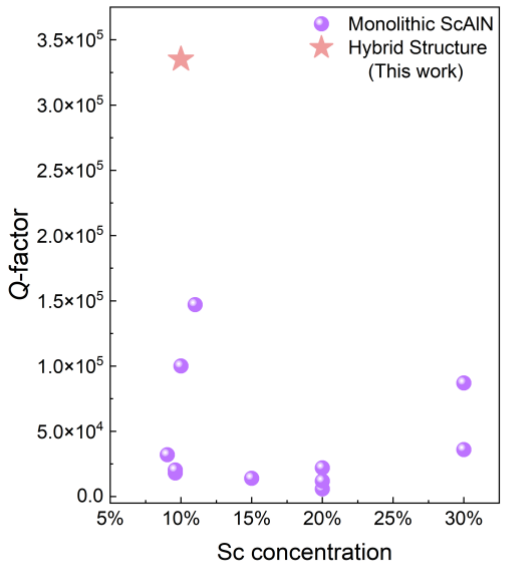


Figure 5.6: Benchmarking of intrinsic quality factors. Comparison of the intrinsic quality factor of the hybrid ScAlN/Si_3N_4 microring demonstrated in this work with other reported monolithic ScAlN resonators of various Sc compositions.

5.5 Conclusion

In summary, we experimentally demonstrate a monolithically integrated Si_3N_4–ScAlN photonic platform with an intrinsic quality factor of $Q_i = 3.35 \times 10^5$, corresponding to a low propagation loss of 1.03 dB/cm on par with hat of commercial single-mode SOI waveguides. The optical mode is confined within the etched Si_3N_4 layer, avoiding direct etching of the hard-to-process underlying ScAlN film. This monolithically integrated structure benefits from the mature, low-loss fabrication process of Si_3N_4 waveguides while leveraging the functional properties of the ScAlN layer. It is also worth noting that further reduction in optical loss is foreseeable as the current Si_3N_4 film's residual absorption due to hydrogen-related bonds (e.g., N–H, Si–H) can be mitigated through proper annealing or hydrogen-free deposition techniques toward even lower material absorption and improved waveguide performance.[184, 185] Our results highlight the potential of combining multiple functional materials and components on a single chip, enabling advanced photonic functionalities while remaining compatible with the well-established CMOS fabrication processes to pave the way for scalable, high-speed photonic systems tailored to future data communication, signal processing, and AI-driven big data center applications.

Chapter 6 Low Sheet Resistance ScAlN/GaN Heterostructures for High-performance Electronics

6.1 Introduction

When forming III-nitride-based heterostructures such as AlGaN/GaN, InAlN/GaN and AlN/GaN, the intrinsic spontaneous polarization and the piezoelectric polarization formed, as discussed in Chapter 1, will generate high density of two-dimensional electron gas (2DEG) with moderately high carrier mobility.[186, 187] The superior carrier transport properties of such structure have led to successful integration in the high electron mobility transistors (HEMTs).[4, 188, 189] Combined with the inherent wide bandgap properties of the III-nitride materials, HEMT devices demonstrate strong competence across a broad range of power electronics and radio frequency (RF) applications, ranging from renewable energy systems to 5G/6G communications.[190] One of the critical metrics affecting the HEMTs performance is the sheet carrier resistance (R_{sh}), which quantifies the resistance in the 2DEG layer. Reducing sheet resistance minimizes power loss and enhances device efficiency by increasing current density, improving gain, and extending operational frequency.[191] The sheet resistance is related to the sheet carrier concentration (n_s) and the carrier mobility (μ) by Eq. 6.1:

$$R_{\mathrm{sh}} = \frac{1}{e \cdot n_s \cdot \mu} \tag{6.1}$$

where e is the elementary charge with the value of 1.6×10^{-19} C. To achieve lower R_{sh} and consequently enhance device performance, higher sheet carrier concentrations and mobilities are favored.

The content of this chapter has been published on *Applied Physics Letters*. The work is supported by the Army Research Office under Grant No. W911NF2420210 and W911NF2220176, and by the College of Engineering at the University of Michigan.

The 2DEG density induced at the nitride interface can be expressed by Eq. 6.2 [192]:

$$n_s = \frac{\sigma_{pz}}{e} - \left(\frac{\varepsilon_B}{de^2}\right)\left(e\phi_b + E_f - \Delta E_c\right) \tag{6.2}$$

where σ_{pz} is the piezoelectric sheet charge density, ε_B represents the dielectric constant of the barrier, d is the thickness of the wider bandgap barrier, $e\phi_b$ is the Schottky barrier height, E_f is the Fermi level with respect to the GaN conduction band edge energy, and the ΔE_c is the conduction band offset between the barrier and GaN. From this equation, it suggests that increasing the barrier thickness and enlarging the conduction band offset could be beneficial to enhance the 2DEG carrier generation. Conventional GaN-based HEMTs are built upon the $Al_xGa_{1-x}N$ /GaN heterostructure, where the 2DEG density will grow with increased Al mol fraction and AlGaN barrier thickness and can reach 5×10^{13} cm^{-2}.[193, 194] For Al-rich AlGaN or even AlN, the large lattice mismatch between AlGaN and GaN indicates that the critical thickness of Al-rich AlGaN is thin and can easily induce defects during the pseudomorphic growth.[195] According to the equation above, the thinner barrier limited by the critical thickness will lead to the barrier thickness *d* to be small thus restrict the generated carrier density. Additionally, the large strain and the thinner barrier will pose challenges in device operation under extreme environment with low leakage current.[196] A more lattice-matched $In_xAl_{1-x}N$/GaN structure was then proposed to be integrated in the HEMT structure.[196-198] The much reduced lattice mismatch breaks the thickness limitation yet the induced 2DEG concentration is limited to be less than 3×10^{13} cm^{-2}.[199] Studies have shown that high mobility and high sheet carrier concentration can be achieved in the AlN/GaN heterostructure to support low sheet resistance below 200 Ω/□ yet it is difficult to further reduce the R_{sh} value due to the challenges inherent from the growth.[193, 194]

Scandium aluminum nitride ($Sc_xAl_{1-x}N$) has gained significant attention due to its greatly enhanced piezoelectricity compared to AlN as well as the emergence of ferroelectricity.[16, 22, 75, 169] Recent studies have also identified it as a promising material to be used as a barrier layer in the GaN HEMTs.[200-207] ScAlN has been predicted to have comparable, or larger spontaneous polarization than AlGaN and InAlN.[208, 209] More recent understandings of polarization in III-nitrides provides fundamental insights into polarization engineering, revealing additional benefits in ScAlN heterostructures.[69] Additionally, ScAlN with Sc less than 18% is

nearly lattice-matched to GaN, eliminating thickness limitation when forming heterostructures with GaN, similar to the InAlN/GaN structure yet with a significantly larger polarization difference due to the stronger spontaneous polarization of ScAlN.[32, 208, 210] With the lattice-matched characteristic, it is also expected that the growth of the ScAlN barrier layer will generate less defects and less roughness at the interface, reducing the scattering and thereby enhancing the carrier mobility at the 2DEG layer. Successful demonstrations of using ferroelectric materials such as ScAlN as the barrier in GaN HEMTs have shown excellent performance with large current density and good RF performance.[200-203, 205, 206, 211-214] The integration of ferroelectric ScAlN has further provided another way of advanced computing.[63, 200, 205, 206, 215, 216] A closer study into the band alignment of ScAlN/GaN reveals that the conduction band offset between ScAlN and GaN is more than 2 eV, which is even larger than the offset between AlN and GaN (~1.5 eV), suggesting that the ΔE_c term in the equation is also enlarged to support higher n_s.[64, 81, 217, 218] With the largely boosted carrier density, it provides a new pathway to further reduce the sheet resistance for operations at higher power and higher frequency with improved efficiency.

6.2 Heterostructure Growth and Characterizations

To investigate and understand the inherent contribution from the strong spontaneous polarization of AlScN without incurring the remnant polarization induced from the ferroelectric switching, the ScAlN/GaN-based HEMT structures were grown by plasma-assisted molecular beam epitaxy (PA-MBE) in a Veeco GENxplor system. The active nitrogen atoms were provided by the N_2 plasma source while the high purity metals of Al, Ga and Sc were evaporated from the effusion cells. To investigate the effect of ScAlN barrier thickness on the carrier transport properties, we grew a series of samples on the C-doped high-resistive GaN-on-sapphire substrate to reduce the parallel conduction effect from the bottom GaN. The sample structures are depicted in Fig. 6.1(a). After loading into the growth chamber, the sample surface was in-situ cleaned by Ga-assisted cleaning in a periodic Ga deposition and thermal evaporation fashion. The Ga adsorption and desorption processes can be observed by monitoring the intensity change of the reflection high-energy electron diffraction (RHEED) pattern where the intensity reduces while Ga is adsorbed on the surface and recovers during the Ga desorption stage. An unintentionally doped GaN was then grown in a slightly metal-rich condition at substrate temperature 580 ˚C as the buffer

layer to achieve a smooth surface. Additionally, a regrown GaN layer can provide a clean and sharp interface with the ScAlN/AlN barrier owing to the continuous growth in the ultra-high vacuum MBE chamber without introducing external impurities. The thin AlN interlayer (2 nm) inserted between the ScAlN barrier and the GaN channel will benefit to suppress the scattering causing from the alloy disorder as AlN is a binary material and increase the 2DEG density.[219-221] We then grew the $Sc_{0.15}Al_{0.85}N$ barrier with various thicknesses, ranging from no ScAlN barrier (0 nm) to 4 nm, 12 nm, 15 nm, and 24 nm thicknesses above the AlN spacer. The composition of ScAlN was calibrated by energy dispersive X-ray spectrometer (EDS) on a thick ScAlN-on-GaN sample grown at the same condition. Finally, 1.5 nm GaN was capped on top of the ScAlN/AlN barrier. ScAlN tends to be much easier oxidized compared to AlN and GaN and the GaN capping can serve as a protection to avoid the ScAlN barrier being oxidized, especially for the thinner ScAlN barrier structures.[81] In the meantime, the GaN capping suppresses the formation of surface states that would degrade the 2DEG density and the associated device performance.[222, 223]

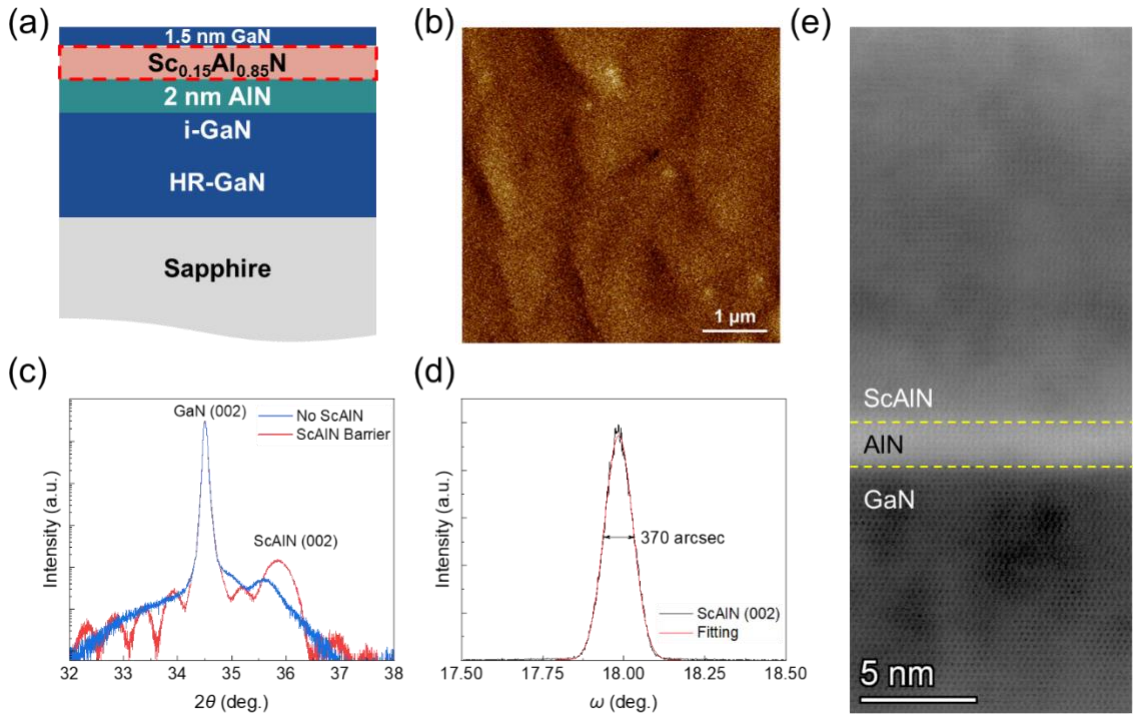


Figure 6.1: (a) Illustration of the grown GaN/ScAlN/AlN/GaN sample structure with varying $Sc_{0.15}Al_{0.85}N$ thicknesses of 0, 4, 12, 15 and 24 nm. (b) Atomic force microscopy image of the heterostructure with 24 nm ScAlN barrier showing rms roughness 1.4 nm. The height color bar is 6 nm. (c) X-Ray diffraction pattern of the 2θ–ω scan on the heterostructure showing (002) peaks of GaN substrate and the epitaxial ScAlN barrier. (d) The XRD rocking curve

scan on the ScAlN (002) peak with 370 arcsec linewidth. (e) Transmission electron microscope imaging on the all-epitaxial ScAlN barrier/AlN interlayer/GaN channel grown by MBE with atomically sharp and clear interface.

The lattice match characteristic between ScAlN and GaN provides a great path to reduce the defects associated with the strain and can overcome the critical thickness limitation as mentioned above. Figure 6.1(b) illustrates the atomic force microscopy (AFM) characterization of the growth stack with 24 nm $Sc_{0.15}Al_{0.85}N$ barrier. The surface root mean squared (rms) roughness is less than 1.5 nm with the atomic step appearing from the AFM scanning, indicating a smooth surface that would be critical in reducing surface states for high performance devices. Figure 6.1(c) depicts the high-resolution X-ray diffraction (HRXRD) pattern of the same sample with 2θ-ω scan. The spectrum shows the (002) peaks of GaN and the ScAlN barrier. It is also noted that interference fringes exist on the spectrum. These Pendellösung fringes originate from the GaN/ScAlN/AlN/GaN heterostructure with clean and smooth interfaces. The high-resolution transmission electron microscopy (HR-TEM) images taken at the stack further confirm the atomically sharp interface between each layer. These smooth and clear interfaces are instrumental to provide high 2DEG carrier densities with minimal scattering from roughness and impurities.[224]

6.3 Hall Measurement at Room Temperature

To study the 2DEG transport characteristics in the grown structures, we have performed Hall-effect measurements with van der Pauw configuration at room temperature for all five samples with different ScAlN barrier thicknesses. To exclude the contribution from the GaN, we grew the i-GaN layer on the semi-insulating GaN substrate at the same growth condition as we used for the following ScAlN/AlN/GaN heterostructures. No current and carrier density can be measured from this structure, confirming the carrier transport contribution is from the heterostructure only. For the structures without or with thinner ScAlN barrier, there is negligible changes on the carrier mobility with slightly increasement from 1139 to 1165 $cm^2/V{\cdot}s$ when the ScAlN barrier grows from 0 to 12 nm. However, the 2DEG carrier densities has a clear increasing trend. When there is no ScAlN barrier added, 1.1×10^{13} cm^{-2} sheet carrier concentration was measured. This is a moderately high density yet adding only a thin layer of 4 nm ScAlN can elevate the n_s to 3.6×10^{13} cm^{-2}, which is more than three times higher compared to that with the AlN-only barrier case. This enhancement can be attributed to both increased nitride barrier thickness

for the stronger spontaneous polarization as well as the larger conduction band offset between ScAlN and GaN compared to AlN and GaN.[81, 208, 209, 217] When the barrier thickness was increased to 12 nm, the carrier density can be further improved to 4.2 × 10^{13} cm^{-2}. The relatively constant mobility with increased 2DEG carriers suggests that the mobility of thinner barrier samples is not primarily dominated by the mechanism that has a strong dependence on the carrier density. Instead, it is believed that the mobility at room temperature is more associated with the coupling between electrons and the polar optical phonons.[225] With the notably increased 2DEG density and the relatively constant mobility, the sheet resistance got considerably reduced from 479 Ω/□ to 127 Ω/□. Further increasing the ScAlN barrier thickness to 15 nm and 19 nm raised the n_s value to 7.8 × 10^{13} cm^{-2} and 8.2 × 10^{13} cm^{-2}, respectively, which are record-high sheet carrier concentrations to our knowledge. However, the mobility also gets slightly reduced to 836 $cm^2/V{\cdot}s$ and 416 $cm^2/V{\cdot}s$ with such high electron density that brings the carrier scattering effect more prominent. Nevertheless, with the much-improved 2DEG density, the sheet resistance can be reduced to 95.5 Ω/□, which is a record low R_{sh} in single channel GaN HEMT structures to our best knowledge. We further grew a thicker ScAlN barrier with a thickness of 24 nm and found that the sheet concentration was reduced to 6 × 10^{13} cm^{-2} and R_{sh} was increased to 111.7 Ω/□. In a separate batch of samples, we further varied the thicknesses of ScAlN barrier to 8 nm and 19 nm and measured consistently high 2DEG density, shown as the open circles in Figure 6.2(b). In this batch of samples, however, we had to significantly reduce the Al flux during the thin AlN barrier growth due to MBE system limitations, which resulted in AlN interface roughness and reduced carrier mobility (not shown).

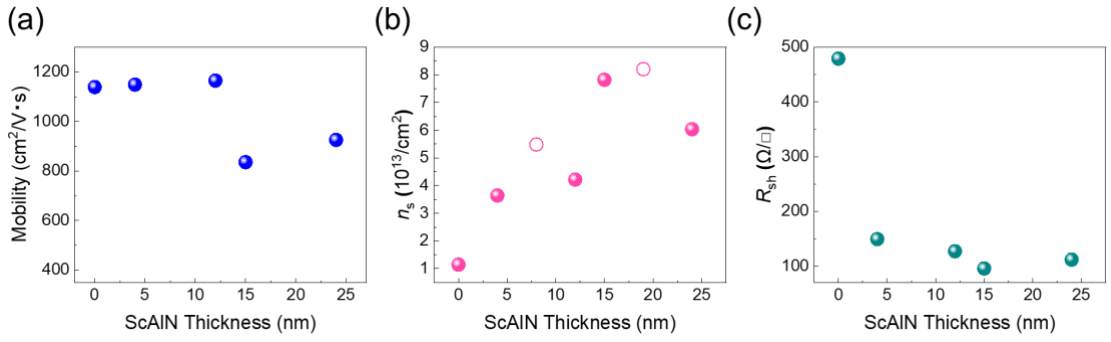


Figure 6.2: The Hall measurement with van der Pauw configuration on epitaxial GaN/ScAlN/AlN/GaN HEMT samples. (a) Electron carrier mobility. (b) 2DEG sheet carrier density. (c) Sheet resistance of different ScAlN barrier thicknesses. Open circles in (b) represents a separate batch of samples with varying ScAlN barrier thicknesses.

6.4 Temperature-dependent Hall Measurement

Further investigation on the low sheet resistance samples was done by measuring the temperature-dependent Hall effect with the physical property measurement system (PPMS) that goes to 10 K. The samples are fabricated into van der Pauw geometry with Ti/Au metal contacts. Results are shown in Figure 6.3, where both the mobility μ and the sheet carrier concentration N_s feature monotonic change with temperature. Due to the stronger relative movement between neighboring atoms at higher temperatures, the polar optical phonon scattering will limit the mobility within this temperature regime. As the temperature was reduced below 100 K, the mobility did not increase drastically, with μ_{70K} = 3480.9 cm^2/V·s and μ_{10K} = 4223.5 cm^2/V·s. The dominant mechanism limiting the mobility at the lower temperature regime can be attributed to scattering from impurities and the interface roughness.[224] Figure 6.3(b) shows the sheet carrier concentration n_s dependence on temperature, and it decreased from more than 7 × 10^{13} cm^{-2} near room temperature to around 4.5 × 10^{13} cm^{-2} below 100 K. Previous studies suggested that the temperature dependence of carrier density indicated that the parallel conduction in the GaN buffer could be freeze out at a lower temperature, similar to the cases that have been reported in several AlGaN/GaN heterostructures.[226, 227] However, as described above, the carrier concentration for the control samples showed negligible contribution from the GaN buffer layer. Moreover, the sample with only a thin AlN barrier layer further sets the upper limit for the parallel conduction in the GaN buffer layer to be less than 1 × 10^{13} cm^{-2} at room temperature, shown in Figure 6.2(b). On the other hand, the strong piezoelectricity of ScAlN and its temperature dependence may largely account for the variation of 2DEG with temperature. Although the carrier density got reduced at lower temperature, with the much-improved mobility, we can still achieve a lower sheet resistance R_{sh} value of 33.3 Ω/□ at 10 K and 38.6 Ω/□ at 70 K. Such low resistance demonstrates the superior 2DEG transport properties in the GaN HEMT with ScAlN barrier.

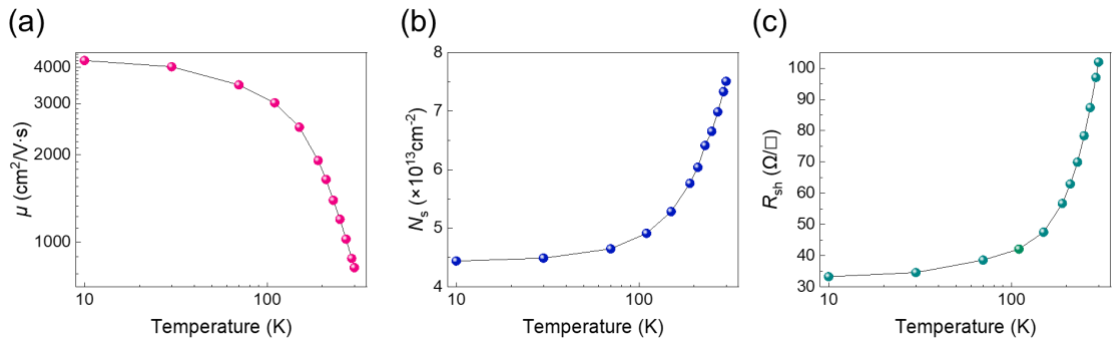


Figure 6.3:The temperature-dependent Hall measurement with Ti/Au contact on the HEMT structure with 15 nm $Sc_{0.15}Al_{0.85}N$ barrier. (a) Electron mobility. (b) 2DEG sheet carrier density. (c) Sheet resistance in the temperature range of 10 K to 300 K.

6.5 Band Diagram Simulations

By solving the Schrödinger and Poisson equations self-consistently, the band diagram of the GaN/ScAlN/AlN/GaN heterostructures with different ScAlN thickness are plotted in Figure 6.4(a). By integrating the electron distribution, the sheet carrier concentration was extracted and plotted in Figure 6.4(b). With the ScAlN layer thickness increased, stronger spontaneous polarization is provided in the barrier layer, which leads to a higher density of 2DEG formed at the ScAlN/AlN/GaN interface. From the figure, it is also shown that by adding the thin AlN interlayer, the 2DEG can be well confined in the well. Figure 6.4(b) plots the calculated sheet carrier density with varying ScAlN barrier thicknesses and it follows the trend of AlGaN/GaN heterostructure that the induced carriers get monotonically increased with thicker barrier layer thickness until it saturates at more than 7×10^{13} cm^{-2} when the ScAlN barrier is more than 20 nm thick. The calculated results are in good agreement with the experimental data with the small deviations possibly originating from the growth variations for different samples.

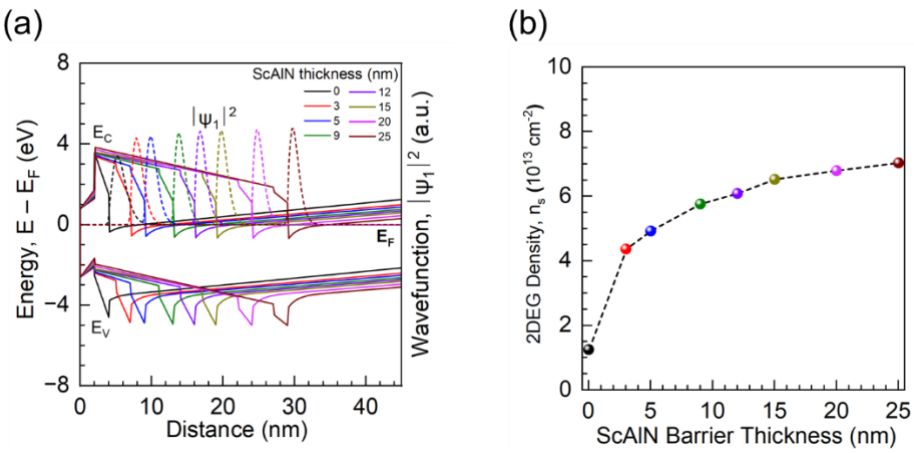


Figure 6.4: Calculation results by solving Schrödinger and Poisson equations self-consistently. (a) Band diagram of the GaN/ScAlN/AlN/GaN with the electron wavefunction plotted within the well. (b) Extracted 2DEG carrier density by integrating the carrier distribution, showing the 2DEG density can reach more than 7×10^{13} cm^{-2} when ScAlN barrier is thick enough.

6.6 Conclusion

Figure 6.5 summarizes and compares the carrier transport properties of our ScAlN/AlN/GaN heterostructures measured at room temperature with some other ScAlN/GaN-based structures reported in the literature.[204, 206, 207, 219, 220, 228-234] It is shown that incorporating ScAlN as the barrier layer in the HEMT structure in general has the capability to induce a large sheet carrier concentration compared to AlGaN/GaN and InAlN/GaN. In this work, by varying the nearly lattice-matched ScAlN barrier thickness, we have further boosted the 2DEG sheet carrier concentration to a level close to 8×10^{13} cm^{-2}, which push the sheet resistance to an ultralow value of 95.5 Ω/□.

In summary, we have demonstrated an epitaxial ScAlN/AlN/GaN heterostructure with the sheet resistance below 100 Ω/□ at room temperature, which is attributed to the record-high carrier concentration of 7.8×10^{13} cm^{-2} induced by the ultrawide bandgap ScAlN barrier. Moreover, the sheet resistance remains constantly below 200 Ω/□ across varying ScAlN barrier thicknesses ranging from 4 nm to 24 nm, further demonstrating the robust low R_{sh} characteristics. By evaluating the 2DEG properties under temperature dependent Hall measurement down to 10 K, it reveals the mobility can be boosted to 4223.5 cm^2/V·s and R_{sh} further reduced to 33.3 Ω/□. The precise control over the growth parameters of composition, thickness and growth rate of each layer in the heterostructure enabled by MBE, coupled with the strong and tunable polarization in $Sc_xAl_{1-x}N$ barrier provides a promising pathway to tailor the desired device parameters such as

2DEG carrier concentrations in the HEMT structures. The compelling 2DEG transport properties of the ScAlN barrier HEMT can lead to improved power electronics and RF devices performance.

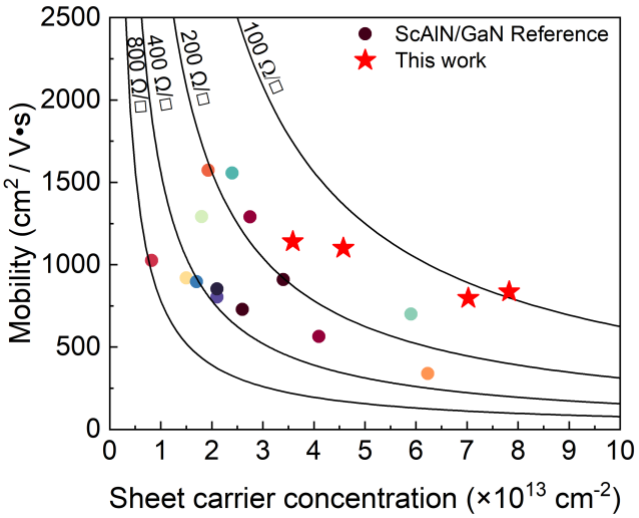


Figure 6.5: Benchmark of sheet carrier concentration n_s and electron mobility of this work with other reported ScAlN/GaN heterostructure data with sheet resistance contour line labeled.

Chapter 7 High-temperature Stable ScAlN/GaN High-Electron Mobility Transistors

7.1 Introduction

High-temperature electronics are widely used in aerospace exploration (~500°C), hypersonic vehicles (~1700°C), electric vehicles (~850°C), gas turbines (~500°C), and energy-dense systems.[235-239] Extensive research has been conducted on wide-bandgap materials because of the challenges traditional electronics suffer when exposed to high-temperature environments, such as increased leakage current and poor stability.[240-242] Due to its several advantages, GaN has shown great potential among wide-bandgap materials for such applications. These include its large bandgap, high-breakdown field, exceptional thermal stability, and high-saturation velocity.[243, 244] Although temperature-dependent studies have been conducted on AlGaN/GaN HEMTs in the last few decades,[196, 245-249] a significant reduction in drain current is observed for an $Al_{0.25}Ga_{0.75}N$ barrier layer even at 300°C. For example, a ~65% reduction was reported by Hatano et al.[249] Recently, Islam *et al.* reported that the $Al_{0.28}Ga_{0.72}N$/GaN HEMT with T-gate had a reduction in drain current capacity of 43% and 65%, respectively, at 300°C and 500°C.[245] To improve the thermal stability of GaN HEMTs, devices made with a lattice-matched InAlN barrier were reported.[196, 246] Due to less residual strain, InAlN/GaN HEMTs demonstrated better stability up to 1000°C.

The integration of ferroelectric nitrides with GaN HEMTs has become more attractive with the recent demonstration ferroelectric switching in single crystalline ScAlN, ScGaN, ScAlGaN, and YAlN on various substrates.[59, 68, 72, 75, 168, 250, 251] Scandium (Sc)-alloyed AlN (ScAlN) which can be lattice-matched to GaN, has emerged as a suitable choice as a barrier material for GaN HEMTs due to its ferroelectricity and large polarization.[200, 201, 206, 220] Using ScAlN/GaN heterostructure, Hardy *et al.* obtained a high charge density of 3.14×10^{13} cm^{-2} and Hall mobility of 910 $cm^2/V\cdot s$ at room temperature (RT).[220] ScAlN/GaN HEMTs have been

The content of this chapter has been published on *Applied Physics Letters*. The work is supported by the Army Research Office under Grant No. W911NF2420210, and by the College of Engineering at the University of Michigan.

reported with very high drain currents due to substantial differences in polarization between GaN and the epitaxial ScAlN layers.[200, 201] In 2021, an in situ structural and dielectric study conducted by Islam *et al.* revealed that ScAlN material exhibited exceptional temperature stability up to 1100 °C.[252] Wang *et al.* demonstrated that ScAlN/GaN-based memristors upheld a rectifying ratio above 10 even at 400 °C.[65] However, no experimental evidence has been identified to date concerning the effect of temperature on the performance of ScAlN/GaN HEMTs.

In this work, we demonstrated high-temperature operation of $Sc_{0.15}Al_{0.85}N$/GaN HEMT up to 700 K. At RT, the maximum drain current density, I_{Dmax} and on-resistance, R_{on} were found to be ~2.17 A/mm and ~1.48 Ω·mm, respectively. A ~52% of reduction in drain current was observed for the ScAlN/GaN HEMT, which is comparatively lower to the conventional AlGaN/GaN HEMTs. Moreover, the ScAlN/GaN HEMT showed the maximum drain current density above 1 A/mm at 700 K, which is over two times higher than any other reports on AlGaN/GaN HEMTs.[245]

7.2 High Current ScAlN/GaN HEMTs Fabrication

Figure 7.1 (a) shows the schematic illustration of $Sc_{0.15}Al_{0.85}N$/GaN HEMT which is fabricated on a semi-insulating GaN (~2 µm)/sapphire substrate. Epi-layers were grown by molecular-beam epitaxy (MBE). The structure consists of a 120 nm thick unintentional doped (UID) GaN channel, 9 nm $Sc_{0.15}Al_{0.85}N$ barrier layer and 2 nm GaN cap layer. A 2 nm AlN was also grown underneath the $Sc_{0.15}Al_{0.85}N$ barrier layer for confining the two-dimensional electron gas (2DEG). Hall-effect measurements in the standard van-der Pauw configuration presented a 2DEG density of 6×10^{13} cm^{-2} and an electron mobility of 710 $cm^2/V\cdot s$ at RT. The device fabrication process flow of HEMTs with regrown contacts is shown in Fig. 7-1 (b). To make ohmic contacts to the 2DEG, a SiO_2 hard mask was first used to define the source and drain regions. This was followed by dry etching and subsequent selective area regrowth of heavily Si-doped n^+-GaN (with a donor concentration of approximately $N_d \sim 10^{20}$ cm^{-3}) at the source and drain regions using MBE. Ti/Al/Ni/Au (25/100/15/10 nm) source/drain metal stacks were deposited on the regrown n^+-GaN, and Ni/Au (20/200 nm) metals were deposited for Schottky gate metallization. Prior to the gate metal deposition, the ohmic metal stacks were annealed at 850 ºC for 30 s in N_2 environment using a rapid thermal annealing (RTA) system. The transfer length method (TLM) measurement curves are shown in Figs.7-1 (c) and (d). The sheet and contact resistances and the transfer length were measured to be 184 Ω/□, 0.18 Ω·mm, and 0.9 µm, respectively. This gives an ohmic specific

contact resistivity of 1.72×10^{-6} Ω·cm^{-2}. We also measured the TLM curves on the regrowth n^{+}-GaN area only and derived the contact and sheet resistances of 0.05 Ω·mm and 33 Ω/□, respectively. These results were in good agreement with those previously reported in literature for regrown contacts.[253, 254] The gate length (L_G), gate-to-source distance (L_{GS}), gate-to-drain distance (L_{GD}), and gate width (W_G) were fixed at 1, 2, 2, and 10 µm, respectively. We used an MMR variable-temperature micro probe (VTMP) system with a Joule-Thomson thermal stage to measure our device. Using an MMR K2000 digital-temperature controller with a vacuum pressure of 4 mTorr, stage temperatures were varied from RT to 700 K. DC characteristics were measured by a Keysight B1500A semiconductor parameter analyzer.

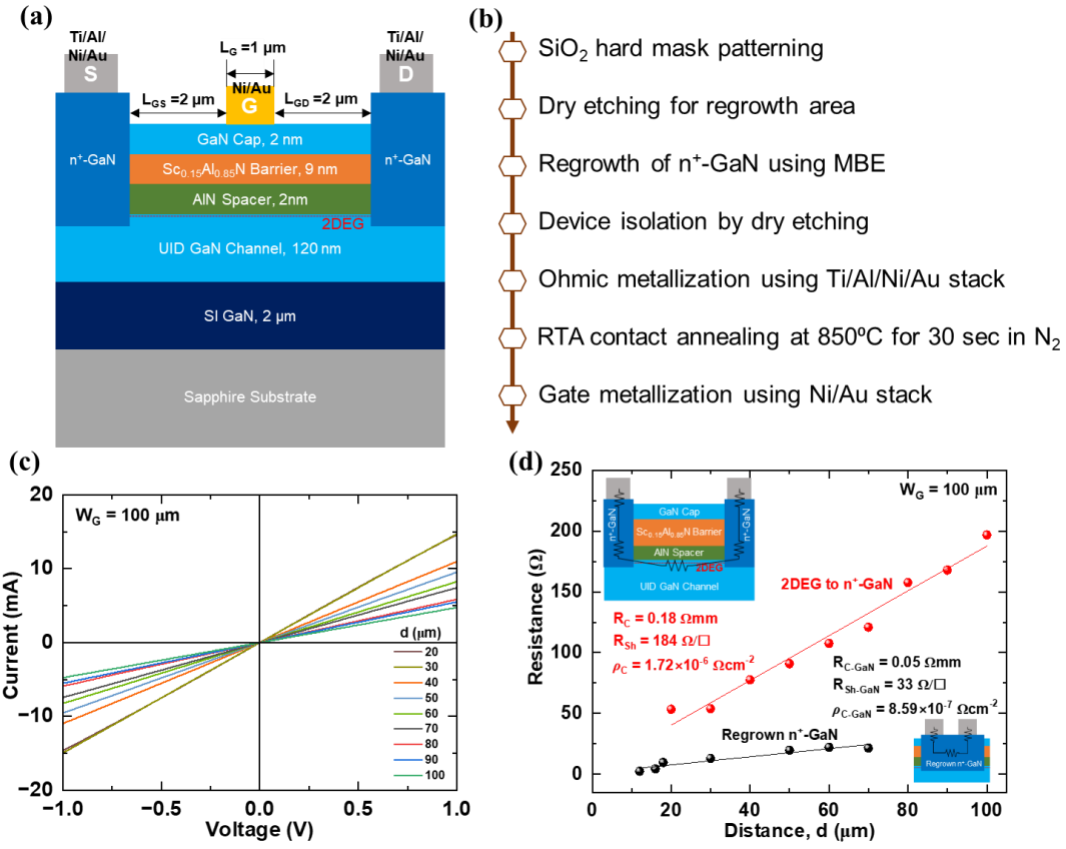


Figure 7.1: (a) Schematic illustration of ScAlN/GaN HEMT. (b) The fabrication process flow. (c) Current-voltage characteristics of different distances on TLM pattern. (d) Resistance versus distance curves at RT.

7.3 Temperature-Dependent Device Characterizations

Figure 7.2 shows the static characteristics of our fabricated ScAlN/GaN HEMTs at RT and 700 K. The drain voltage (V_{DS}) was varied from 0 to 6 V with different gate-voltages (V_{GS}) for output characteristic curves (Figures 7.2 (a) and (b)), and V_{GS} was varied from +1 V (on-state) to

−20 V (off-state) to +1 V (on-state) with a fixed V_{DS} of 5 V for transfer curves (Figures 7.2 (c) and (d)). The maximum drain current, I_{Dmax} defined at V_{GS} = 1 V was ~ 2.17 A/mm with an on-resistance, R_{on} value of ~1.48 Ω·mm at RT. An exceptionally high value of current was measured for an $Sc_{0.15}Al_{0.85}N$/GaN HEMT with an L_G of 1 μm. This is due to high-2DEG density induced by the large difference in polarization between the GaN channel and the epitaxial $Sc_{0.15}Al_{0.85}N$ barrier. These drain current and on-resistance results are also in good agreement with the reported literatures.[200, 201] On the other hand, I_{Dmax} of ~1.04 A/mm and R_{on} of ~4.17 Ω·mm were measured at 700 K. The device's current carrying capacity was reduced by ~52% and R_{on} was increased by 2.83 times compared to its RT value. A comparatively high gate leakage current densities of ~10^{-4} and ~10^{-2} A/mm were observed during off-state at RT and 700 K, respectively, shown in Figure 7.2 (c). At high temperatures, Poole-Frenkel emission becomes more significant and dominate to elevate the gate leakage current.[91] The I_{on}/I_{off} ratios were measured ~10^5 and ~10^3 measured at RT and 700 K, respectively, which are limited by the gate leakage. To suppress the gate leakage current under high temperature, inserting an additional insulating layer to form MIS-HEMT would be viable solution for the future devices.[255, 256] Additionally, after completing measurements of the device's input and output characteristics at 700 K, the stage temperature was cooled down from 700 K to RT and the device was re-measured. The device's performance remained nearly the same as in its virgin condition, indicating good thermal stability. Additionally, a very small hysteresis loop was observed in the gate-leakage current as well as the drain current at RT. This result indicates that electrons may have been trapped during off-stage due to a high gate leakage current at RT. The peak transconductance, g_{mpeak} was measured to be ~325 mS/mm and ~170 mS/mm at RT and 700 K with a fixed V_{DS} = 5 V, respectively, shown in Figure 7.2 (d). The results above indicate that ScAlN/GaN HEMTs are suitable for RF and high-power applications.

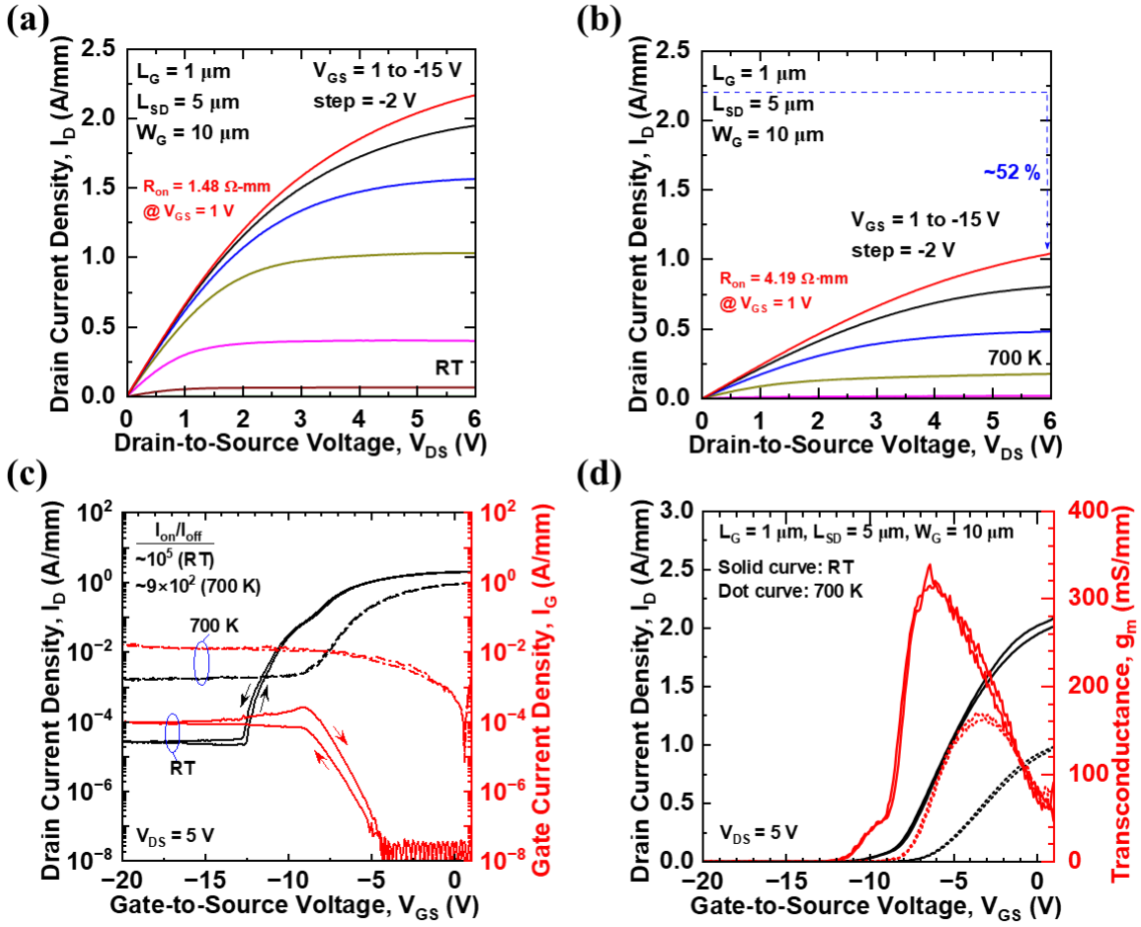


Figure 7.2: Drain current density, I_D versus drain-to-source voltage, V_{DS} characteristic curves of a device were measured by varying gate-to-source voltages, V_{GS} from -15 V (off-state) to 1 V (on-state) in -2 V increments at (a) RT and (b) 700 K. The on-resistances, R_{on} of 1.48 Ω·mm and 4.17 Ω·mm were measured at V_{GS} = 1 V for device tested at RT and 700 K, respectively. (c) Transfer curve in log-scale (black curve) and gate-leakage current (red curve) were measured at a fixed V_{DS} = 5 V. (d) Transfer (in linear scale, black curve) and transconductance, g_m characteristic curves (red curve) measured at RT and 700 K.

Figure 7.3 (a) shows the benchmarking of temperature-dependent normalized drain current with those of published and commercially available wide-bandgap transistors.[239, 245, 248, 249, 255, 257-259] The maximum saturation drain currents as a function of temperature were normalized by its value at RT. Our proposed device exhibits less current degradation compared to other GaN-based HEMTs with AlGaN barrier. Notably, a significant factor in the drain current degradation with temperature is the relative contribution of the contact resistance and channel resistance towards the R_{on}. In this study, the R_{on} was determined to be ~1.48 Ω·mm with a total contact resistance of 0.36 Ω·mm, leading to an estimated channel resistance of ~1.12 Ω·mm, which represents 76% of the R_{on} at RT. Therefore, scaling the channel length would be the next strategy

to further reduce temperature-dependent device degradation.[259] We also showed the benchmarking of the saturation drain current density for the higher temperatures, ranging from 573 to 700 K with published results, shown in Figure 7.3 (b). Our device exhibited a very high I_D of ~1.04 A/mm even at 700 K. These results indicate that ScAlN/GaN HEMTs will enable high-power devices to operate even in harsh environments.

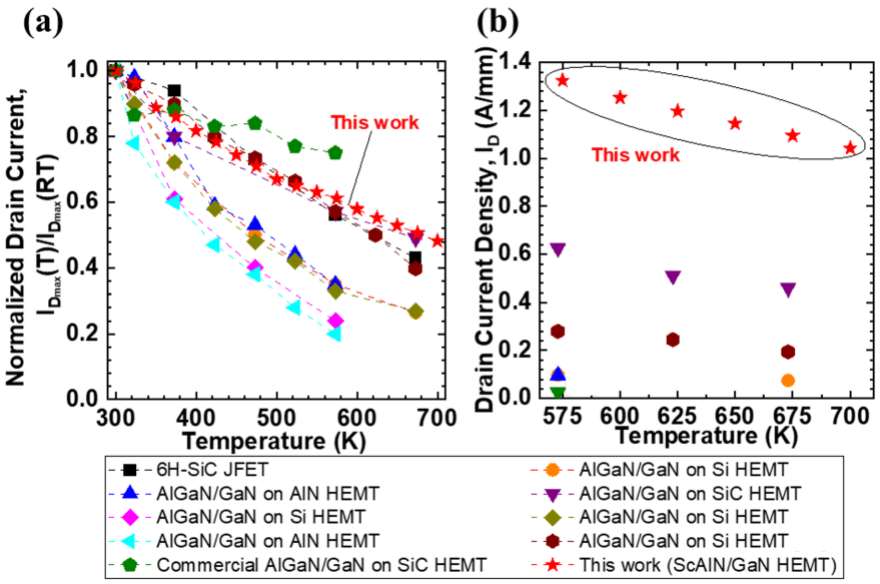


Figure 7.3: (a) Benchmarking of temperature-dependent normalized drain current of our proposed device with those published and commercially available wide-bandgap transistors. (b) Benchmarking of saturation drain current density as a function of temperature range 573 to 700 K.

The g_{mpeak} is also shown as a function of temperatures in Figure 7.4 (a). It was reduced by ~50% at 700 K compared to its value at RT. To clarify the degradation of drain current as well as the g_{mpeak}, we measured the temperature-dependent R_{on} as shown in Figure 7.4 (a). It was measured in the linear range, i.e., below 1/5 of the I_{Dmax}. The value of R_{on} increased by ~2.8 times with the increase in temperature from RT to 700 K. More recently, Niroula et al. reported that, the regrown contact resistance, R_C was very stable at high temperature (~500 ºC), while sheet resistance, R_{Sh} increased monotonically.[260] Based on these findings, the increase in R_{Sh} appears to be most responsible for the observed increase in R_{on} in GaN-HEMTs. Additionally, we measured the temperature dependence of the 2DEG density and mobility using Hall measurements up to 500 K, shown in Figure 7.4 (b). The 2DEG density was almost constant, whereas 2DEG mobility exponentially decreased with increase in temperature. This results in an increase in the extracted R_{Sh} with temperature. These are in good agreement with those reported in the literature.[245] The

results above show that the resistance increases due to a decrease in mobility. The decrease in mobility being due to polar optical phonon (POP) scattering, similar results are shown in Ref. [261]. This POP scattering is most responsible parameter to increase the R_{Sh} with temperature as well as R_{on}.

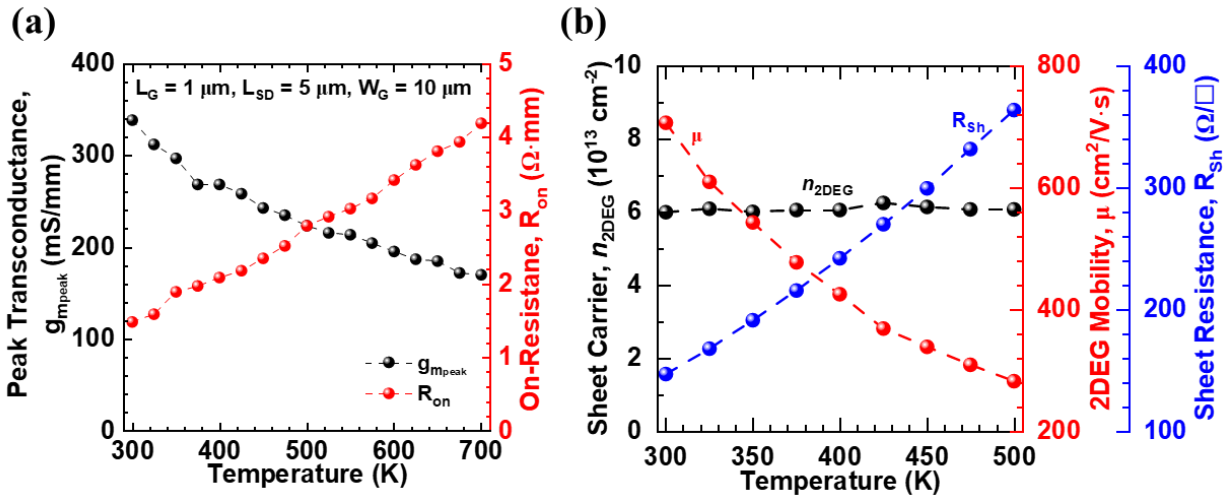


Figure 7.4: (a) Variations in g_{mpeak} and R_{on} with temperature. (b) Variations in sheet carrier, n_{2DEG}, 2DEG mobility, µ and sheet resistance, R_{Sh} with temperature measured using the van der Pauw method.

7.4 Conclusion

We studied the effect of temperature on ScAlN/GaN HEMT performance. A high drain current density of ~2 A/mm and an on/off ratio of ~10^5 were measured at RT. The R_{on} of ~1.5 Ω·mm was measured at V_{GS} = 1. A ~52% reduction of drain current and 2.82 times enhancement of R_{on} were observed when the device was tested from RT to 700 K. The reduction of 2DEG mobility, which leads to increased sheet resistance, is primarily responsible for this drain current reduction. These findings show that ScAlN/GaN HEMTs will be beneficial for high-power devices operating in harsh environments.

Chapter 8 High-Temperature Memory Devices Based on Ferroelectric ScAlN/AlGaN/GaN HEMTs

8.1 Introduction

The era of big data and the rapid advancement of artificial intelligence have intensified the demand for efficient computing systems capable of handling, processing, and storing vast volumes of data.[262, 263] Traditional von Neumann architecture faces challenges due to the so-called "memory wall," a bottleneck arising from the inefficiency of transferring data between memory and processing units.[262-264] To overcome this limitation, various emerging non-volatile memory (NVM) devices such as resistive random-access memory (RRAM), phase-change RAM (PCRAM), magnetoresistive RAM (MRAM), and ferroelectric (FE) memory have been proposed and studied alongside alternative computing paradigms, including near- or in-memory computing and biomimetic neuromorphic computing.[262-264] Among these candidates, ferroelectric field-effect transistors (FeFETs) have attracted attention due to their non-destructive read-out capability, multi-bit storage potential, energy efficiency, and ability to integrate logic and memory functionalities within a single device.[262, 264] By incorporating a ferroelectric layer into the gate dielectric stack of a transistor, data can be stored in the direction of the ferroelectric polarization.[250, 262, 264] This strategy holds the potential to affect computing by reducing latency, enhancing energy efficiency, and enabling new paradigms for data-intensive applications.[250, 262-264]

The discovery of ferroelectricity in HfO_2 in 2011 has catalyzed research on FeFETs.[265] As an already well-established high-*k* dielectric in modern logic transistors, HfO_2 provides excellent CMOS compatibility, positioning it as a promising candidate for high-volume manufacturing.[250, 265] This combination of properties has elevated FeFETs to the forefront as a transformative technology for next-generation computing systems.[262] Despite their promise,

The content of this chapter has been published on *Device*. The work is supported by the Army Research Office under Grant No. W911NF2420210, and by the College of Engineering at the University of Michigan.

current FeFETs based on ferroelectric HfO_2 and silicon or oxide channels struggle to meet the requirements for operation in harsh environments.[39, 264] This challenge arises from the instability of both the ferroelectric HfO_2 dielectric and the channel materials. Ferroelectric HfO_2 tends to degrade in performance at elevated temperatures, as its ferroelectric orthorhombic phase is metastable.[266] Above its Curie temperature of 500 °C,[250] ferroelectric properties of HfO_2 can diminish or vanish due to phase transformations, as well as the redistribution and generation of oxygen vacancies.[266, 267] Additionally, traditional semiconductors such as silicon and oxide-based materials are susceptible to degradation in extreme environments, including high temperatures, radiation, and chemical corrosion.[39] Consequently, current FeFETs exhibit limited operational temperature ranges, with the majority of studies conducted at room temperature.[39] This limitation underscores the need for material systems and device architectures to extend the applicability of FeFETs to demanding environmental conditions.

Scandium aluminum nitride (ScAlN), a wurtzite-structured ferroelectric material,[21] has emerged as a promising candidate for resilient electronics. ScAlN demonstrates high thermal stability, with a ferroelectric-to-paraelectric transition temperature exceeding 1100 °C,[252] attributed to its thermally stable wurtzite structure. Ferroelectric ScAlN diodes based on Ni/AlScN/Pt structures have shown operational temperatures up to 600 °C.[268] However, the diode structure lacks gain, modulation capability, and efficient switching control, which may limit its practical applications. Ferroelectric ScAlN-based field-effect transistors (FETs) with 2D and oxide semiconductor channels have also been demonstrated.[269, 270] Nevertheless, the vulnerability of 2D materials and oxide semiconductors to degradation under harsh conditions renders them unsuitable for extreme-environmental applications.[39]

In contrast, ScAlN benefits from compatibility with GaN platforms, which are renowned for their robustness and performance in high-power, high-frequency, high-temperature, and radiation-hard electronics.[271] By integrating ferroelectric ScAlN with AlGaN/GaN heterostructures, it is possible to develop ferroelectric high-electron-mobility transistors (HEMTs) that address the demands of harsh-environment applications and provides superior logic-memory performance. While some preliminary results on ferroelectric ScAlN/GaN HEMTs have been reported,[200, 206, 272, 273] their memory performance, particularly under high-temperature conditions, has yet to be demonstrated.

In this work, we report the development of ferroelectric ScAlN/AlGaN/GaN HEMTs enabled by molecular beam epitaxy (MBE). These devices demonstrate logic-memory functionalities, including an on-off current ratio exceeding 10^8, a subthreshold swing below 60 mV/decade across two decades of current, a memory window of approximately 4 V, an on-current of 474 mA/mm, and a transconductance of 140 mS/mm. These results are favorable when compared to previously reported ferroelectric GaN HEMTs,[200, 206, 272-277] ScAlN-based GaN HEMTs,[201, 202, 204, 228, 278, 279] and oxide-based FeFETs, [280-296] highlighting their competitiveness in logic-memory applications. Furthermore, the devices also exhibit reliable endurance, maintaining performance over 300 direct-current (DC) switching cycles, and stable retention performance extrapolated to over 10 years. They also showcase multi-bit capability at room temperature. The devices retain stable performance at elevated temperatures, with reliable operation at 250 °C and functionality up to 350 °C, highlighting their potential for high-temperature applications.

8.2 Fabrication of Ferroelectric ScAlN/AlGaN/GaN HEMTs

Figure 8.1(a) illustrates the schematic of the ferroelectric ScAlN/AlGaN/GaN HEMTs. The epitaxial layers were designed with a 120-nm unintentionally doped (UID) GaN channel layer, an 8-nm $Al_{0.3}Ga_{0.7}N$ barrier layer, and a 24-nm $Sc_{0.3}Al_{0.7}N$ ferroelectric layer on a semi-insulating GaN (~2 μm)/sapphire substrate. These layers were grown epitaxially using a Veeco GENxplor MBE system. Hall-effect measurements revealed a sheet carrier concentration of ~8×10^{12} cm^{-2} and a mobility of ~1000 $cm^2/(V\cdot s)$. The ScAlN layer exhibited an average remnant polarization of ~150 μC/cm^2, as determined in our previous work using positive-up-negative-down (PUND) measurements.[206] Device fabrication then begins by defining the source/drain regrowth regions, where a 300 nm SiO_2 layer was deposited using plasma-enhanced chemical vapor deposition (PECVD) and patterned through standard photolithography. This SiO_2 layer served as a hard mask during Cl-based inductively coupled plasma (ICP) etching to selectively remove the ScAlN and AlGaN layers in the contact areas. After etching, the samples were reintroduced into the MBE chamber for selective-area regrowth of 150 nm heavily doped n^+-GaN, with a Si doping concentration of approximately 10^{20} cm^{-3}. The SiO_2 hard mask was subsequently removed using a hydrofluoric acid (HF) solution. A metal stack of Ti/Al/Ni/Au (25/100/15/100 nm) was then deposited onto the regrown n^+-GaN regions by e-beam evaporation, followed by a lift-off process to form the source/drain Ohmic contacts. Transmission line measurements (TLM) indicated a low

contact resistance of ~0.05 Ω·mm between the source/drain metal and n^+-GaN, facilitating a high on-current (I_{on}). Mesa isolation of the active device region was defined by using SPR220 photoresist as a mask during Cl-based ICP etching. The photoresist was subsequently removed by immersion in PG Remover, followed by a water bath at 80 °C for 1 hour. Finally, a Schottky gate was patterned via photolithography and formed using a Ni/Au (20/200 nm) stack deposited by e-beam evaporation. Figure 8.1(b) presents a false-color tilted scanning electron microscope (SEM) image of the fabricated ScAlN/AlGaN/GaN HEMT, showcasing the GaN regrowth contact, mesa isolation, and source/drain/gate metallization. The fabricated devices feature a channel width (W_G) of 10 µm, a gate length (L_G) of 1 µm, a gate-to-source distance (L_{GS}) of 2 µm, and a gate-to-drain distance (L_{GD}) of 5 µm.

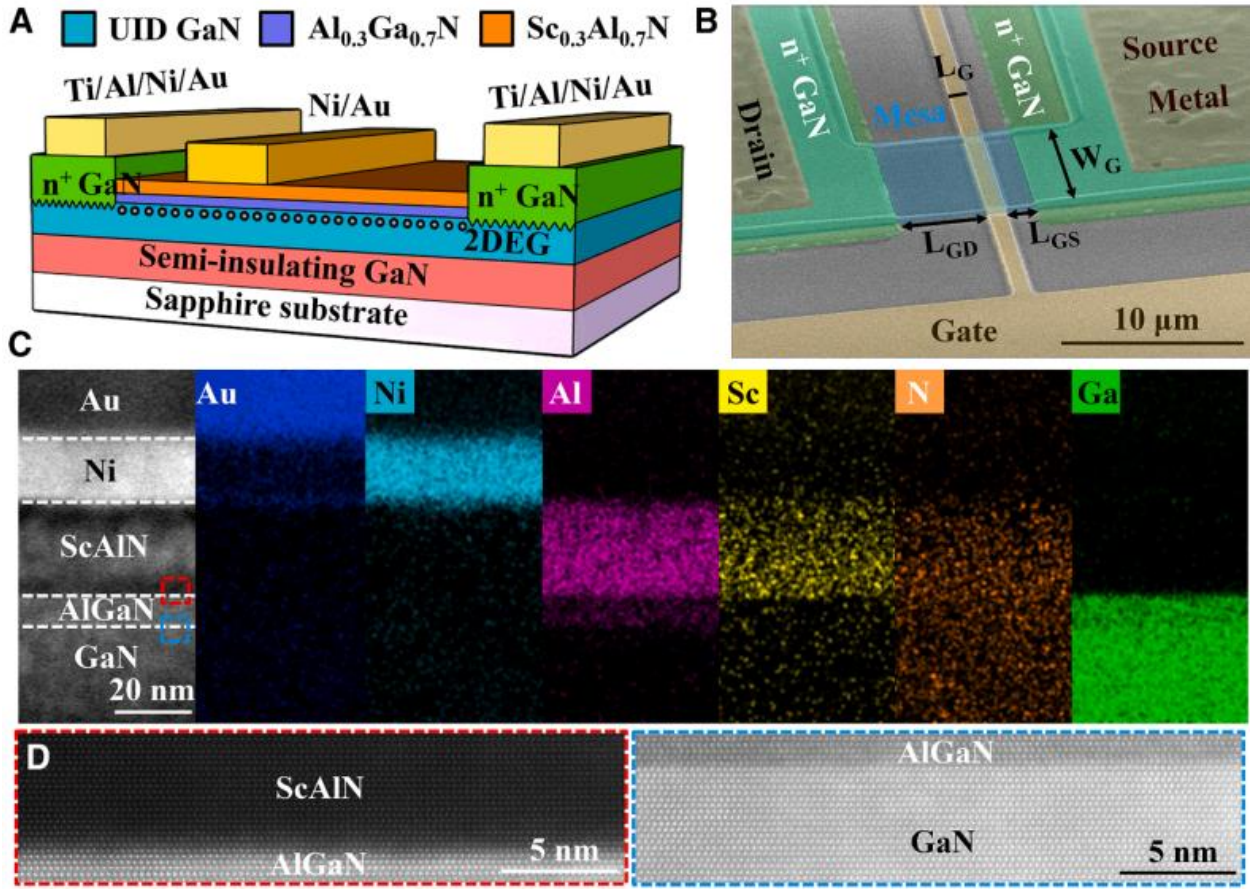


Figure 8.1: Illustration of ferroelectric ScAlN/ AlGaN/GaN HEMTs (a) Schematic of the ferroelectric ScAlN/AlGaN/ GaN HEMT. (b) False-color tilted SEM image of the fabricated ScAlN/AlGaN/GaN HEMTs, showing GaN regrowth contacts and a gate length (L_G) of 1 µm. (c) Cross-sectional HAADF image and corresponding EDS element maps of the Au/Ni/ScAlN/ AlGaN/GaN gate stack after high-temperature operation at 350 °C, revealing the thickness of each layer and uniform element distribution. (d) High-resolution HAADF-STEM images of the ScAlN/AlGaN and AlGaN/GaN interfaces after operation at 350 °C, revealing well-defined, high quality interfaces with atomic-scale resolution.

The structural and compositional integrity of the gate stack region in ScAlN/AlGaN/GaN HEMTs was examined after thermal exposure at 350 °C for approximately 2 hours. High-angle annular dark-field (HAADF) imaging was performed in conjunction with element mapping using X-ray signals, providing simultaneous insights into the structural and compositional characteristics. Figure 8.1(c) shows the HAADF image of Au/Ni/ScAlN/AlGaN/GaN gate stack along with the corresponding element maps, which confirms the thickness of each layer. The interfaces within the gate stack are abrupt and clean, with a uniform elemental distribution, indicating that high-quality interfaces can be maintained after high-temperature operation. High-resolution HAADF-STEM imaging was further employed to examine the ScAlN/AlGaN and AlGaN/GaN interfaces post-thermal exposure, as shown in Fig. 8.1(d). These images reveal atomically sharp and well-defined interfaces, along with the monocrystalline structure and wurtzite lattice configuration of the ScAlN, AlGaN, and GaN layers.[75] This TEM analysis underscores the thermal robustness of the ScAlN/AlGaN/GaN gate stack, demonstrating that the structural and compositional integrity of the interfaces can be maintained even under prolonged high-temperature operation. These findings validate the resilience of the ScAlN/GaN platform and its suitability for high-performance electronic applications in harsh environments.

8.3 Operational Principle of Ferroelectric ScAlN/AlGaN/GaN HEMTs

The operational principle of the ferroelectric ScAlN/AlGaN/GaN HEMTs was investigated by varying the drain-source voltage (V_{DS}) and the gate-source voltage end value ($V_{GS,END}$) during the sweep process. Figures 8.2(a) and 8.2(b) present the bi-directional semi-logarithmic transfer characteristics of the HEMTs under different $V_{GS,END}$ values ranging from −1 V to +7 V, with V_{DS} set to 0.5 V and 5 V, respectively. Distinct counterclockwise hysteresis loops are observed in all transfer curves, which are a hallmark of the ferroelectric switching behavior of the ScAlN layer. Hump features in the transfer curves can be attributed to electron trapping and detrapping in the ScAlN/AlGaN/GaN gate stack.[297-299] During the positive V_{GS} sweep, electrons become trapped at interfaces or within the ScAlN and AlGaN layers and are gradually released during the negative sweep, resulting in the hump. This behavior is supported by temperature-dependent measurements showing increased gate leakage (I_G) and the emergence of a small clockwise hysteresis at elevated temperatures during trestings, consistent with thermally activated trapping/detrapping and prior reports.[297, 299, 300]

The memory window (MW) is observed to increase with the increasing magnitude of $V_{GS,END}$, attributed to the negative shift in the transfer curves during the backward sweep. The threshold voltage (V_T) is defined using the constant-current method, where the corresponding V_{GS} value at which the drain current (I_D) reaches 0.1 mA/mm is identified. The MW is quantified as the difference in V_T between the forward and backward sweeps. The observed enlargement of the MW can be attributed to the enhanced partial switching of the ferroelectric domains within the ScAlN layer under higher $V_{GS,END}$, resulting in increased accumulation of the two-dimensional electron gas (2DEG) and a more pronounced negative shift in V_T during the backward sweep. This effect is indicative of the stochastic nature of ferroelectric domain switching and underscores the suitability of ferroelectric ScAlN/AlGaN/GaN HEMTs for multi-bit memory applications. Furthermore, the ferroelectric ScAlN/AlGaN/GaN HEMTs exhibit steep sub-Boltzmann switching characteristics during the backward sweep, achieving an average subthreshold swing (*SS*) as low as 15 mV/decade over two decades of current (ranging from 10^{-6} mA/mm to 10^{-4} mA/mm). This behavior can be attributed to the alignment of the polarization of the ScAlN layer against the polarization discontinuity at the AlGaN/GaN interfaces, which facilitates the depletion of the 2DEG and contributes to the observed steep switching characteristics.

Additionally, it was observed that the V_{DS} did not affect the memory window (MW), but it did influence the subthreshold behavior during the forward sweep. Figure 8.2(c) provides a detailed depiction of the impact of V_{DS} on the bi-directional transfer characteristics of the ferroelectric ScAlN/AlGaN/GaN HEMTs, with a fixed $V_{GS,END}$ of 7 V and V_{DS} spanning from 0.1 V to 10.1 V. The transfer curves in the backward sweep exhibited minimal variation across different V_{DS} values, whereas the forward sweep transfer curves showed a negative shift in the subthreshold region as V_{DS} was increased, accompanied by a degradation in the *SS* value. This degradation of the subthreshold characteristics at higher V_{DS} values during the forward sweep can be attributed to the self-heating effects and the generation of hot electrons caused by high voltage and current stress.[300-303] Such thermal effects could potentially be mitigated through improved thermal management strategies, such as substrate engineering [304, 305] and the adoption of advanced device architectures, [306] in future designs. Furthermore, the ferroelectric ScAlN/AlGaN/GaN HEMTs also demonstrate a high on-off current ratio (I_{on}/I_{off}) exceeding 10^8 across a wide range of V_{DS} values, as shown in Figure 8.2(g). This value ranks among the highest reported for GaN HEMTs [200-202, 204, 206, 228, 272-279] and oxide-based FeFETs [280-296]. It is important to

note that the I_{off} is constrained by the limitations of the measurement system. Additionally, a high transconductance (g_m) of approximately 140 mS/mm was observed during the backward sweep under a V_{DS} of 10.1 V, offering substantial current gain and positioning the device as a promising candidate for high-power, high-frequency applications as well.

Figure 8.2(d) presents the mapping of the MW as a function of V_{DS} and V_{GS} biasing condition for a representative ferroelectric ScAlN/AlGaN/GaN HEMT. It is observed that a stable and large MW of approximately 4 V can be achieved for $V_{GS,END}$ values exceeding 6 V across a broad range of V_{DS}. Figures 8.2(e) and (f) depict the corresponding mapping of *SS* with respect to V_{DS} and V_{GS} biasing under forward and backward sweeps, respectively. Sub-60 mV/dec switching behavior is observed across the entire V_{DS} range during the backward sweep. The devices exhibit consistent behaviors in terms of MW and subthreshold characteristics. The results demonstrate MW values exceeding 3 V and sub-60 mV/dec *SS* under the backward sweep, with some observed device-to-device variation, which can be attributed to process-induced variations during fabrication. Figures 8.2(g) and (h) illustrate the output characteristics of the ferroelectric ScAlN/AlGaN/GaN HEMTs under positive and negative V_{GS} poling, with V_{GS} varying from −2 V to +7 V and +7 V to −2 V, respectively. During positive V_{GS} poling, the drain current (I_D) shows a gradual modulation with respect to V_{GS}, whereas during negative V_{GS} poling, the I_D exhibits more abrupt changes, consistent with the transfer characteristics. A reasonably low on-resistance (R_{on}) of 11.4 Ω·mm and 9.1 Ω·mm is achieved under positive and negative poling conditions, respectively, particularly considering the relatively large source-drain distance (L_{SD}) of 8 μm in this work. Additionally, the devices achieve high on-current (I_{on}) values of 311 mA/mm and 474 mA/mm under positive and negative poling, respectively. The I_{on} is the highest among ScAlN-based GaN HEMTs with an L_G of 1 μm [200-202, 204, 206, 228, 272-279], a performance that can typically only be achieved by oxide FeFETs with highly scaled L_G. [280-296] The notable discrepancy in I_{on} between the two poling conditions can be attributed to self-heating effects [305, 307] and potential ferroelectric domain pinning [308]. During the forward sweep, cumulative heating from prior high-bias points degrades carrier mobility, resulting in a reduced I_{on}.[301] In contrast, during the backward sweep starting from a high V_{GS}, the device initially experiences minimal heating, leading to a higher I_{on}. Additionally, bias-dependent ferroelectric domain dynamics can impact 2DEG modulation, further contributing to the discrepancy.[308] These effects are consistent with literature reports [301, 308] and will be explored in future work.

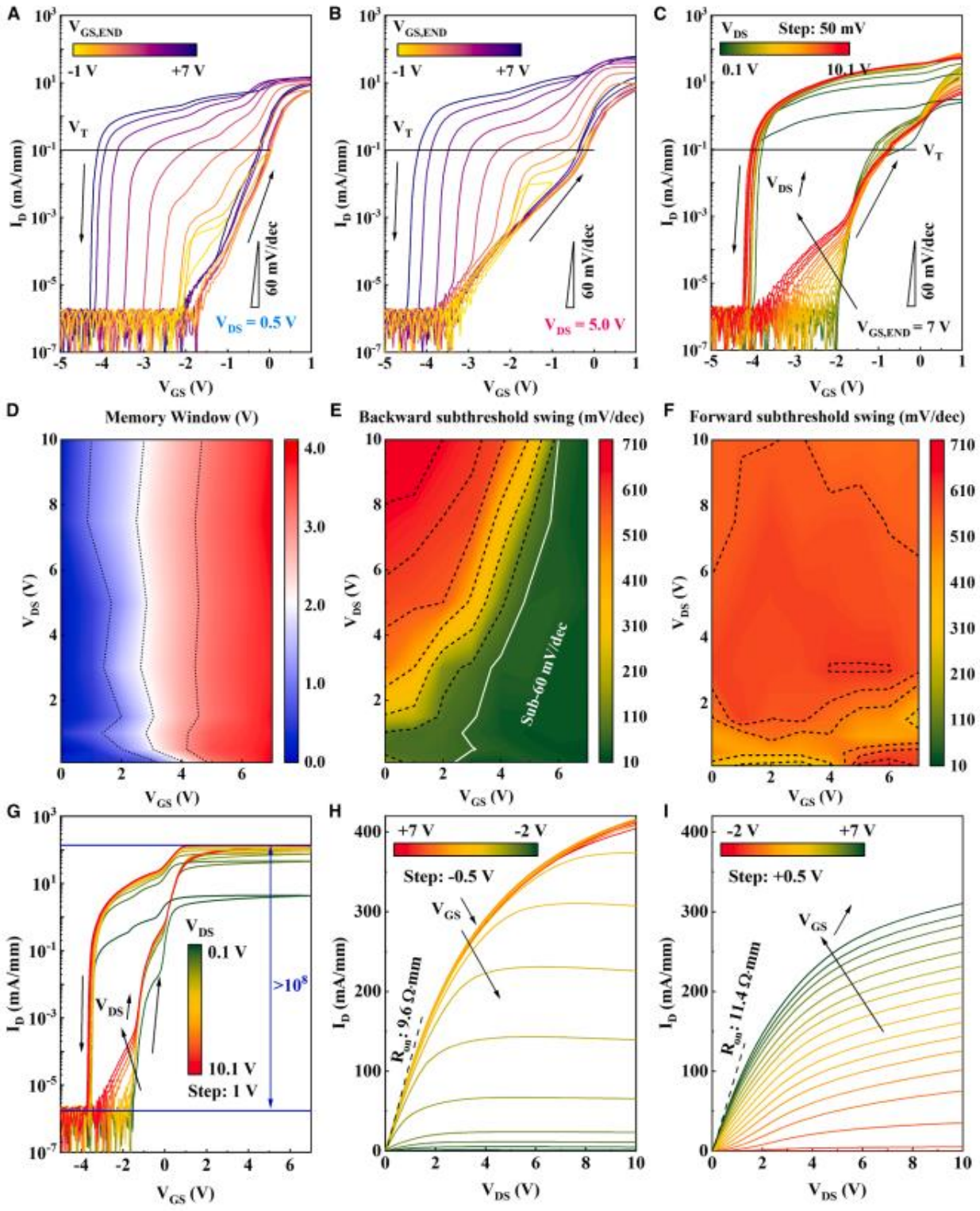


Figure 8.2: Electrical performance of a representative ferroelectric ScAlN/AlGaN/GaN HEMT at room temperature (a–c) Semi-logarithmic transfer characteristics under various bias conditions: (a) fixed V_{DS} of 0.5 V with $V_{GS,END}$, defined as the final V_{GS} value at the end of the voltage sweep, varying from − 1 to +7 V; (b) fixed V_{DS} of 5 V with $V_{GS,END}$ ranging from − 1 to +7 V; and (c) varying V_{DS} from 0.1 to 10.1 V with a fixed $V_{GS,END}$ of +7 V. (d) Dependence of the memory window (MW) on V_{DS} and V_{GS}, showing stable and large MWs of ~4 V. (e and f) Subthreshold swing

(*SS*) as a function of V_{DS} and V_{GS} during (e) forward sweep and (f) backward sweep. Sub-60 mV/dec SS is achieved during the backward sweep, attributed to the ferroelectric switching of ScAlN. (g) Semi-logarithmic double-sweep transfer characteristics under various VDS, demonstrating a high I_{on}/I_{off} ratio exceeding 108 across a wide range of V_{DS}. (h and i) Output characteristics under different V_{GS} poling: (h) V_{GS} from − 2 to +7 V and (I) V_{GS} from +7 to − 2 V.

8.4 Memory Performance of Ferroelectric HEMTs under High Temperature

The memory performance of ferroelectric ScAlN/AlGaN/GaN HEMTs was evaluated at room temperature and elevated temperatures up to 350 °C. Figure 8.3(a) presents the transfer characteristics of the ScAlN/AlGaN/GaN HEMT subjected to manual direct-current (DC) switching cycles up to 300 cycles at room temperature. Figure 8.3(b) illustrates the variation in V_T during the erase and program states as a function of cycle number. A stable MW greater than 3 V is maintained after 300 DC cycles, indicating robust endurance performance of the ScAlN/AlGaN/GaN HEMT. It is important to note that manual DC switching cycles were used instead of conventional pulse-based measurements. This approach places a higher demand on the endurance performance of the device but provides more detailed information by capturing full *I-V* curves.[309] The retention performance of the ScAlN/AlGaN/GaN HEMTs after V_{GS} poling at 7 V and -6 V at room temperature is shown in Figure 8.3(c), where the measurements were performed at a V_{DS} of 0.5 V and V_{GS} of -1.8 V. The devices maintain a distinct I_{on}/I_{off} ratio of 10^4 after extrapolation to 10 years, demonstrating excellent retention performance. The extrapolation was based on a linear fit of the measured current versus time beyond 100 s, plotted on a log–log scale, with the fitting region marked. This performance is consistent with previously reported ScAlN/MoS_2 FETs, validating the potential of ferroelectric ScAlN as a candidate material for non-volatile memory storage.

The ferroelectric ScAlN/AlGaN/GaN HEMTs demonstrate remarkable memory performance at elevated temperatures. Figure 8.3(d) presents the transfer characteristics of the ferroelectric HEMTs after 100 DC switching cycles conducted at 250 °C. A distinct counterclockwise hysteresis loop is observed, confirming that the ScAlN layer retains its ferroelectric switching characteristics at this high temperature. Furthermore, the devices exhibit low I_{off} values at 250 °C, remaining below the detection limits of the measurement system, which contributes to the preservation of robust endurance and retention performance,[250, 262] even under high-temperature operating conditions. However, it is noted that the ferroelectric HEMTs exhibit a negatively shifted V_T and degraded subthreshold behavior at 250 °C, relative to their

room temperature performance. These phenomena can be attributed to thermally generated hot electrons, which enhance the density of the 2DEG in the channel, leading to a negative shift in V_T . Additionally, these high-energy electrons may undergo thermal and/or field emission into the ScAlN ferroelectric layer,[310] leading to an increase in I_G and more pronounced hump features in transfer curves. This behavior also aligns with the negative shift and the corresponding degradation in subthreshold performance observed in the transfer curves under increased V_{DS} bias at room temperature, as depicted in Figure 8.2(c).

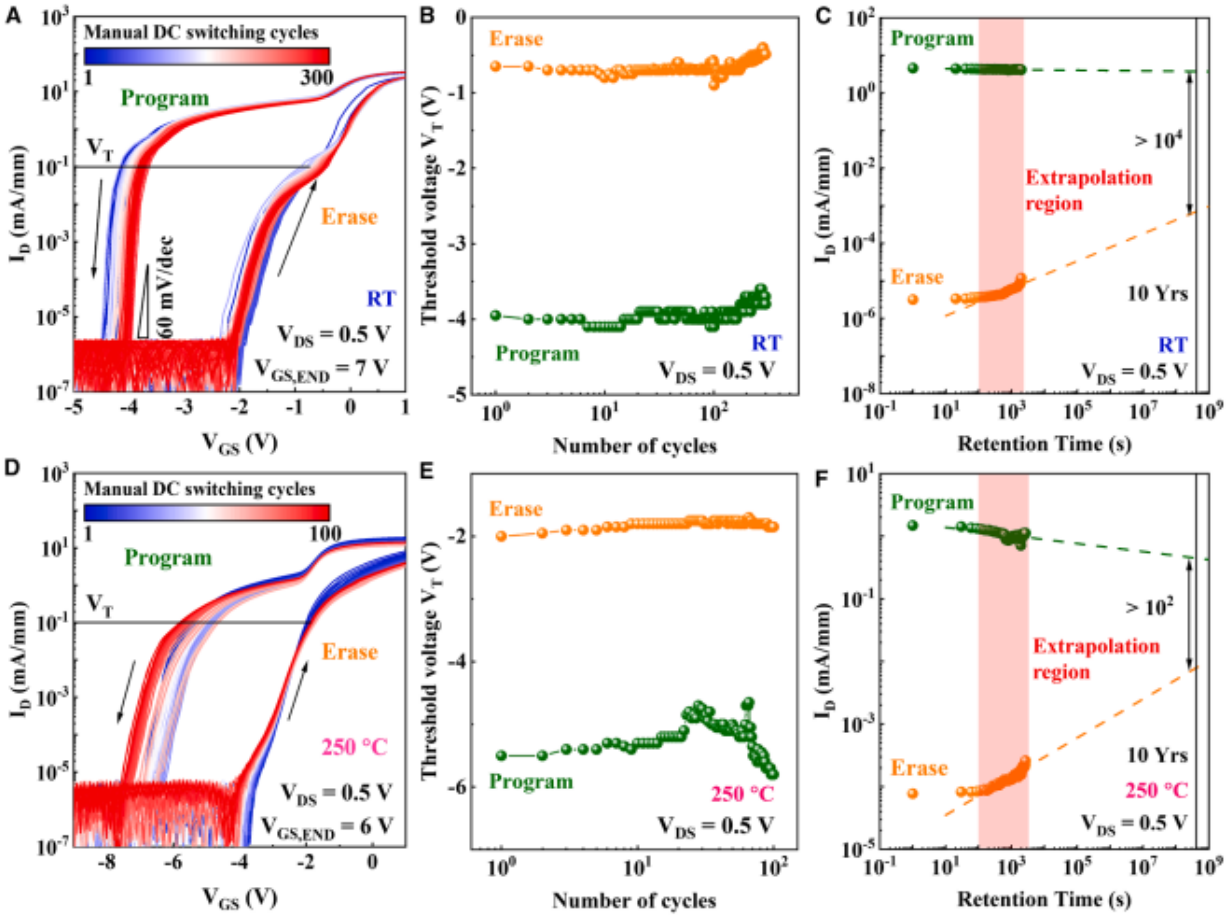


Figure 8.3: Memory performance of a representative ferroelectric ScAlN/AlGaN/GaN HEMT at room temperature and a high temperature of 250 °C (a) Transfer characteristics of the ScAlN/AlGaN/GaN HEMT with manual DC switching cycles up to 300 cycles at room temperature. (b) Endurance performance at room temperature under manual DC switching. (c) Retention performance at room temperature. (d) Transfer characteristics of the ScAlN/AlGaN/GaN HEMT with manual DC switching cycles up to 100 cycles at 250 °C. (e) Endurance performance at 250 °C. (f) Retention performance at 250 °C.

The endurance performance of the ferroelectric ScAlN/AlGaN/GaN HEMTs at 250 °C is shown in Figure 8.3(e), where a stable and large MW greater than 3 V is maintained after 100 DC

switching cycles. Figure 8.3(f) further demonstrates the retention performance of the devices after V_{GS} poling at +6 V and −9 V at 250 °C, with measurements taken at V_{DS} of 0.5 V and V_{GS} of −3 V. Notably, the ferroelectric ScAlN/AlGaN/GaN HEMTs retain a distinct I_{on}/I_{off} ratio greater than 10^2 after a 10-year extrapolation at 250 °C, demonstrating the robustness of the device and positioning it as a candidate for high-performance memory devices in harsh environments. Furthermore, the ferroelectric HEMTs also remain functional at 350 °C. At this elevated temperature, the devices exhibit reasonable endurance, with MW exceeding 2 V after 40 DC cycles, and retention times on the order of tens of minutes. The observed performance degradation at 350 °C is primarily attributed to an increase in I_{off}, which can be explained by the hot-electron-induced gate leakage I_G and trapping events.[311] The increased I_G and enhanced electron trapping/detrapping events are also believed to contribute to the degradation of HfO_2-based ferroelectric memory.[312-314] Further improvements in memory performance, particularly at high temperatures, could be achieved by optimizing material growth conditions,[250, 264] engineering interfaces,[299, 313] enhancing substrate thermal management,[301, 304] and adopting advanced device architectures, such as three-dimensional (3D) structures,[306] to suppress leakage pathways in future designs.

8.5 Multi-Bit Capacity of Ferroelectric ScAlN/AlGaN/GaN HEMTs

Leveraging its large MW and voltage-controlled partial polarization switching, the ferroelectric ScAlN/AlGaN/GaN HEMTs are promising for multi-bit operation, which could increase data storage density.[262] Figure 8.4(a) demonstrates that four distinct current levels, corresponding to a 2-bit memory operation, can be achieved by applying different $V_{GS,END}$ values over 100 cycles of DC switching at room temperature. The distribution of these four well-separated conductance levels over 100 cycles is shown in Figure 8.4(b), indicating successful implementation of 2-bit operation. Higher-bit operations may be feasible by fine-tuning the V_T using pulse measurements in future work.[269] Figure 8.4(c) illustrates how polarization switching in the ScAlN layer modulates the 2DEG density, enabling nonvolatile memory behavior in our HEMTs. Applying a low negative V_G for poling results in upward polarization, which reduces 2DEG density and increases V_T. A higher positive V_G switches the ScAlN domains downward, enhancing 2DEG accumulation and lowering V_T. The stochastic nature of ferroelectric switching allows for multi-bit memory operation.

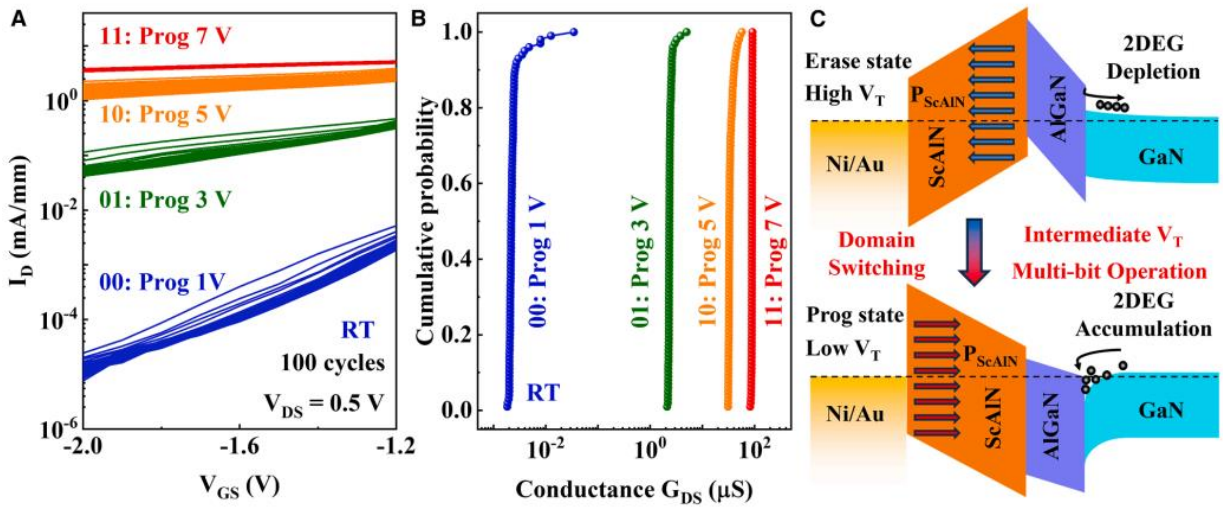


Figure 8.4: Demonstration of the multi-bit capability of the ScAlN/AlGaN/GaN HEMT at room temperature and corresponding energy band diagrams (a) Four distinct current levels obtained by applying different programming gate voltages ($V_{GS,END}$) over 100 cycles of manual DC switching. (b) Distribution of the four well-separated conductance levels over 100 cycles. (c) Energy band diagrams of the ferroelectric ScAlN/AlGaN/GaN HEMT in erase and program states, highlighting nonvolatile modulation of 2DEG density through ferroelectric domain switching in ScAlN

We benchmark our ferroelectric ScAlN/AlGaN/GaN HEMTs against other ferroelectric GaN HEMTs [200, 206, 272-277] and ScAlN-containing GaN HEMTs [201, 202, 204, 228, 278, 279] in Figures 8.5(a) and (b). It is important to note that certain ScAlN-containing GaN HEMTs, particularly those with smaller L_G, do not exhibit ferroelectric hysteresis, as these devices are designed for radio-frequency (RF) applications. Figure 8.5(a) compares the I_{on}/I_{off} ratio versus SS for these GaN HEMTs with our ferroelectric ScAlN/AlGaN/GaN HEMTs, demonstrating enhanced performance of our ferroelectric HEMTs characterized by a steep SS of less than 60 mV/dec and the high I_{on}/I_{off} ratio. Figure 8.5(b) illustrates I_{on} as a function of L_G, demonstrating that I_{on} follows a trend inversely proportional to L_G. Our ferroelectric ScAlN/AlGaN/GaN HEMTs exhibit the highest I_{on} for a L_G of 1 μm. While further scaling of L_G could lead to a boost in I_{on} values, the current achievable I_{on} of 474 mA/mm is sufficient to meet the requirements of most memory applications. We also compare our ferroelectric ScAlN/AlGaN/GaN HEMTs with recently reported oxide-based FeFETs [280-296] in Figures 8.5(c) and (d). Our devices show comparable or improved performance in terms of I_{on}/I_{off}, SS, MW, and retention compared to other oxide-based FeFETs and recently reported ScAlN/MoS_2 FeFETs. However, it should be noted that prior reports have focused on room-temperature evaluations. This work presents the demonstration of ferroelectric ScAlN/AlGaN/GaN HEMTs that can operate at temperatures as high as 350 °C

while maintaining stable logic-memory performance. This is made possible by the robust nature of the well-established GaN platform, which offers advantages for applications in extreme environments. Our ferroelectric ScAlN/AlGaN/GaN HEMTs are thus poised to serve as a viable solution for high-performance memory devices in harsh environments such as avionics, space exploration, autonomous driving, nuclear energy, and geothermal energy harvesting—domains where previously reported FeFETs based on oxide ferroelectric materials or alternative semiconductor channels are likely to encounter functional limitations.

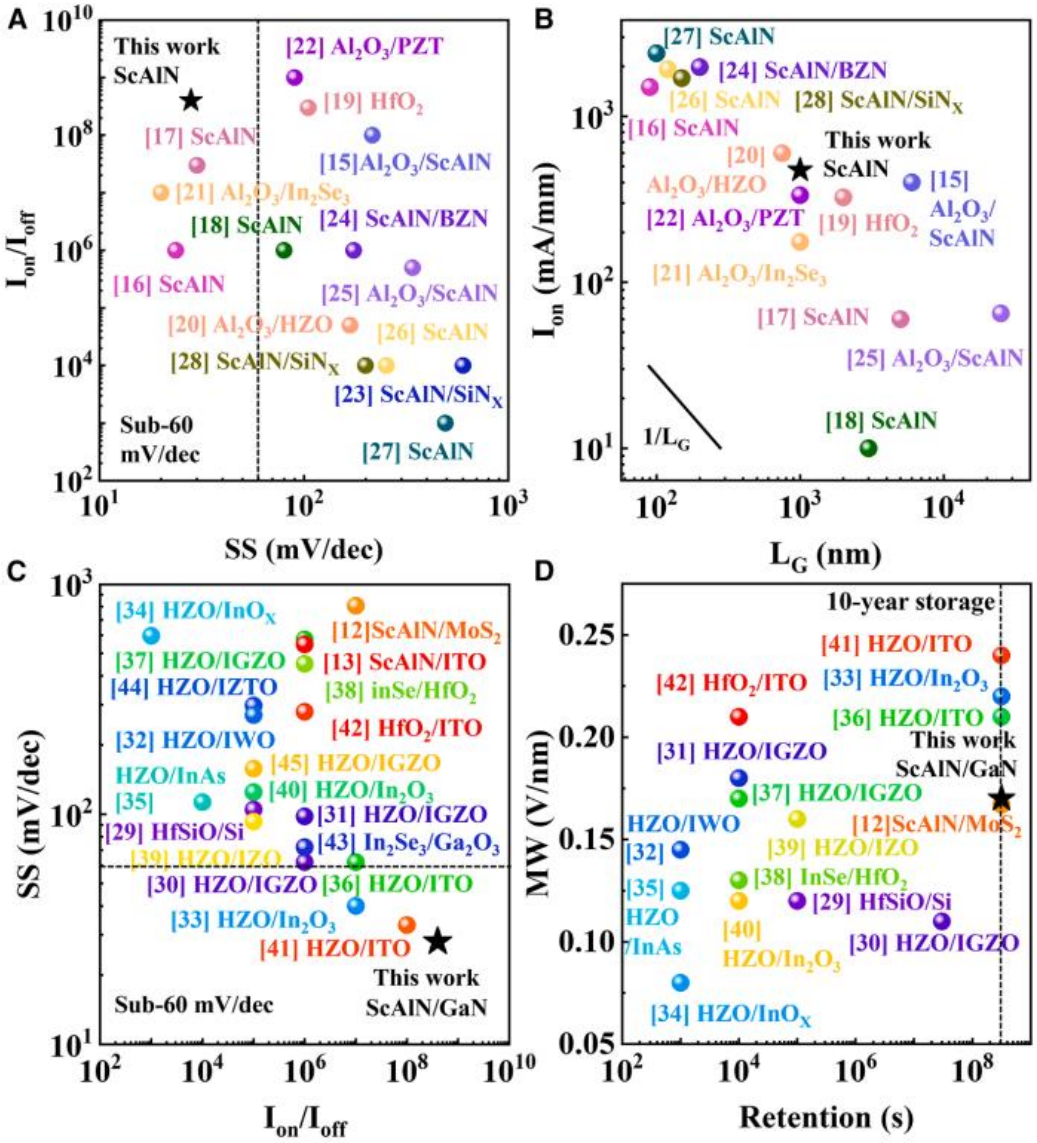


Figure 8.5: Benchmarking of the ferroelectric ScAlN/AlGaN/GaN HEMT in this work against recently reported GaN HEMTs and oxide-based FeFETs (a and b) Benchmarks of (a) Ion/Ioff ratio versus *SS* and (b) Ion versus L_G for the ScAlN/AlGaN/GaN HEMT in this work compared to other ferroelectric or ScAlN-containing GaN HEMTs. It is noted

that some ScAlN-containing GaN HEMTs do not exhibit ferroelectric hysteresis. (c and d) Benchmarks of (c) *SS* versus I_{on}/I_{off} ratio and (d) MW versus retention for the ScAlN/AlGaN/ GaN HEMT in this work compared to recently reported oxide-based FeFETs.

8.6 Conclusion

In summary, we report ferroelectric ScAlN/AlGaN/GaN HEMTs enabled by MBE, demonstrating enhanced logic-memory functionality. These devices exhibit high I_{on}/I_{off}, large I_{on} and g_m, sub-Boltzmann *SS*, wide MW, multi-bit capability, and reliable endurance and retention characteristics. Benefiting from the high-quality material and interface achieved through MBE and the inherent thermal stability and robustness of ScAlN and GaN, they remain operational up to 350 °C. These performance metrics compare favorably to previously reported GaN HEMTs and oxide-based FeFETs, marking an advancement in ferroelectric device technology. Looking forward, performance improvements are anticipated through optimization of material growth conditions, interface engineering, enhanced thermal management using high thermal conductivity substrates, and the adoption of advanced device architectures to mitigate leakage pathways. This work establishes ferroelectric ScAlN/AlGaN/GaN HEMTs as strong candidates for high-performance memory applications in extreme environments, including avionics, space exploration, autonomous vehicles, nuclear energy systems, and geothermal energy harvesting.

Chapter 9 E-mode GaN HEMT with ScAlN/ScN Charge Trap-Coupled Ferroelectric Gate Stacks

9.1 Introduction

The merits of wide bandgap and high electron saturation velocity enable gallium nitride (GaN) an excellent material platform for the next generation of power electronics that can operate fast and endurably under high power and extreme environments.[244, 315-317] These superior properties make AlGaN/GaN-based high electron mobility transistors (HEMTs) a competent candidate for applications in the fields of high power and high frequency applications such as space, 6G communications, data centers, and the automotive industry.[318-320] Despite intense research has been conducted in the design and fabrication of AlGaN/GaN HEMTs, several challenges remain, and addressing these challenges would be critical to realize its commercial viability. The safe operation of power electronics generally requires a low leakage current and an enhancement-mode (E-mode) operation. The normally-off behavior would also ease the load on circuit design by reducing the protection circuits.[321] There have been several approaches proposed and demonstrated to realize the E-mode operation of GaN HEMTs. For example, by reducing the AlGaN barrier thickness to lower the Fermi-level, the 2-dimensional electron gas (2DEG) concentration would be reduced accordingly.[322] Further work on the fluorine-treated surface technique was developed to inject more negatively charged ions to shift the threshold voltage (V_{th}) to achieve E-mode operation.[323] Another approach is to incorporate a p-type GaN gate in the structure to extend the depletion region in the 2DEG layer.[324, 325] However, these methods face process variation issues, limited V_{th} stability or the increased gate leakage.[326-329]

The concept of introducing a charged floating gate or negatively charged oxide dielectric to compensate for the 2DEG carriers in AlGaN/GaN HEMTs was theoretically proposed in 2009

The content of this chapter has been published on *Applied Physics Letters*. The work is supported by the National Science Foundation (NSF) under Grant No. 2235377, the Army Research Office under Grant No. W911NF2420210, and by the College of Engineering at the University of Michigan.

by Hasegawa *et al.* [330]and then experimentally demonstrated by Lee *et al.* in a SiO_2 tunneling dielectric coupled with HfO_2 charge trapping layer to realize E-mode operation [331]. Further works by implementing oxide-based ferroelectric (FE) materials, such as $Hf_xZr_{1-x}O_2$ (HZO) have been shown to be an effective method to provide an additional dimension by modulating the polarization in the gate stack to shift the V_{th} to a positive value and improve electrical characteristics in terms of reconfigurability and subthreshold swing.[332, 333] Nitride ferroelectric materials, such as ScAlN, exhibit superior properties including high breakdown field, large remnant polarization, and high Curie temperature.[59, 68, 72, 250, 334] Properties of ScAlN can be further tuned by varying the scandium composition. For example, its coercive field can be adjusted to potentially support a desired V_{th} tuning window. Along with its large polarization that can achieve a strong ferroelectric charge coupling and its high breakdown field that supports the operation under strong fields, ScAlN is also expected to find suitable applications in power electronics. In addition, it can be grown in situ with the nitride-based AlGaN/GaN channel materials in molecular beam epitaxy (MBE) or metalorganic chemical vapor deposition (MOCVD) systems with a good lattice registry that can significantly reduce defect formation.[22, 32, 36, 81, 206, 207, 220] Successful demonstrations of non-volatile multi-level programmable memory devices based on the ScAlN/GaN heterostructure have shown the merits of large ON/OFF ratios, good retention, superior cycling endurance as well as robust stability under temperatures higher than most ferroelectrics' Curie point.[65, 74] More recently, GaN HEMTs with ferroelectric ScAlN barrier have shown to break the Boltzmann limit of the subthreshold swing (*SS*) of 60 mV/dec while generating wide threshold tuning windows that pave the way to integrate multifunctional devices on the ScAlN platform for the development of power-efficient next-generation electronics.[200, 206] Another transition metal nitride, ScN has a rock salt structure with a direct bandgap of ~ 2 eV, excellent mechanical properties and high temperature stability that would be promising for high temperature electronics.[335, 336] In the meantime, the lattice mismatch between ScN (111) and wurtzite *c*-plane GaN is ~0.1%,[14, 337] which is sufficiently small to support high-quality materials growth on GaN.

In this work, we developed an E-mode GaN HEMT device by constructing a unique gate structure with a ferroelectric scandium aluminum nitride (ScAlN) and monolayer scandium nitride (ScN) charge trapping layer. The ultrathin ScN here acts as an electron reservoir to trap and store the electrons from the 2DEG channel region, transitioning the operation of the GaN HEMT from

D-mode to E-mode. Additionally, the ferroelectric ScAlN barrier with its switchable polarization property would help with the charge trapping to provide additional stability of the trapped carriers and improved subthreshold performance.

9.2 E-mode GaN HEMT Device Structure and Fabrication

Figure 9.1(a) presents the schematic structure of the E-mode HEMT. The HEMT structure was epitaxially grown in a Veeco GENxplor MBE system equipped with a radio frequency (RF) plasma source on a semi-insulating GaN (2 μm)/sapphire substrate, with 100 nm unintentional doped (UID) GaN channel and 10 nm $Al_{0.3}Ga_{0.7}N$ barrier layer grown to form the 2DEG and two monolayers of ScN serving as the charge trap layer on top and finally capped with 27 nm ferroelectric $Sc_{0.2}Al_{0.8}N$ as the coupled gate barrier. Figure 9.1(b) shows the fabrication flow of the device discussed in this work. After the MBE growth of the structure, a SiO_2 hard mask was deposited for selectively etching at the source/drain regions. Heavily doped n^+-GaN ($N_d \sim 10^{19}$ cm^{-3}) was re-grown at the etched regions to establish ohmic contacts with the 2DEG. Subsequently, the isolation step was conducted in a chlorine-based reactive ion etching (RIE) system. Then, a metal stack of 20/120 nm Ti/Au was deposited for source, drain, and gate contacts. The fabricated devices were finally annealed at 600°C for 5 mins in N_2 environment using a rapid thermal annealing (RTA) furnace. The contact resistance, R_C, and sheet resistances, R_{sh} are extracted to be 15 Ω·mm and 2628 Ω/□, respectively, using transfer length method (TLM) measurement at room temperature as shown in Figure 9.1(c). The values are relatively high due to the unoptimized metal stack and fabrication process. Further optimization related to the heterostructure design and regrowth step such as mask removal without incurring damage to the ScAlN is expected to lower the R_{sh} and R_C respectively. The gate length (L_G), the gate width (W_G) and the distance between gate and source/drain (L_{GS}, L_{GD}) were 2 μm, 10 μm and 1.3 μm respectively. All the measurements were done at room temperature. A control sample with a similar structure was fabricated into a capacitor with ScAlN/ScN/AlGaN/GaN sandwiched by Ti/Au metal contact followed by measurement of capacitance-voltage (C-V) characteristic under the frequency of 1 MHz. The result is shown in Figure 9.1(d) and the counterclockwise hysteresis in pristine capacitors confirms the ferroelectricity in the stack. We further confirmed the materials and interface quality by Scanning Transmission Electron Microscopy (STEM). The STEM specimen was prepared by focused ion beam (FIB) milling in an FEI Nova 200, where a cross-section of the bulk material was lifted out using an initial thinning at 30 kV with beam currents of 1.0 nA for

high-current thinning and 0.50 nA for low-current thinning, followed by final thinning at 5 kV with a beam current of 0.12 nA to minimize damage and achieve electron transparency. STEM images were taken on a Thermo Fisher Spectra 300 Probe-Corrected S/TEM operated at 300 keV. High Angle Annular Dark Field (HAADF) STEM images were collected with a probe current of 140 pA, a convergence angle of 30 mrad, and a dwell time of 5us at each pixel. HAADF STEM images of the same region were taken consecutively and then registered to produce a higher signal-to-noise STEM image. Atomic resolution STEM imaging shown in Figure 9.1(e) revealed uniform layer deposition with GaN, AlGaN, and ScAlN displaying characteristic <001> wurtzite structure while the ScN monolayer displayed characteristic <111> rock salt structure.

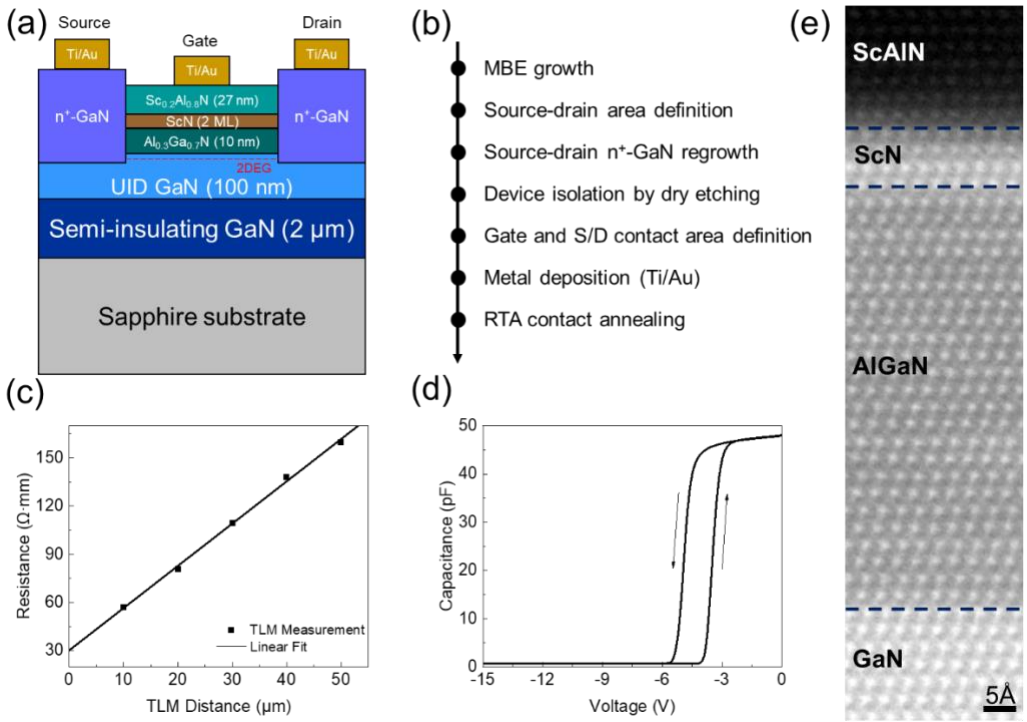


Figure 9.1: (a) Schematic illustration of the ScAlN-gated AlGaN/GaN HEMT with an ultrathin ScN charge trapping layer. (b) Fabrication flow of the AlGaN/GaN HEMT device. (c) TLM measurement results for the AlGaN/GaN 2DEG channel. (d) The counterclockwise *C-V* curve of the ScAlN/ScN/AlGaN/GaN stack confirming the ferroelectricity. (e) Atomic resolution STEM image showcasing the uniformity of the grown layered material. The structure of each layer in the image matches the expected crystal structure of the material.

9.3 Operation Switching from D-mode to E-mode

Figure 9.2(a) shows transfer curves of the GaN HEMT device during the initialization process. The curves were measured in the double-sweep mode with a fixed drain bias V_{DS} = 1 V. V_{GS} swept from −5 V to various positive endpoints $V_{GS,max}$ up to 10 V, which was determined based

on the gate leakage behavior, then swept back to −5 V. ON/OFF ratios remain high (> 10^7) throughout the initialization process. Clear clockwise hysteresis is observed at higher $V_{GS,max}$ (8 V and 10 V) due to the filling of charge traps in the ScN layer. The difference of initial threshold voltages exhibited in Figure 9.2(a) and Figure 9.1(d) is mainly due to the different starting voltage of scans for purposes of injecting carriers and confirming the ferroelectricity, respectively. For this study, the V_{th} is defined for the backward sweep V_{GS} with a fixed current density of 0.01 mA/mm. The V_{th} during the initialization process is shown in Figure 9.2(b) as a function of the endpoint of forward sweep $V_{GS,max}$. The D-mode behavior was observed until the forward sweep reached $V_{GS,max}$ = 6 V and the V_{th} shifted to the positive side until $V_{GS,max}$ reaches 8 V and continues to shift as the gate bias increases until $V_{GS,max}$ = 10 V, where the V_{th} reaches 1.3 V.

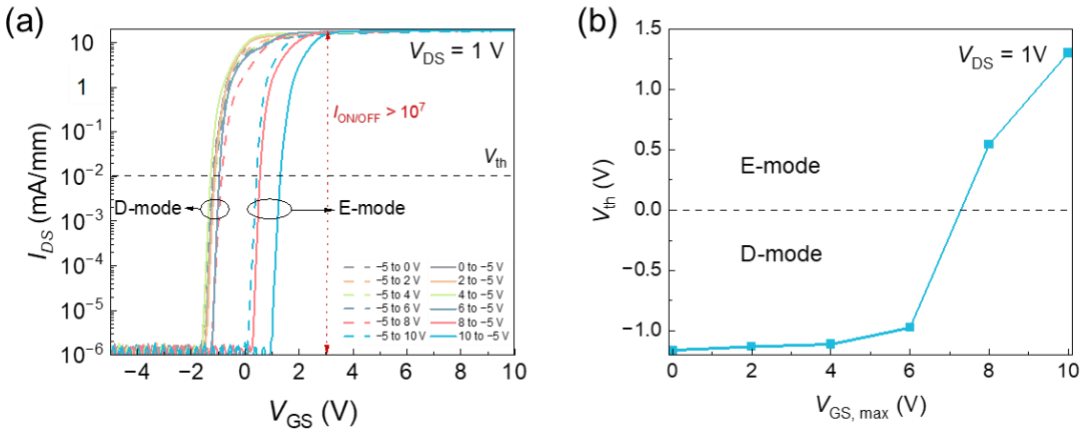


Figure 9.2: (a) Transfer characteristics of the devices. (b) Extracted V_{th} as a function of the endpoint of forward sweep V_{GS}.

The E-mode operation is achieved with the ferroelectric ScAlN coupled with the charge trap layer of ScN. Initially, the polarization of the as grown metal-polar ScAlN is pointing to the sample surface.[68] During the initialization process, as illustrated in Figure 9.3(a), electrons from the 2DEG formed at the AlGaN/GaN interface gradually get extracted to the ScN charge trap layer. In the meantime, when the $V_{GS,max}$ is large enough to switch the polarization of ScAlN to the direction pointing toward the substrate, the polarization charges will further lower the barrier to significantly inject the carriers from the channel to the ScN well.[330, 331] As higher gate biases are applied to the gate, more carriers will be trapped in the ScN layer until all the 2DEG carriers are depleted from the AlGaN/GaN interface. The initialization process completed with the device operation transits from D-mode to E-mode, benefiting performance in power switching

applications.[338] After the process is completed, positive polarization charges in the switched ScAlN layer will continue to hold most carriers in the ScN layer, lowering the Fermi level even when the gate bias is zero, as illustrated in Figure 9.3 (b), to stabilize the E-mode operation.

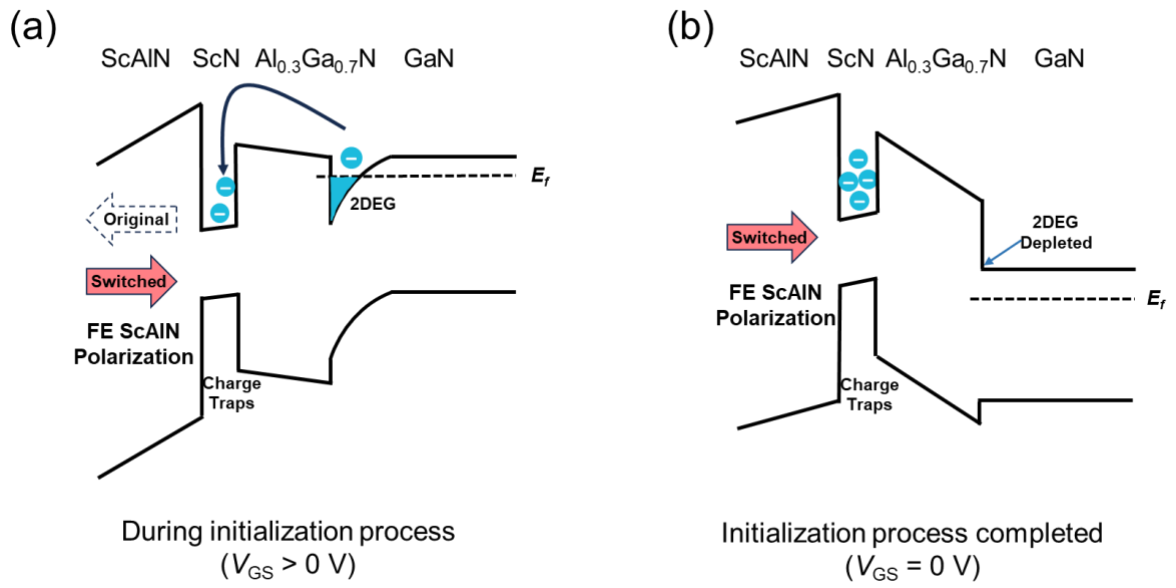


Figure 9.3: Schematic band diagram of the HEMT device illustrating the initialization process. (a) during the initialization where V_{GS} is large enough to switch the ScAlN polarization and reduce the barrier height to inject electrons from the 2DEG region into ScN trap layer. (b) V_{GS} withdrawn (= 0 V) after the initialization process and carriers are trapped in the ScN layer due to the switched polarization of ScAlN, lowering the Fermi level to realize a stable E-mode operation.

9.4 E-mode Stability Testing

To verify the E-mode operation stability, especially under high drain bias for power electronics applications, we first initialized the device by setting forward sweeping voltage, $V_{GS,max}$ to 10 V for trapping the 2DEG electrons to the ScN layer. After the initialization, we tested the transfer characteristics of the device 20 times with the same bias condition, *i.e.,* V_{GS} sweeping from 0 V to 6 V and finally sweeping back to 0 V with a fixed V_{DS} = 10 V. This V_{GS} sweeping range was determined based on the initialization process that within such a relatively low voltage range, there should be negligible carriers injected to the ScN thus no positive V_{th} shift should be incurred during the stability testing. The initial 20 transfer curves are plotted in Figure 9.4(a). It is noticed that the V_{th} will gradually shift to a lower value but tends to become relatively stable as shown from the inset figure. Such V_{th} shifts are due to the carriers getting slowly released from the ScN charge trap layer after the initialization process is completed. To study the device stability over time, we have set a series of time intervals from a few seconds to days between the completion of the initialization

process and the stability tests to observe the V_{th} shifts. The results were measured under the same condition (relatively low V_{GS}, high V_{DS}) as mentioned above and are plotted in Figure 9.4(b). It demonstrates similar behavior as in the previous tests that V_{th} showed an initial shift towards the left but become relatively stable after 100 seconds with V_{th} ~ 700 mV. Within the tested time scale of our measurements (> 3 days), we observed that the device remains to operate in E-mode without the need for any additional initialization process. This indicates that such a unique design can enable a relatively robust E-mode operation, which is largely due to the strong polarization in the switched ScAlN.

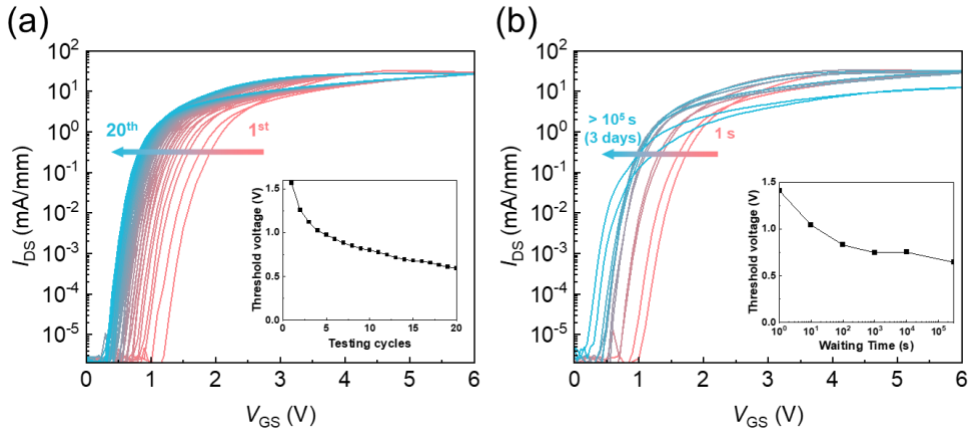


Figure 9.4: Transfer characteristics stability test under a double sweep mode that V_{GS} swept from 0 V to 6 V and back to 0 V with fixed V_{DS} = 10 V. (a) The device experienced 20 cycles of testing after initialization to E-mode operation. (b) The device was tested with waiting time, defined as the time interval between the initialization process and the tests, in a range from 5 seconds to more than 3 days. Insets shown the extracted V_{th} during the stability tests.

Figures 9.5(a-b) shows the output curves of the HEMT devices before and after the initialization process with the V_{GS} applied in a range of −2 to 2 V with a 500 mV step. It is evident that the drain current is much higher before the initialization, indicating a clear depletion mode operation while the threshold voltage is confirmed to be moving to a more positive value after the initialization process. Furthermore, we have characterized the breakdown behavior at its OFF-state, and within the limit of our testing equipment (100 V), no breakdown was observed. The sub-threshold swing of the device is plotted in Figure 9.5(c). Compared with most GaN HEMTs with ferroelectric barriers to achieve E-mode operation, where the *SS* can be above 100 mV/dec,[272, 275, 339] we have achieved an *SS* as low as 61 mV/dec which is close to the Boltzmann limit [340]. The low *SS* can be attributed to two aspects. On one hand, the whole HEMT structure, including the ScN charge trapping layer and the ferroelectric gate ScAlN were epitaxially grown

in the same MBE chamber, which provides a high-quality film with low trap densities at the interface.[22] On the other hand, the ferroelectric ScAlN gate supports an improved modulation on the 2DEG channel, in which the depletion or the injection of the carrier can be effectively tuned by aligning the polarization field in the ferroelectric layer with the applied gate voltage.[333] A benchmark plot of *SS* and the $I_{ON/OFF}$ of E-mode GaN HEMT devices with various ferroelectric materials as gate is shown in Figure 9.5(d), which confirms our device with a low *SS* and relatively high ON/OFF ratio.[272, 275, 277, 333, 339] These results indicate the hybrid gate stack of ScAlN/ScN could be a great candidate for future high-speed and energy-efficient power electronics.

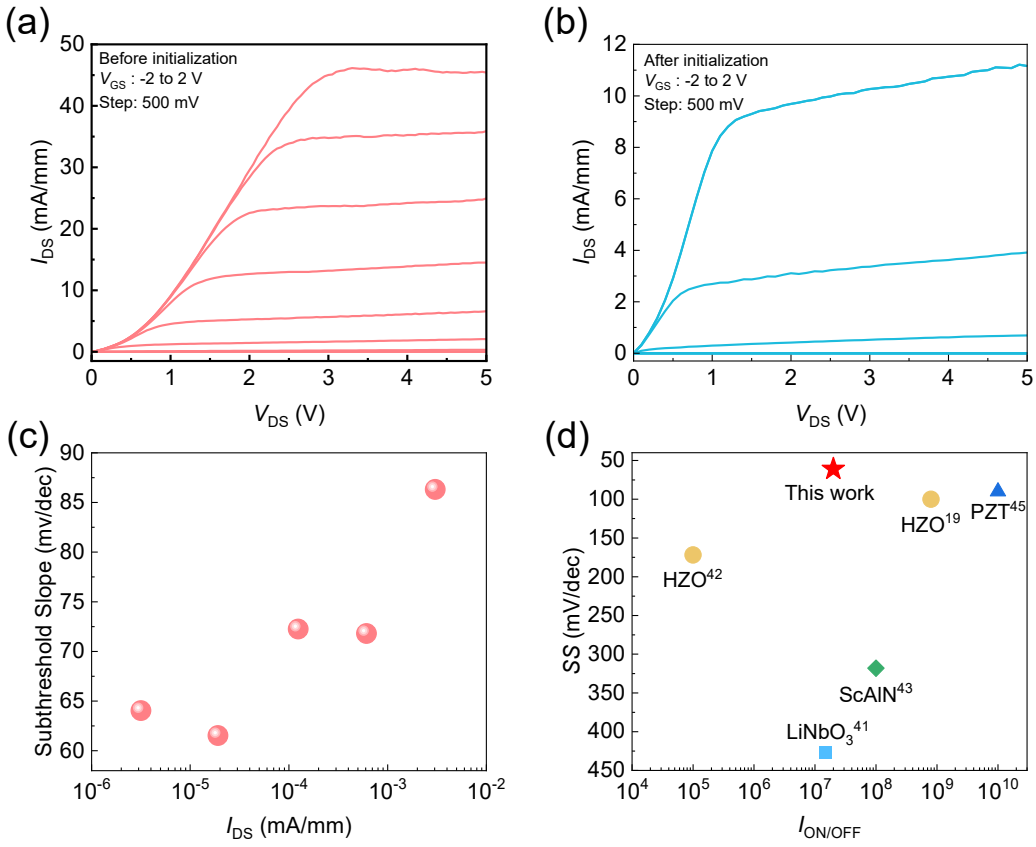


Figure 9.5: (a-b) Measured output characteristics of the HEMT device with V_{GS} from −2 to 2 V with a 500 mV step (a) before and (b) after the initialization process. (c) Extracted subthreshold slope under various drain current densities. (d) Benchmark plot of *SS* and ON/OFF ratio of our E-mode GaN HEMT with ferroelectric ScAlN gates.

9.5 Conclusion

The incorporation of ferroelectric ScAlN in the structure provides a controllable path to switch the polarization in the barrier so that a wider V_{th} tuning window can be achieved. Compared

to the conventional oxide ferroelectric materials, ScAlN shows a larger coercive field that is capable to retain trapped carriers in the charge trap layer after the initialization process is completed [21, 22] and leads to a stable E-mode operation even under high power environment. Furthermore, ScAlN, GaN and ScN can all be epitaxially grown in MBE and share good lattice registry, limiting the formation of interface defects to improve the device performance. ScAlN also demonstrates superior ferroelectric stability under high temperature,[341] holding promise to preserve stable E-mode operation even under harsh environment such as high temperature.

As the field of high-power devices grows rapidly in electric vehicles and renewable energy integration, a stable E-mode GaN HEMT device with a large threshold voltage is urgently required. In this work, an all-epitaxial AlGaN/GaN HEMT structure with an ultrathin ScN layer coupled with a ferroelectric ScAlN gate stack has been demonstrated. The device can operate stably in a normally-off mode after a simple initialization step under $\leq$ 10 V and stays stable during the operation, which would be beneficial for a fail-safe operation in power integrated circuits as well as digital electronics applications. Further improvements on higher current density and better threshold tunability are possible by reducing the contact resistance and optimizing the structure design, which will make the GaN HEMT coupled with the ferroelectric gate more competitive in the power electronics market.

Chapter 10 Ferroelectric ScAlN coupled Al-rich AlGaN-channel HEMT

10.1 Introduction

Ultra-wide bandgap (UWBG) III-nitride semiconductors with high breakdown fields and saturation velocities are ideal for mm-wave and terahertz electronics, enabling efficient, high-gain power amplifiers, and high-temperature electronic applications.[342-344] Among these, Al-rich AlGaN-channel HEMTs have emerged as a promising architecture for achieving superior performance in high-power and high-temperature environments due to their enhanced electron transport properties.[343, 345] Al-rich AlGaN (~50% Al) offers an estimated higher breakdown field (>10 MV/cm) and saturation velocity (>1.5×10^7 cm/s), promising greater power gain and density than GaN.[345, 346] A higher breakdown field results in a significantly elevated Baliga figure of merit (BFOM), even though AlGaN alloys exhibit lower electron mobility compared to GaN. However, despite the promising advantages, several practical challenges, such as poor ohmic contacts, lack of matching dielectric materials, and current collapse due to material defects and interface quality, have prevented Al-rich transistors from realizing their full potential.[342] In 2008, Nanjo *et al.* demonstrated the first $Al_{0.20}Ga_{0.80}N$-channel HEMT.[347] Gaevski *et al.* reported large drain current density (I_D) of ~1.3 A/mm for $Al_{0.40}GaN_{0.60}N$-channel metal-oxide semiconductor (MOS)-HEMT due to low ohmic contact resistance (R_C) of 1.7 Ω·mm and better gate dielectrics of Al_2O_3/ZrO_2.[348] A very low R_C of 0.43 Ω·mm with I_D of 250 mA/mm for AlN (barrier)/$Al_{0.50}Ga_{0.50}N$ (channel) HEMT were reported by Maeda *et al*.[349] An excellent switching performance, with an I_{ON}/I_{OFF} of ~10^6, was also demonstrated in AlN/$Al_{0.50}Ga_{0.50}N$ HEMTs featuring highly degenerate n-doped (~2.6×10^{20} cm^{-3}) regrown GaN contacts, maintaining stability even at elevated temperatures up to 300 °C.[350] Recently, Zhu *et al.* reported the lowest R_C of 0.25 Ω·mm for $Al_{0.82}Ga_{0.18}N$ metal semiconductor field effect transistor (MESFET) using composition grading (AlN mole fraction ranging from 0.85 to 0.14) for the AlGaN contact layer

The content of this chapter has been published on *Applied Physics Letters*. The work is supported by Army Research Office (Grant Nos. W911NF2420210 and W911NF2220176), Sandia National Laboratory, and ARO DEVCOM (Grant No. W911NF2220163) (UWBG RF Center, Program Manager Dr. Tom Oder), and by the College of Engineering at the University of Michigan.

with degenerate doping and proper interfacial engineering.[351] Tokuda *et al.* demonstrated the high-temperature operation of $Al_{0.86}Ga_{0.14}N/Al_{0.51}Ga_{0.49}N$ HEMT with an I_D of 25.2 mA/mm at gate bias (V_{GS}) = 4 V and drain bias (V_{DS}) = 50 V at room temperature (RT), while I_D was reduced by 20% at 300 ºC from its value of RT.[352] *Klein et al.* reported a small reduction of I_D from its RT value (~7.2 mA/mm) to 600 ºC (~4.4 mA/mm) for $Al_{0.86}Ga_{0.14}N/Al_{0.70}Ga_{0.30}N$ HEMT.[343] Moreover, the estimated sheet charge density in AlGaN heterostructures, with various compositions of the barrier and channel, has been observed to reach approximately ~10^{13} cm^{-2}.[342, 349] These results indicate that AlGaN-channel HEMTs are promising candidates for high-frequency, high-power, and high-temperature operations.

The incorporation of alternative barrier materials, such as scandium aluminum nitride (ScAlN), in III-nitride HEMTs introduces an additional degree of freedom to engineer polarization and electric fields within the device, enabling unprecedented control over their performance.[59, 72, 206, 353] The lattice compatibility between ScAlN and AlGaN facilitates high-quality, heteroepitaxial growth, minimizing defects and improving device reliability. In 2017, Hardy *et al.* reported a high 2DEG density of 3.14×10^{13} cm^{-2} with a Hall mobility of 910 $cm^2/V\cdot s$ at RT for ScAlN/GaN heterostructure.[220] Green *et al.* further investigated the RF performance of ScAlN/GaN HEMT, achieving the extrinsic cutoff frequency and maximum oscillation frequency of 88 and 91 GHz respectively.[201] Hasan *et al.* demonstrated that AlScN/GaN HEMT exhibited a high I_D of above 1 A/mm at 423°C.[203] Zhao *et al.* studied the effect of AlScN poling conditions on the ferroelectric HEMT performance, demonstrating a large threshold voltage swing of 3.26 V.[273] MOCVD-grown AlScN/GaN heterostructures were also grown by Streicher *et al.*, achieving high sheet carrier density of 3.25×10^{13} cm^{-2}.[221] A very high I_D of 4 A/mm with a maximum oscillation frequency pushed above 130 GHz was reported for AlScN/GaN HEMTs by and Nomoto *et al.* [354] and Casamento *et al [200]*. Even at 400°C, Wang *et al.* showed that ScAlN/GaN-based memristors maintained a rectifying ratio over 10.[65] In 2021, full epitaxial, single-crystalline, ferroelectric ScAlN (ScN mole fractions between 0.14 – 0.36) on n-GaN, with a residual polarization of ~ 135 μC/cm^2 and a coercive field of ~ 4.2 MV/cm at 10 kHz, was achieved by Wang *et al*.[22] Thus, the inherent feature of ferroelectricity in ScAlN opens avenues for HEMTs for next-generation nonvolatile and reconfigurable power memory and radio frequency applications. Recently, Wang *et al.* demonstrated a fully epitaxial ScAlN/AlGaN/GaN based ferroelectric HEMTs with an inclusive threshold voltage tuning range of 3.8 V, an I_{ON}/I_{OFF}

ratio of 3×10^7, and reconfigurable output characteristics. The coupling between the ferroelectric ScAlN barrier and the UWBG Al-rich AlGaN channel is expected to offer a robust platform for achieving high-power, high-frequency, and multifunctional device performance.

10.2 Integration of Ferroelectric ScAlN to $Al_{0.50}Ga_{0.50}N$-channel HEMT

In this study, we demonstrate a HEMT with the integration of an MBE-grown ferroelectric $Sc_{0.15}Al_{0.85}N$ barrier and a MOCVD-grown $Al_{0.50}Ga_{0.50}N$ channel, focusing on its capability to dynamically control the 2DEG and enhance device performance. The device exhibited a maximum I_D of approximately 16 mA/mm at V_{GS} = 1 V and V_{DS} = 10 V. The transfer characteristics displayed a counterclockwise hysteretic loop, attributed to ferroelectric switching. A large threshold voltage tuning range of 6.4 V was observed at V_{DS} = 1 V. Additionally, the device achieved a low subthreshold swing (*SS*) of ~ 65 mV/dec when tuning the gate bias voltage from positive to negative. Notably, I_D increasing during high-temperature operation up to 400°C, which contrasts with the typical behavior observed in III-nitride HEMTs reported in the literature.[257, 343]

The $Sc_{0.15}Al_{0.85}N$ barrier was grown using MBE on MOCVD-grown $Al_{0.50}Ga_{0.50}N$ channel for HEMT operation. Figures 10.1(a) and (b) show a schematic illustration of an $Sc_{0.15}Al_{0.85}N/Al_{0.50}Ga_{0.50}N$ HEMT on AlN/sapphire substrate and a top-view of SEM image of the proposed device. The structure consists of barrier layers with $Sc_{0.15}Al_{0.85}N$ (20 nm) and n-$Al_{0.73}GaN_{0.27}N$ (15 nm), an unintentional doped (UID) $Al_{0.50}Ga_{0.50}N$ channel (80 nm), and an AlN buffer layer (50 nm). A 1 nm GaN and 1 nm AlN layer were grown on the n-$Al_{0.73}GaN_{0.27}N$ layer using MOCVD, serving as the base layer for ScAlN growth in the MBE chamber. The GaN layer was thermally decomposed in the MBE chamber at substrate heater 800 °C for 20 mins prior to MBE regrowth to expose a pristine AlN surface followed by Ga-assisted in-situ cleaning to further clean the interface, while the AlN layer was incorporated to prevent impurity incorporation and enhance both 2DEG mobility and sheet density. The energy band diagram with the first-state wavefunction is shown in Figure 10.1(c). The combination of AlN and n-doped $Al_{0.73}GaN_{0.27}N$ layers facilitate electron accumulation at the barrier and $Al_{0.50}GaN_{0.50}N$ channel interface. The MBE-regrown $Sc_{0.15}Al_{0.85}N$ layer will follow the metal-polarity of the bottom AlGaN layer and further enhanced the 2DEG density from ~ 4.5×10^{12} cm^{-2} (for n-$Al_{0.73}GaN_{0.27}N/Al_{0.50}GaN_{0.50}N$ heterostructure) to ~ 2×10^{13} cm^{-2}, attributed to its strong polarization and large conduction band discontinuity.[234] The device fabrication process flow for HEMT with regrown contacts is shown

in Figure 10.1 (d). To form ohmic contacts to the 2DEG, a SiO_2 hard mask was first used to define the source and drain regions followed by dry etching and selective-area regrowth of heavily Si-doped n^+-GaN (with a donor concentration of approximately $N_a \sim 3\times10^{20}$ cm^{-3}) at these regions with MBE. Ti/Au (20/200 nm) source/drain metal stacks were deposited on the regrown n^+-GaN, while Ni/Au (20/200 nm) was used for Schottky gate metallization. Using the transfer length method (TLM), a relatively high specific ohmic contact resistivity of 1.57×10^{-3} $\Omega\cdot cm^2$ was measured, indicating limited interface quality between the regrown n^+-GaN and the 2DEG. However, the reverse graded layer approach presents a promising method to further improve contact resistivity.[351] The gate length (L_G), gate-to-source distance (L_{GS}), gate-to-drain distance (L_{GD}), and gate width (W_G) were set at 1, 2, 5, and 10 µm, respectively.

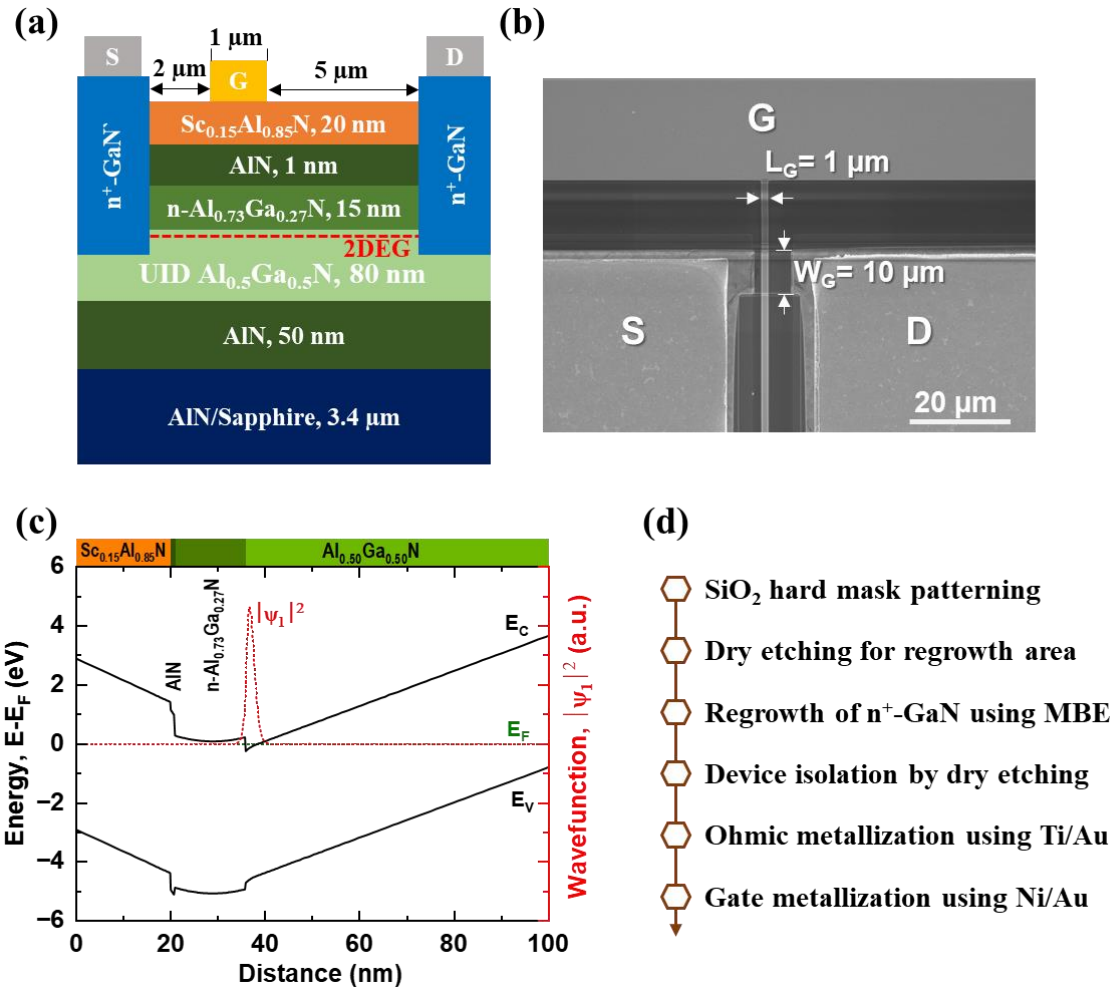


Figure 10.1: (a) Schematic illustration of ScAlN/AlGaN HEMT and (b) top-view of SEM image of the proposed device, where the scale bar represents 20 µm. (c) Energy band diagram of the proposed schematic structure with the ground state wave-function illustrated. The solid black curve, dotted green curve, and red dotted curve represent the

conduction and valence band energies, Fermi level, and wavefunction, respectively. (d) Illustration of the fabrication process flow.

10.3 Device Characterization

Device characterization was performed using an MMR variable-temperature microprobe (VTMP) system equipped with a Joule-Thomson thermal stage. Temperature control was achieved using an MMR K2000 digital-temperature controller under a vacuum pressure of 4 mTorr, with stage temperatures varied from RT to 400°C. DC characteristics were measured using a Keysight B1500A semiconductor parameter analyzer. Figure 10.2 shows the static characteristics of the fabricated ScAlN/AlGaN HEMTs at RT. The drain voltage varied from 0 to 10 V with different gate-voltages for output characteristic curves (Fig. 10.2(a)), and V_{GS} was varied from +1 V (on-state) to −25 V (off-state) to +1 V (on-state) with a fixed V_{DS} of 5 V for transfer curves (Fig. 10.2(b)). The maximum drain current, I_D defined at V_{GS} = 1 V was ~ 16.3 mA/mm with an on-resistance (R_{on}) value of ~ 340 Ω·mm at RT. These drain current and on-resistance results are in good agreement with the values reported in the literature.[343, 352] An I_{ON}/I_{OFF} of 2.3×10^{6} was achieved at V_{DS} = 5 V with a gate leakage current density of 5.53×10^{-6} mA/mm during the off-state at RT, shown in Figure 10.2(b). This result indicates that the off-state current is limited by the gate current due to the high-quality epitaxial layer beneath the gate. The polarization-driven modulation enhances gate control and improves subthreshold swing (*SS*).[206, 276, 355] Thus, a clear and distinct counterclockwise hysteresis behavior was observed and is attributed to the ferroelectric properties of the epitaxial ScAlN.[206] The memory window (ΔV) is defined as the difference in threshold voltage (V_{th}), measured at I_D = 0.01 mA/mm, between the forward and reverse transfer curves. A wide ΔV of 2.1 V was obtained at V_{DS} = 5 V, indicating that the ferroelectric ScAlN/AlGaN HEMT is a promising candidate for next-generation memory applications.

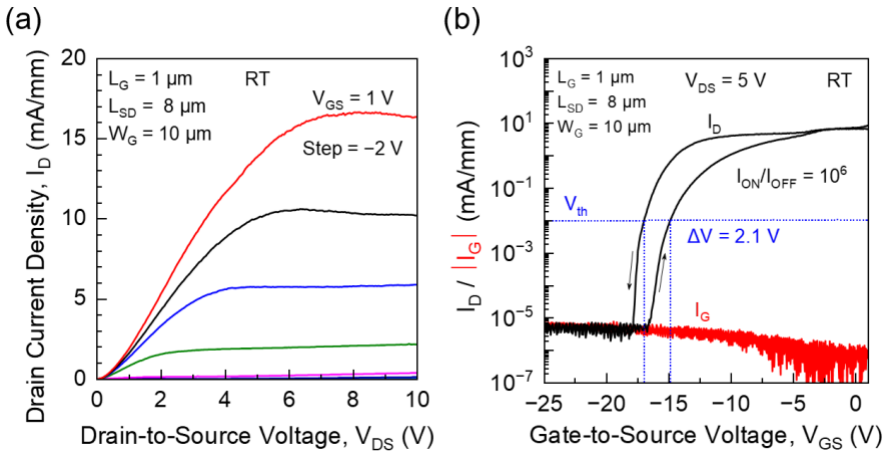


Figure 10.2: (a) Static characteristics of the fabricated ScAlN/AlGaN HEMT at room temperature (RT). (b) Transfer curves (black curve) and gate leakage current (red curve), which were measured at V_{DS} = 5 V. The threshold voltage (V_{th}), defined at 0.01 mA/mm, is represented by the horizontal blue dotted lines. Vertical blue dotted lines are shown to indicate the forward and backward V_{th}.

Figure 10.3 (a) illustrates the transfer curves at two different V_{DS}, demonstrating the regulation of the electric field within the channel. The forward sweep is defined as the direction of V_{GS} bias from off-state (−25 V) to on-state (+1 V), while the opposite direction of V_{GS} bias from on-state (+1 V) to off-state (−25 V) is defined as backward sweep. No significant difference in V_{th} was observed for the two V_{DS} values during the forward gate bias sweep. However, a pronounced shift in V_{th} was noted during the backward gate bias sweep. An increase in off-state current, which corresponds to gate leakage current increase (I_G = 1.93×10^{-6} mA/mm for V_{DS} = 1 and 5.53×10^{-6} mA/mm for V_{DS} = 5 V) under high V_{DS} bias indicates that electrons are captured/trapped in the barrier layers. This trapping effect results in a positive shift in V_{th} when V_{GS} is swept from positive to negative.[356] It is noted that at lower drain bias voltages, the trapping/de-trapping effects have a reduced influence on the counterclockwise hysteresis, which is primarily governed by ferroelectric charge coupling.[206] The precise optimization of growth conditions may help suppress trapping and de-trapping effects, fostering superior carrier transport, smoother interface quality, and enhanced long-term device reliability and performance. The device exhibited a wide ΔV of 2.1 V for the V_{DS} = 5 V, while it was enhanced to 6.4 V for V_{DS} = 1 V, also shown in Figure 10-3(a). The value of ΔV is ~ 4 times higher than the reported ScAlN/GaN ferroelectric HEMTs for V_{DS} = 1 V. Figure 10.3(b) presents the extracted SS for different I_D measured in the device under both forward and backward gate biases. The V_{GS} step was fixed at 50 mV for all measurements. The SS values (~ 65 and ~ 104 mV/dec for V_{DS} = 1 V and 5 V, respectively) are

lower when the device is measured under backward sweep gate bias originating from the polarization in the ScAlN facilitates the depletion of the 2DEG compared to the values (~ 219 and ~ 333 mV/dec for V_{DS} = 1 V and 5 V, respectively) measured under forward sweep, regardless of V_{DS}. The lowest *SS* value, ~ 65 mV/dec for V_{DS} = 1 V, is close to the Boltzmann limit. The tunable V_{th} and low *SS* exhibit great potential for future memory devices and multifunctional transistors.

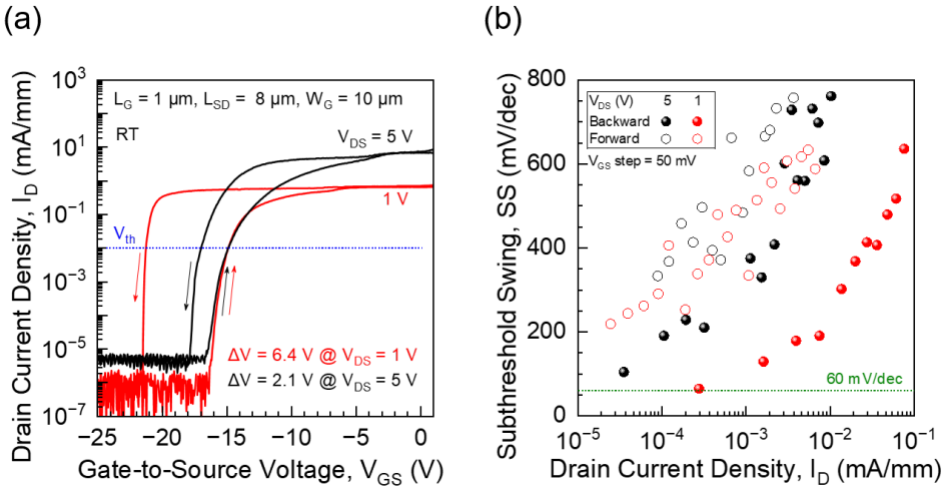


Figure 10.3: (a) Transfer curves for different V_{DS} at RT. Red and black curves represent the transfer curves, which were measured at V_{DS} = 1 and 5 V, respectively. The threshold voltage (V_{th}), defined at 0.01 mA/mm, is represented by the blue dotted line. (b) Subthreshold swing, SS versus drain current density, I_D for both forward and backward gate bias sweeps with different V_{DS}. The V_{GS} step was fixed at 50 mV. The olive dotted line represents the Boltzmann limit.

To investigate the poling conditions on the ferroelectric HEMT behavior, we have varied the sweeping path of V_{GS}. By setting the V_{GS} step from 10 mV to 50 mV, we observed a clear trend of the ΔV becoming wider with larger V_{GS} step as shown in Figure 10.4(a). This is because the backward scan leads to a sharp 2DEG depletion originating from the ScAlN switching and the smaller V_{GS} step will increase the total poling time, reducing the hysteresis here. Figure 10.4(b) further investigated the V_{GS} scan path on the hysteresis. By varying the endpoint of the forward sweep gate voltage $V_{GS,\,max}$ from negative (–1 V) to positive (4 V), the ferroelectric ScAlN will be gradually switched, enlarging the hysteresis window. Although the observed hysteresis and previously reported PUND results[22] are consistent with ferroelectric switching, similar effects may also originate from charge trapping.[357] Moreover, recent studies suggest N-polar switching under positive bias in ScAlN,[69] motivating future atomic-scale investigations to fully decouple these contributions.

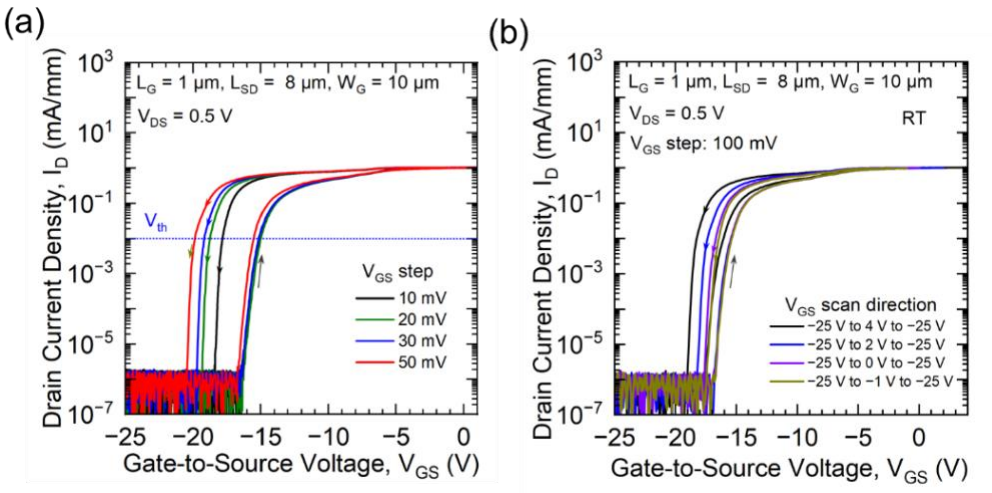


Figure 10.4: Transfer characteristics under various (a) V_{GS} steps at 10, 20, 30 and 50 mV, and (b) gate voltage poling paths with the maximum poling voltage $V_{GS,\,max}$ set at –1, 0, 2 and 4 V.

Figure 10.5(a) shows the variation of maximum I_D with temperature for different V_{DS}. The maximum I_D is defined at V_{GS} = 1 V. At 400°C, the device exhibited a significant enhancement in its current-carrying capacity, with I_D increasing by 3.75 times and 2.47 times compared to its RT values for V_{DS} = 1 and 5 V, respectively. The results also show a consistent increase in I_D with temperature, regardless of V_{DS}, indicating thermally activated carrier transport at elevated temperatures, possibly due to thermionic emission over the n^+-GaN/$Al_{0.50}Ga_{0.50}N$ hetero-barrier.[350] The gate leakage current density in the off-state increased to ~ 10^{-5} mA/mm at 400 °C, which is an order of magnitude higher than its RT value, shown in Figure 10.5(b). This increase in leakage current may be attributed to thermal excitation of carriers and enhanced tunneling effects at higher temperatures. Despite this, the device maintains its functional integrity in the on-state, demonstrating its potential for high-temperature applications.

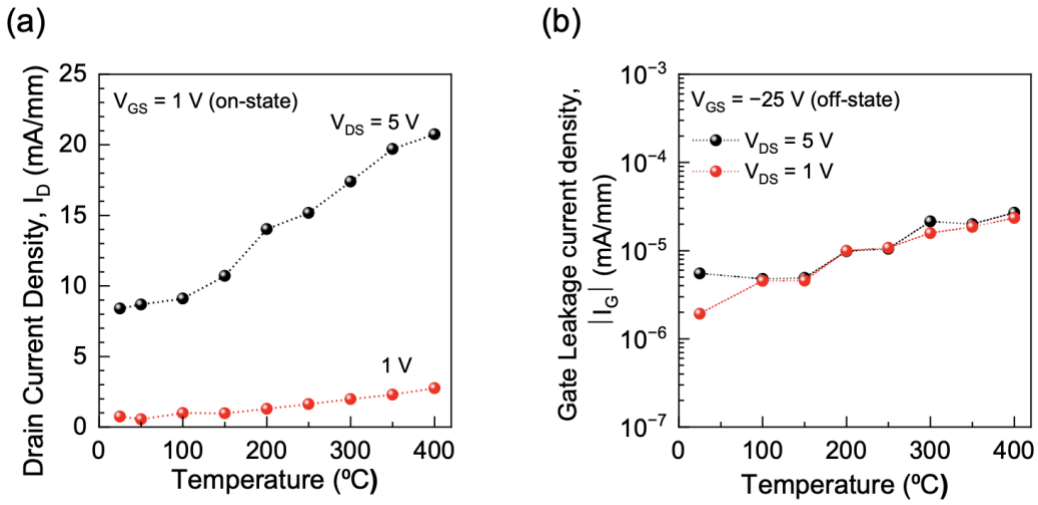


Figure 10.5: Variations of drain current (a) and gate leakage current (b) with temperature for different V_{DS}. Red and black curves correspond to measurements performed at V_{DS} = 1 and 5 V, respectively. The on- and off-states are defined for V_{GS} = 1 and −25 V, respectively.

10.4 Conclusion

In summary, we have demonstrated ferroelectric $Sc_{0.15}Al_{0.85}N/Al_{0.50}Ga_{0.50}N$ HEMTs through the integration of MBE-grown ScAlN barrier with MOCVD-grown AlGaN channel. The device exhibited a maximum I_D of ~16 mA/mm for V_{DS} = 10 V with a high I_{ON}/I_{OFF} of ~10^6. The transfer curve exhibited counterclockwise hysteresis, with a widely tunable V_{th} range of 6.4 V and a low *SS* of ~65 mV/dec at V_{DS} = 1 V. At 400°C, I_D increased 3.75× and 2.47× from RT at V_{DS} = 1 and 5 V, respectively, indicating thermally activated transport, probable driven by thermionic emission over the n^+-GaN/$Al_{0.50}Ga_{0.50}N$ hetero-barrier. The realization of ferroelectric ScAlN/AlGaN HEMTs open opportunities for the future reconfigurable multifunction transistors, memory, and high-temperature applications.

Chapter 11 Summary and Outlook

11.1 Summary

In summary, this dissertation investigates scandium-doped III-nitrides, with an emphasis on ScAlN, as an emerging ultrawide bandgap multifunctional material platform for advanced electronic and photonic devices. By leveraging molecular beam epitaxy, high quality ScAlN films and related heterostructures have been grown and realized with precise control over phase, composition, thickness and interface quality, providing a solid base for comprehensive studies of the enhanced ferroelectricity, second-order optical nonlinearity and polarization engineering that could be beneficial for next-generation photonic and electronic applications.

In terms of the photonics area, this dissertation demonstrates that the Sc incorporation can significantly enhance the second-order nonlinear optical susceptibility in both AlN and GaN lattices, while preserving a wide optical transparency window extending down to the UV range. A further demonstration of hybrid ScAlN/Si_3N_4 integrated photonics platform simultaneously achieved low optical loss and strong nonlinear functionality. The results show a promising pathway to further leverage Sc-rich ScAlN that shows stronger piezoelectric and optical nonlinear properties while minimizing the optical loss, especially at shorter wavelengths.

On the electronic device side, the strong spontaneous and piezoelectric polarization of ScAlN was exploited to achieve record-low sheet resistance in GaN-based heterostructures and high current density HEMTs with excellent thermal stability, which is critical for the next-generation RF applications. Furthermore, the ferroelectric behavior of ScAlN enabled novel device architecture, including high temperature nonvolatile memory and E-mode GaN HEMTs. Specifically, a fundamental study on the identification and protection of the native oxynitride layer in ScAlN thin films has been presented to improve the performance of ScAlN-based ferroelectric devices.

Overall, this dissertation establishes epitaxial ScAlN as a versatile, CMOS-compatible material that bridges photonics and electronics to expand the functionality of III-nitrides.

11.2 Future Works

Moving forward, several promising research directions can be further developed or investigated from this dissertation, as will be discussed in the following sections.

11.2.1 Sc-rich ScAlN Epitaxy with low loss

Enhancing the electro-optic coefficient of AlN by alloy engineering with scandium substitutional doping originates from the fact that Sc incorporation simultaneously softens the wurtzite lattice structure and induce more polarization anisotropy. Experimental and density-functional theory calculations demonstrated a nearly linear change in the electro-optic coefficient for r_{33} and r_{13} components with Sc incorporation up to ~30%. Beyond that, an exponential enhancement in both components occur and surpass $LiNbO_3$ when the Sc composition is close to the wurtzite/rock-salt crossover (~50%), shown in Figure 11.1(a).[170] However, the growth of phase-pure, high-Sc fraction ScAlN is challenging due to the thermodynamic phase competition between wurtzite AlN and cubic ScN. To further enhance the E-O coefficient, we target to develop Sc-rich ScAlN materials by MBE. To maintain the wurtzite phase of ScAlN near the crossover point for large E-O coefficients while reducing the loss, we will leverage the benefits of MBE growth in terms of precise flux control, wide growth temperature compatibility, ultra-high vacuum, doping flexibility and real-time feedback. Independent effusion cells control of Sc and Al provides the capability to fine tune the Sc incorporation and deposit the film in an atomic thickness precision. Combined with the real-time feedback provided by the reflection high-energy electron diffraction (RHEED), the phase information can be extracted during the epitaxial process and get connected with the growth parameters for further growth kinetics optimization. Meanwhile, the ultrahigh vacuum environment ($<10^{-9}$ Torr) can minimize the incorporation of oxygen and carbon contaminants that possibly form nucleation sites for unwanted cubic grains. Recent studies also take advantage of the doping flexibility of MBE to incorporate Ga as the surfactant in ScAlN to drastically reduce the oxygen and carbon impurity levels while lowering the surface energy to further inhibit the cubic phase formation, as shown in Figure 11.1(b).[122] Other group-III surfactants such as indium (In) will be investigated to further limit the impurity incorporation. These proposed strategies will push the wurtzite/rock-salt crossover point to the more Sc-rich end and the reduction in the impurity level can also reduce the absorption and scattering loss in the materials.

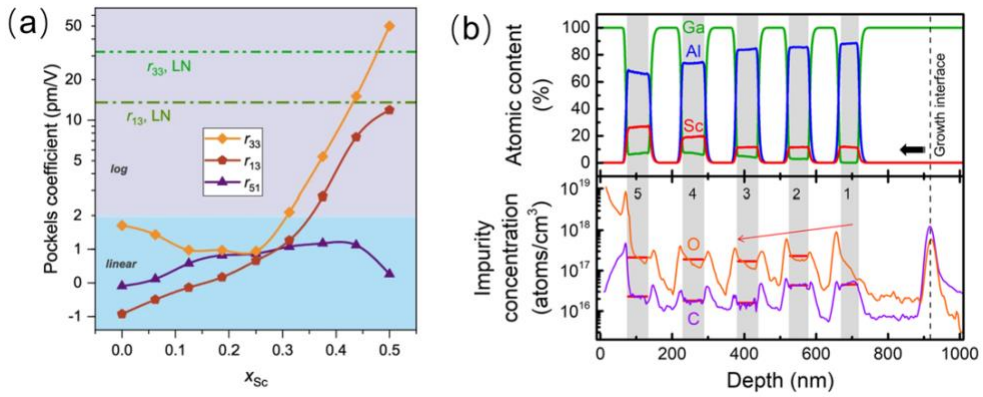


Figure 11.1: (a) DFT-calculated Pockels coefficients of ScAlN with various Sc contents. Notably r_{33} can potentially exceeds $LiNbO_3$ at high Sc alloying.[170] (b) SIMS profile of main elements Sc, Al, Ga and impurity elements O and C in the ScAlGaN/GaN multilayer stack, showing 3-4 orders of magnitude lower impurity incorporation than typical ScAlN grown on AlN.[122]

11.2.2 Novel Rare-earth Dopants to III-nitrides

Beyond Sc substitution, incorporating other rare-earth elements such as yttrium (Y) and lanthanum (La) offers another route to lower the ferroelectric switching barrier, improve the optical nonlinearity and enhance the E-O coefficients. The doping of Y and La is much less investigated compared to ScAlN due to the larger cation radii compared with Sc, posing additional challenges in single-crystalline YAlN and LaAlN growth. YAlN has been shown to be ferroelectric with Y doping even at 7% Y content.[58] However, the Y doping so far is achieved by evaporating Y by E-beam sources in these studies, limiting the vapor pressure achievable during the growth. In the next step, we will transition the Y doping from the E-beam source to the high-temperature effusion cell, which is currently used by ScAlN growths. This strategy provides more precise control on the composition and can achieve higher doping level in YAlN.

Lanthanum doping offers an even more intriguing route because the binary LaN thin film crystallizes in a wurtzite structure.[358] This structural characteristic fundamentally breaks the limit of rare-earth element doping levels, which are currently faced by ScAlN and YAlN. Since there is a clear trend in ScAlN that the E-O coefficient will increase with higher Sc content, it is possible with the much higher available La concentrations, a similar enhancement trend in E-O coefficients will be extended to LaAlN alloys.

11.2.3 Quantum Engineering in ScAlN

Through the construction of quantum structures, including quantum wells and digital alloys, the internal field can be strengthened by orders of magnitude higher. For example,

incorporating wide bandgap barriers such as AlN with other III-nitrides creates built-in polarization discontinuity and generate internal field on the order of MV/cm. Earlier work on MBE-epitaxial AlN/AlGaN quantum wells has been identified to have >40 pm/V r_{33} coefficient, surpassing GaN, AlN and $LiNbO_3$ while maintaining the cut-off wavelength at the UV range.[166] By leveraging the enhanced E-O efficient in ScAlN, building quantum well structures with ScAlN barrier are expected to further boost the conversion efficiency.

Alternatively, building digital alloys of $(ScN)_m/(AlN)_n$ and $(YN)_m/(AlN)_n$ can effectively achieve much higher Sc content since the lattice avoids the long-range rock-salt ordering, which is faced by bulk ScAlN materials. The extremely short periodicity also introduces polarization discontinuity at the interface which can generate a large internal field as discussed above. Preliminary DFT calculations show that when building *a*-plane $(ScN)_m/(AlN)_n$ digital alloys, both clamped and piezoelectric contributions of r_{33} have an abrupt increase above 25% Sc incorporation and can reach >40 pm/V E-O coefficients at equivalent 50% Sc incorporation.[124]

11.2.4 Improved Device Performance of ScAlN/GaN HEMTs

Extensive studies have shown that fin-structured and nanowire HEMTs have emerged as the next generation power devices compared to planar GaN HEMTs, especially for the small footprint nodes. Such structures improve the device linearity and enable E-mode operation through enhanced gate control, which provides another novel pathway for normally-off HEMTs.[359, 360]

In this thesis, we have shown the superior device performance enabled by ScAlN and we hope to extend the benefits of ScAlN barrier HEMTs further to achieve higher current density and enhanced threshold tunability. Furthermore, device reliability may be improved with better thermal management and reduced peak electric field. The success of this work would position 3D-structured ScAlN barrier HEMTs as a scalable platform for high power RF applications with improved efficiency, extending the GaN platform into the next technology node.

11.2.5 Contact Resistance Reduction by Contact Engineering in AlGaN-channel HEMTs

High contact resistance remains as a major challenge in realizing high current AlGaN-channel HEMTs. This possibly comes from two aspects: The first limitation is by the AlGaN-channel structure. Due to the limited band discontinuity in Al-rich AlGaN heterostructures, the generated 2DEG density is limited. In the meantime, Al-rich AlGaN channel has lower mobility

limited by the alloy scattering in both barrier and channel layers. This leads to high sheet resistance and leads to worse contact with the regrown contact layers.

In the next step, we will address the above-mentioned issues in two parallel aspects. First, we will optimize the heterostructure of AlGaN-channel HEMT to reduce its sheet resistance. This will be achieved by epitaxial optimization and structural engineering. Presented AlGaN-channel devices were built on MOCVD-grown AlN/AlGaN on sapphire substrate, which tends to form a high density of dislocations and defects. Moving the growth on single crystalline bulk AlN substrate will reduce the defect densities by orders of magnitude, potentially improve the mobility by reducing scatterings. Furthermore, from the structure point of view, ScAlN, which has a larger conduction band offset with AlN and GaN, can be integrated to create higher 2DEG densities. An interlayer of AlN can also be introduced to compensate the alloy scattering to further improve the mobility. Bandgap engineering strategy including graded n^+-AlGaN contact will also be investigated in parallel. If the current density of AlGaN-channel HEMT can reach a level on par with the GaN-channel devices, with the higher breakdown field, the AlGaN-based devices are expected to push the boundary of operation voltages and frequencies.

Bibliography

1. Song, Y., et al., *III-nitride-based monolithic integration: From electronics to photonics.* Applied Physics Reviews, 2025. **12**(2).
2. Palacios, T., et al., *High-power AlGaN/GaN HEMTs for Ka-band applications.* IEEE Electron Device Letters, 2005. **26**(11): p. 781-783.
3. Hardy, M.T., et al., *Group III-nitride lasers: a materials perspective.* Materials Today, 2011. **14**(9): p. 408-415.
4. Mishra, U.K., P. Parikh, and W. Yi-Feng, *AlGaN/GaN HEMTs-an overview of device operation and applications.* Proceedings of the IEEE, 2002. **90**(6): p. 1022-1031.
5. Nakamura, S., *III–V nitride based light-emitting devices.* Solid State Communications, 1997. **102**(2): p. 237-248.
6. Walukiewicz, W., et al., *Optical properties and electronic structure of InN and In-rich group III-nitride alloys.* Journal of Crystal Growth, 2004. **269**(1): p. 119-127.
7. Feneberg, M., et al., *High-excitation and high-resolution photoluminescence spectra of bulk AlN.* Physical Review B, 2010. **82**(7): p. 075208.
8. Piprek, J., *Nitride semiconductor devices: principles and simulation*. 2007: John Wiley & Sons.
9. Coughlan, C., et al., *Band gap bowing and optical polarization switching in $Al_{1-x}Ga_xN$ alloys.* physica status solidi (b), 2015. **252**(5): p. 879-884.
10. Ferhat, M. and F. Bechstedt, *First-principles calculations of gap bowing in $In_xGa_{1-x}N$ and $In_xAl_{1-x}N$ alloys: relation to structural and thermodynamic properties.* Physical Review B, 2002. **65**(7): p. 075213.
11. Zhang, J.-M., D.-D. Wang, and K.-W. Xu, *Calculation of the surface energy of hcp metals by using the modified embedded atom method.* Applied Surface Science, 2006. **253**(4): p. 2018-2024.
12. Andiwijayakusuma, D., M. Saito, and A. Purqon, *Density functional theory study : Electronic structures of RE:GaN in wurtzite $Ga_{15}RE_1N_{16}$.* Journal of Physics: Conference Series, 2016. **739**(1): p. 012027.
13. Bagayoko, D. and L. Franklin, *Density-functional theory band gap of wurtzite InN.* Journal of Applied Physics, 2005. **97**(12).
14. Schulz, H. and K.H. Thiemann, *Crystal structure refinement of AlN and GaN.* Solid State Communications, 1977. **23**(11): p. 815-819.
15. Zoroddu, A., et al., *First-principles prediction of structure, energetics, formation enthalpy, elastic constants, polarization, and piezoelectric constants of AlN, GaN, and InN: Comparison of local and gradient-corrected density-functional theory.* Physical Review B, 2001. **64**(4): p. 045208.
16. Akiyama, M., et al., *Enhancement of Piezoelectric Response in Scandium Aluminum Nitride Alloy Thin Films Prepared by Dual Reactive Cosputtering.* Advanced Materials, 2009. **21**(5): p. 593-596.

17. Umeda, K., et al. *Piezoelectric properties of ScAlN thin films for piezo-MEMS devices*. in *2013 IEEE 26th International Conference on Micro Electro Mechanical Systems (MEMS)*. 2013.
18. Zheng, Y., et al. *High-Order Sezawa Mode AlScN/GaN/Sapphire Surface Acoustic Wave Resonators*. in *2022 IEEE 35th International Conference on Micro Electro Mechanical Systems Conference (MEMS)*. 2022.
19. Peng, W., et al. *A 56 GHz Trilayer AlN/ScAlN/AlN Periodically Poled FBAR*. in *2024 IEEE/MTT-S International Microwave Symposium - IMS 2024*. 2024.
20. Park, M., et al., *A 19 GHz All-Epitaxial $Al_{0.8}Sc_{0.2}N$ Cascaded FBAR for RF Filtering Applications.* IEEE Electron Device Letters, 2024. **45**(7): p. 1341-1344.
21. Fichtner, S., et al., *AlScN: A III-V semiconductor based ferroelectric.* Journal of Applied Physics, 2019. **125**(11).
22. Wang, P., et al., *Fully epitaxial ferroelectric ScAlN grown by molecular beam epitaxy.* Applied Physics Letters, 2021. **118**(22).
23. Liu, J., et al. *Second-order optical nonlinearities in ferroelectric ScAlN for quantum photonics*. in *2023 IEEE Photonics Conference (IPC)*. 2023.
24. Eshita, T., T. Tamura, and Y. Arimoto, *Ferroelectric random access memory (FRAM) devices*, in *Advances in Non-volatile Memory and Storage Technology*, Y. Nishi, Editor. 2014, Woodhead Publishing. p. 434-454.
25. Scott, J.F. and C.A. Paz de Araujo, *Ferroelectric Memories.* Science, 1989. **246**(4936): p. 1400-1405.
26. Chandra, P. and P.B. Littlewood, *A Landau Primer for Ferroelectrics*, in *Physics of Ferroelectrics: A Modern Perspective*. 2007, Springer Berlin Heidelberg: Berlin, Heidelberg. p. 69-116.
27. Piazza, G., et al., *Piezoelectric aluminum nitride thin films for microelectromechanical systems.* MRS Bulletin, 2012. **37**(11): p. 1051-1061.
28. Zhu, W., et al., *Strongly temperature dependent ferroelectric switching in AlN, $Al_{1-x}Sc_xN$, and $Al_{1-x}B_xN$ thin films.* Applied Physics Letters, 2021. **119**(6).
29. Hasegawa, K., et al., *Full polarization reversal at room temperature in unsubstituted AlN.* Applied Physics Letters, 2023. **123**(19).
30. Gogi, V.K., et al., *Understanding ferroelectricity in sputtered aluminum nitride thin films on silicon.* APL Materials, 2025. **13**(5).
31. Tasnádi, F., et al., *Origin of the Anomalous Piezoelectric Response in Wurtzite $Sc_xAl_{1-x}N$ Alloys.* Physical Review Letters, 2010. **104**(13): p. 137601.
32. Motoki, K., et al., *Improved crystallographic order of ScAlN/GaN heterostructures grown at low temperatures under metal rich surface conditions.* Journal of Applied Physics, 2024. **135**(13).
33. Wang, H., et al., *Piezoelectric effect and polarization switching in $Al_{1-x}Sc_xN$.* Journal of Applied Physics, 2021. **130**(10).
34. Kobayashi, A., et al., *Sputter Epitaxy of Transition Metal Nitrides: Advances in Superconductors, Semiconductors, and Ferroelectrics.* physica status solidi (a), 2025. **222**(17): p. 2400896.
35. Wang, P., et al., *Molecular beam epitaxy and characterization of wurtzite $Sc_xAl_{1-x}N$.* Applied Physics Letters, 2020. **116**(15).
36. Leone, S., et al., *Metal-Organic Chemical Vapor Deposition of Aluminum Scandium Nitride.* physica status solidi (RRL) – Rapid Research Letters, 2020. **14**(1): p. 1900535.

37. Nguyen, T.-S., et al., *Lattice-matched multiple channel AlScN/GaN heterostructures.* APL Materials, 2024. **12**(10).
38. Gaddam, V., et al., *Aluminum Scandium Nitride as a Functional Material at 1000 °C.* Advanced Electronic Materials, 2025. **11**(6): p. 2400849.
39. Pradhan, D.K., et al., *Materials for high-temperature digital electronics.* Nature Reviews Materials, 2024. **9**(11): p. 790-807.
40. Jiang, Y., et al., *Enabling ultra-low-voltage switching in $BaTiO_3$.* Nature Materials, 2022. **21**(7): p. 779-785.
41. Schroeder, U., et al., *The fundamentals and applications of ferroelectric HfO_2.* Nature Reviews Materials, 2022. **7**(8): p. 653-669.
42. Li, Y.-C., et al., *Domain Switching Characteristics in Ga-Doped HfO_2 Ferroelectric Thin Films with Low Coercive Field.* Nano Letters, 2024. **24**(22): p. 6585-6591.
43. Rath, M., et al., *A comparative study on macroscopic and nanoscale polarization mapping on large area PLD grown PZT thin films.* Ceramics International, 2018. **44**(8): p. 8749-8755.
44. Liu, X., A.W. Bruch, and H.X. Tang, *Aluminum nitride photonic integrated circuits: from piezo-optomechanics to nonlinear optics.* Advances in Optics and Photonics, 2023. **15**(1): p. 236-317.
45. Li, N., et al., *Aluminium nitride integrated photonics: a review.* Nanophotonics, 2021. **10**(9): p. 2347-2387.
46. Xiong, C., W.H.P. Pernice, and H.X. Tang, *Low-Loss, Silicon Integrated, Aluminum Nitride Photonic Circuits and Their Use for Electro-Optic Signal Processing.* Nano Letters, 2012. **12**(7): p. 3562-3568.
47. Liu, X., et al., *Aluminum nitride nanophotonics for beyond-octave soliton microcomb generation and self-referencing.* Nature Communications, 2021. **12**(1): p. 5428.
48. Pernice, W.H.P., et al., *Second harmonic generation in phase matched aluminum nitride waveguides and micro-ring resonators.* Applied Physics Letters, 2012. **100**(22).
49. Huang, W., et al., *Acousto-Optic Modulation on Silicon-Aluminum Nitride Hybrid-Integrated Platform for Cryogenic Applications.* Nano Letters, 2025. **25**(13): p. 5117-5123.
50. Boyd, R.W., *Nonlinear optics*. 2020, San Diego, CA: Academic Press. 636.
51. Majkić, A., et al., *Optical nonlinear and electro-optical coefficients in bulk aluminium nitride single crystals.* physica status solidi (b), 2017. **254**(9): p. 1700077.
52. Bruch, A.W., et al., *17 000%/W second-harmonic conversion efficiency in single-crystalline aluminum nitride microresonators.* Applied Physics Letters, 2018. **113**(13).
53. Choy, M.M. and R.L. Byer, *Accurate second-order susceptibility measurements of visible and infrared nonlinear crystals.* Physical Review B, 1976. **14**(4): p. 1693-1706.
54. Levine, B.F., *Bond-Charge Calculation of Nonlinear Optical Susceptibilities for Various Crystal Structures.* Physical Review B, 1973. **7**(6): p. 2600-2626.
55. Suceava, A., et al., *Enhancement of second-order optical nonlinearities and nanoscale periodic domain patterning in ferroelectric boron-substituted aluminum nitride thin films.* Optical Materials Express, 2023. **13**(6): p. 1522-1534.
56. Yoshioka, V., et al., *Strongly enhanced second-order optical nonlinearity in CMOS-compatible $Al_{1-x}Sc_xN$ thin films.* APL Materials, 2021. **9**(10).
57. Qin, H., et al., *Perspectives of Ferroelectric Wurtzite AlScN: Material Characteristics, Preparation, and Applications in Advanced Memory Devices.* Nanomaterials, 2024. **14**(11): p. 986.

58. Wang, D., et al., *Ferroelectric YAlN grown by molecular beam epitaxy.* Applied Physics Letters, 2023. **123**(3).
59. Wang, P., et al., *Dawn of nitride ferroelectric semiconductors: from materials to devices.* Semiconductor Science and Technology, 2023. **38**(4): p. 043002.
60. Yang, S., et al., *Molecular beam epitaxy and characterization of ferroelectric quaternary alloy $Sc_{0.2}Al_{0.45}Ga_{0.35}N$.* Applied Physics Letters, 2024. **124**(19).
61. Wang, D., et al., *Fully epitaxial ferroelectric ScGaN grown on GaN by molecular beam epitaxy.* Applied Physics Letters, 2021. **119**(11).
62. Zheng, J.X., et al., *Electrical breakdown strength enhancement in aluminum scandium nitride through a compositionally modulated periodic multilayer structure.* Journal of Applied Physics, 2021. **130**(14).
63. Wang, D., et al., *Electric-field-induced domain walls in wurtzite ferroelectrics.* Nature, 2025. **641**(8061): p. 76-82.
64. Wang, D., et al., *Band alignment and charge carrier transport properties of YAlN/III-nitride heterostructures.* Applied Surface Science, 2023. **637**: p. 157893.
65. Wang, D., et al., *An Epitaxial Ferroelectric ScAlN/GaN Heterostructure Memory.* Advanced Electronic Materials, 2022. **8**(9): p. 2200005.
66. Wang, P., et al., *Ferroelectric N-polar ScAlN/GaN heterostructures grown by molecular beam epitaxy.* Applied Physics Letters, 2022. **121**(2).
67. Fichtner, S., et al. *Ferroelectricity in AlScN: Switching, Imprint and sub-150 nm Films*. in *2020 Joint Conference of the IEEE International Frequency Control Symposium and International Symposium on Applications of Ferroelectrics (IFCS-ISAF)*. 2020.
68. Wang, D., et al., *Rethinking polarization in wurtzite semiconductors.* Applied Physics Letters, 2024. **124**(26).
69. Ye, H., et al., *Experimental determination of giant polarization in wurtzite III-nitride semiconductors.* Nature Communications, 2025. **16**(1): p. 3863.
70. Wang, P., et al., *Ferroelectric Nitride Heterostructures on CMOS Compatible Molybdenum for Synaptic Memristors.* ACS Applied Materials & Interfaces, 2023. **15**(14): p. 18022-18031.
71. Wang, D., et al., *Sub-Microsecond Polarization Switching in (Al,Sc)N Ferroelectric Capacitors Grown on Complementary Metal–Oxide–Semiconductor-Compatible Aluminum Electrodes.* physica status solidi (RRL) – Rapid Research Letters, 2021. **15**(5): p. 2000575.
72. Wang, D., et al., *Perspectives on nitride ferroelectric semiconductors: Challenges and opportunities.* Applied Physics Letters, 2024. **124**(15).
73. Ryoo, S.K., et al., *Fabrication of Ultrathin Ferroelectric $Al_{0.7}Sc_{0.3}N$ Films under Complementary-Metal-Oxide-Semiconductor Compatible Conditions by using $HfN_{0.4}$ Electrode.* Advanced Materials, 2025. **37**(1): p. 2413295.
74. Wang, D., et al., *Ultrathin Nitride Ferroic Memory with Large ON/OFF Ratios for Analog In-Memory Computing.* Advanced Materials, 2023. **35**(20): p. 2210628.
75. Wang, D., et al., *Thickness scaling down to 5 nm of ferroelectric ScAlN on CMOS compatible molybdenum grown by molecular beam epitaxy.* Applied Physics Letters, 2023. **122**(5).
76. Wang, D., et al., *Controlled ferroelectric switching in ultrawide bandgap AlN/ScAlN multilayers.* Applied Physics Letters, 2023. **123**(10).

77. Giribaldi, G., et al. *Compensation of Contact Nature-Dependent Asymmetry in The Leakage Current of Ferroelectric $Sc_xAl_{1-x}N$ Thin-Film Capacitors*. in *2021 IEEE 34th International Conference on Micro Electro Mechanical Systems (MEMS)*. 2021.
78. Li, M., et al., *Oxide overlayer formation on sputtered ScAlN film exposed to air.* Applied Physics Letters, 2022. **121**(11).
79. Wang, D., et al., *Ferroelectric Switching in Sub-20 nm Aluminum Scandium Nitride Thin Films.* IEEE Electron Device Letters, 2020. **41**(12): p. 1774-1777.
80. Wang, R., et al., *Enhancing Reliability in Ferroelectric ScAlN Non-Volatile Memory With AlO_x Layer Insertion.* IEEE Electron Device Letters, 2025. **46**(7): p. 1107-1110.
81. Wang, D., et al., *On the surface oxidation and band alignment of ferroelectric $Sc_{0.18}Al_{0.82}N$/GaN heterostructures.* Applied Surface Science, 2023. **628**: p. 157337.
82. Kim, K.-H., et al., *Multistate, Ultrathin, Back-End-of-Line-Compatible AlScN Ferroelectric Diodes.* ACS Nano, 2024. **18**(24): p. 15925-15934.
83. Liu, X., et al., *Aluminum scandium nitride-based metal–ferroelectric–metal diode memory devices with high on/off ratios.* Applied Physics Letters, 2021. **118**(20).
84. Chang, J.-H., et al., *Effect of capping layer on the ferroelectricity of hafnium oxide.* Thin Solid Films, 2022. **753**: p. 139274.
85. Shifat, A.S.M.Z., et al., *Vertical Etching of Scandium Aluminum Nitride Thin Films Using TMAH Solution.* Nanomaterials, 2023. **13**(2): p. 274.
86. Yazawa, K., et al., *Low leakage current in heteroepitaxial $Al_{0.7}Sc_{0.3}N$ ferroelectric films on GaN.* Physical Review Applied, 2025. **23**(1): p. 014036.
87. Casamento, J., et al., *Epitaxial $Sc_xAl_{1-x}N$ on GaN exhibits attractive high-K dielectric properties.* Applied Physics Letters, 2022. **120**(15).
88. Akiyama, M., et al., *Influence of scandium concentration on power generation figure of merit of scandium aluminum nitride thin films.* Applied Physics Letters, 2013. **102**(2).
89. Hu, Z., et al., *Demonstration of Highly Scaled AlScN Ferroelectric Diode Memory with a Storage Density of >100 Mbit/mm^2.* Nano Letters, 2025. **25**(37): p. 13748-13755.
90. Liu, C., et al. *Multiscale Modeling of $Al_{0.7}Sc_{0.3}N$-based FeRAM: the Steep Switching, Leakage and Selector-free Array*. in *2021 IEEE International Electron Devices Meeting (IEDM)*. 2021.
91. Zhang, H., E.J. Miller, and E.T. Yu, *Analysis of leakage current mechanisms in Schottky contacts to GaN and $Al_{0.25}Ga_{0.75}N$/GaN grown by molecular-beam epitaxy.* Journal of Applied Physics, 2006. **99**(2).
92. Wang, D., et al., *Impact of dislocation density on the ferroelectric properties of ScAlN grown by molecular beam epitaxy.* Applied Physics Letters, 2022. **121**(4).
93. Pai, S., et al., *Experimentally realized in situ backpropagation for deep learning in photonic neural networks.* Science, 2023. **380**(6643): p. 398-404.
94. Alexander, K., et al., *A manufacturable platform for photonic quantum computing.* Nature, 2025. **641**(8064): p. 876-883.
95. Jia, X., et al., *Continuous-variable multipartite entanglement in an integrated microcomb.* Nature, 2025. **639**(8054): p. 329-336.
96. McKenna, T.P., et al., *Ultra-low-power second-order nonlinear optics on a chip.* Nature Communications, 2022. **13**(1): p. 4532.
97. Bruch, A.W., et al., *On-chip $\chi^{(2)}$ microring optical parametric oscillator.* Optica, 2019. **6**(10): p. 1361-1366.

98. Chai, Z., et al., *Ultrafast All-Optical Switching.* Advanced Optical Materials, 2017. **5**(7): p. 1600665.
99. Cong, K., et al., *Quantum-Memory-Enabled Ultrafast Optical Switching in Carbon Nanotubes.* ACS Photonics, 2020. **7**(6): p. 1382-1387.
100. Wang, X., et al., *Quantum frequency conversion and single-photon detection with lithium niobate nanophotonic chips.* npj Quantum Information, 2023. **9**(1): p. 38.
101. Lu, J., et al., *Periodically poled thin-film lithium niobate microring resonators with a second-harmonic generation efficiency of 250,000%/W.* Optica, 2019. **6**(12): p. 1455-1460.
102. Moody, G., et al., *Chip-scale nonlinear photonics for quantum light generation.* AVS Quantum Science, 2020. **2**(4).
103. Bosshard, C., et al., *Kerr Nonlinearity via Cascaded Optical Rectification and the Linear Electro-optic Effect.* Physical Review Letters, 1995. **74**(14): p. 2816-2819.
104. Boes, A., et al., *Lithium niobate photonics: Unlocking the electromagnetic spectrum.* Science, 2023. **379**(6627): p. eabj4396.
105. Shoji, I., et al., *Absolute scale of second-order nonlinear-optical coefficients.* Journal of the Optical Society of America B, 1997. **14**(9): p. 2268-2294.
106. Tan, Y., et al., *Micro-transfer Printed Thin Film Lithium Niobate (TFLN)-on-Silicon Ring Modulator.* ACS Photonics, 2024. **11**(5): p. 1920-1927.
107. Majkić, A., et al., *Optical properties of aluminum nitride single crystals in the THz region.* Optical Materials Express, 2015. **5**(10): p. 2106-2111.
108. Gromovyi, M., et al., *Low-loss GaN-on-insulator platform for integrated photonics.* Optics Express, 2022. **30**(12): p. 20737-20749.
109. Ashkin, A., et al., *Optically-Induced Refractive Index Inhomogeneities in $LiNbO_3$ and $LiTaO_3$.* Applied Physics Letters, 1966. **9**(1): p. 72-74.
110. Wang, S., et al., *CMOS-compatible photonic integrated circuits on thin-film ScAlN.* APL Photonics, 2024. **9**(6).
111. Schuster, J.C. and J. Bauer, *The ternary systems ScAlN and YAlN.* Journal of the Less Common Metals, 1985. **109**(2): p. 345-350.
112. Bethune, D.S., *Optical harmonic generation and mixing in multilayer media: extension of optical transfer matrix approach to include anisotropic materials.* Journal of the Optical Society of America B, 1991. **8**(2): p. 367-373.
113. Kang, D., A. Anirban, and A.S. Helmy, *Monolithic semiconductor chips as a source for broadband wavelength-multiplexed polarization entangled photons.* Optics Express, 2016. **24**(13): p. 15160-15170.
114. Zhang, X., et al., *Polarization-entangled photon pairs generation from a single lithium niobate waveguide with single poling period.* Optics Express, 2025. **33**(12): p. 24193-24203.
115. Örsel, O.E. and G. Bahl, *Electro-optic non-reciprocal polarization rotation in lithium niobate.* APL Photonics, 2023. **8**(9).
116. Boes, A., et al., *Status and Potential of Lithium Niobate on Insulator (LNOI) for Photonic Integrated Circuits.* Laser & Photonics Reviews, 2018. **12**(4): p. 1700256.
117. Alferness, R.C., *Efficient waveguide electro-optic TE⇄TM mode converter/wavelength filter.* Applied Physics Letters, 1980. **36**(7): p. 513-515.
118. Chen, J.-Y., et al., *Modal phase matched lithium niobate nanocircuits for integrated nonlinear photonics.* OSA Continuum, 2018. **1**(1): p. 229-242.

119. Yan, Z., et al., *An Optical Parametric Amplifier via $\chi^{(2)}$ in AlGaAs Waveguides.* Journal of Lightwave Technology, 2022. **40**(17): p. 5943-5951.
120. Akin, J., et al., *InGaP $\chi^{(2)}$ integrated photonics platform for broadband, ultra-efficient nonlinear conversion and entangled photon generation.* Light: Science & Applications, 2024. **13**(1): p. 290.
121. Briggs, I., et al., *Simultaneous type-I and type-II phase matching for second-order nonlinearity in integrated lithium niobate waveguide.* Optics Express, 2021. **29**(16): p. 26183-26190.
122. Wang, P., et al., *Quaternary alloy ScAlGaN: A promising strategy to improve the quality of ScAlN.* Applied Physics Letters, 2022. **120**(1).
123. Zhang, S., et al., *Tunable optoelectronic and ferroelectric properties in Sc-based III-nitrides.* Journal of Applied Physics, 2013. **114**(13).
124. Wang, H., S. Mu, and C.G. Van de Walle, *Towards higher electro-optic response in AlScN.* Applied Physics Letters, 2025. **126**(4).
125. Liu, J., Y. Bai, and G. Xiong, *Studies of the second-order nonlinear optical susceptibilities of GaN/AlGaN quantum well.* Physica E: Low-dimensional Systems and Nanostructures, 2004. **23**(1): p. 70-74.
126. Dmitriev, V.A., et al., *Electric breakdown in GaN p-n junctions.* Applied Physics Letters, 1996. **68**(2): p. 229-231.
127. Pearton, S.J., et al., *GaN electronics for high power, high temperature applications.* Materials Science and Engineering: B, 2001. **82**(1): p. 227-231.
128. Sequeira, M.C., et al., *Unravelling the secrets of the resistance of GaN to strongly ionising radiation.* Communications Physics, 2021. **4**(1): p. 51.
129. Jia, H., et al., *Recent Progress in GaN-Based Light-Emitting Diodes.* Advanced Materials, 2009. **21**(45): p. 4641-4646.
130. Vico Triviño, N., et al., *Integrated photonics on silicon with wide bandgap GaN semiconductor.* Applied Physics Letters, 2013. **102**(8).
131. Zeng, H., et al., *Quantum Light Generation Based on GaN Microring toward Fully On-Chip Source.* Physical Review Letters, 2024. **132**(13): p. 133603.
132. Kheirodin, N., et al., *Electrooptical Modulator at Telecommunication Wavelengths Based on GaN–AlN Coupled Quantum Wells.* IEEE Photonics Technology Letters, 2008. **20**(9): p. 724-726.
133. Yu, Z.J., et al., *The growth and characterization of GaN on sapphire and silicon.* Journal of Electronic Materials, 1992. **21**(3): p. 383-387.
134. Melton, W.A. and J.I. Pankove, *GaN growth on sapphire.* Journal of Crystal Growth, 1997. **178**(1): p. 168-173.
135. Dmitriev, V., et al., *Growth and characterization of GaN layers on SiC substrates.* Journal of Crystal Growth, 1996. **166**(1): p. 601-606.
136. Ploog, K.H., et al., *Nucleation and growth of GaN layers on GaAs, Si, and SiC substrates.* Journal of Vacuum Science & Technology B: Microelectronics and Nanometer Structures Processing, Measurement, and Phenomena, 1998. **16**(4): p. 2229-2236.
137. Sanford, N.A., et al., *Measurement of second order susceptibilities of GaN and AlGaN.* Journal of Applied Physics, 2005. **97**(5).
138. Uehara, M., et al., *Lower ferroelectric coercive field of ScGaN with equivalent remanent polarization as ScAlN.* Applied Physics Express, 2022. **15**(8): p. 081003.

139. Yang, S., et al., *Sc-rich monocrystalline ScGaN grown by MBE exhibits attractive ferroelectric properties.* Applied Physics Letters, 2025. **127**(2).
140. Fathabadi, M., et al., *Molecular beam epitaxy growth and characterization of ScGaN epilayers.* Journal of Vacuum Science & Technology A, 2024. **42**(5).
141. Tsui, H.C.L., et al., *Band gaps of wurtzite $Sc_xGa_{1-x}N$ alloys.* Applied Physics Letters, 2015. **106**(13).
142. Tsui, H.C.L., *Characterisation of scandium-based III-nitride thin films*. 2016, Imperial College London.
143. Helkey, R., et al., *High-Performance Photonic Integrated Circuits on Silicon.* IEEE Journal of Selected Topics in Quantum Electronics, 2019. **25**(5): p. 1-15.
144. Su, Y., et al., *Scalability of Large-Scale Photonic Integrated Circuits.* ACS Photonics, 2023. **10**(7): p. 2020-2030.
145. Liao, K., et al., *Integrated Photonic Neural Networks: Opportunities and Challenges.* ACS Photonics, 2023. **10**(7): p. 2001-2010.
146. Moss, D.J., et al., *New CMOS-compatible platforms based on silicon nitride and Hydex for nonlinear optics.* Nature Photonics, 2013. **7**(8): p. 597-607.
147. Xiang, C., W. Jin, and J.E. Bowers, *Silicon nitride passive and active photonic integrated circuits: trends and prospects.* Photonics Research, 2022. **10**(6): p. A82-A96.
148. Puckett, M.W., et al., *422 Million intrinsic quality factor planar integrated all-waveguide resonator with sub-MHz linewidth.* Nature Communications, 2021. **12**(1): p. 934.
149. Ji, X., et al., *Methods to achieve ultra-high quality factor silicon nitride resonators.* APL Photonics, 2021. **6**(7).
150. Xiang, C., et al., *High-performance lasers for fully integrated silicon nitride photonics.* Nature Communications, 2021. **12**(1): p. 6650.
151. Jin, W., et al., *Hertz-linewidth semiconductor lasers using CMOS-ready ultra-high-Q microresonators.* Nature Photonics, 2021. **15**(5): p. 346-353.
152. Barwicz, T., et al., *Microring-resonator-based add-drop filters in SiN: fabrication and analysis.* Optics Express, 2004. **12**(7): p. 1437-1442.
153. Bryan, M.R., et al., *Biosensing with Silicon Nitride Microring Resonators Integrated with an On-Chip Filter Bank Spectrometer.* ACS Sensors, 2023. **8**(2): p. 739-747.
154. Girardi, M., et al., *Superefficient microcombs at the wafer level.* Optics Express, 2025. **33**(13): p. 27451-27460.
155. Shen, B., et al., *Integrated turnkey soliton microcombs.* Nature, 2020. **582**(7812): p. 365-369.
156. Wang, C., et al., *Integrated lithium niobate electro-optic modulators operating at CMOS-compatible voltages.* Nature, 2018. **562**(7725): p. 101-104.
157. Li, M., et al., *Lithium niobate photonic-crystal electro-optic modulator.* Nature Communications, 2020. **11**(1): p. 4123.
158. Meng, X., et al., *Thin-Film Lithium Niobate Modulators with Ultra-High Modulation Efficiency.* Laser & Photonics Reviews, 2025. **19**(1): p. 2400809.
159. Zhang, M., et al., *Integrated lithium niobate electro-optic modulators: when performance meets scalability.* Optica, 2021. **8**(5): p. 652-667.
160. Du, H., et al., *High-efficiency second harmonic generation in a micro-resonator on dual-layered lithium niobate.* Optics Letters, 2024. **49**(2): p. 391-394.
161. Qu, L., et al., *Second Harmonic Generation in Lithium Niobate on Insulator.* Laser & Photonics Reviews, 2025. **19**(11): p. 2401928.

162. Lu, J., et al., *Ultralow-threshold thin-film lithium niobate optical parametric oscillator.* Optica, 2021. **8**(4): p. 539-544.
163. Peng, Y., et al., *Efficient optical parametric amplification in the thin film lithium niobate waveguides.* Scientific Reports, 2025. **15**(1): p. 2851.
164. Vazimali, M.G. and S. Fathpour, *Applications of thin-film lithium niobate in nonlinear integrated photonics.* Adv. Photonics, 2022. **4**(03).
165. Doolittle, W.A., et al., *Prospectives for AlN electronics and optoelectronics and the important role of alternative synthesis.* Applied Physics Letters, 2023. **123**(7).
166. Shin, W.J., et al., *Enhanced Pockels Effect in AlN Microring Resonator Modulators Based on AlGaN/AlN Multiple Quantum Wells.* ACS Photonics, 2023. **10**(1): p. 34-42.
167. Sun, Y., et al., *Ultrahigh Q microring resonators using a single-crystal aluminum-nitride-on-sapphire platform.* Optics Letters, 2019. **44**(23): p. 5679-5682.
168. Moram, M.A. and S. Zhang, *ScGaN and ScAlN: emerging nitride materials.* Journal of Materials Chemistry A, 2014. **2**(17): p. 6042-6050.
169. Mondal, S., et al., *Unprecedented enhancement of piezoelectricity of wurtzite nitride semiconductors via thermal annealing.* Nature Communications, 2025. **16**(1): p. 4130.
170. Yang, G., et al., *Unveiling the Pockels coefficient of ferroelectric nitride ScAlN.* Nature Communications, 2024. **15**(1): p. 9538.
171. Zhu, S., et al. *Integrated ScAlN Photonic Circuits on Silicon Substrate*. in *Conference on Lasers and Electro-Optics*. 2020. Washington, DC: Optica Publishing Group.
172. Liu, S., et al., *Fabrication of Ultra-Low-Loss, Dispersion-Engineered Silicon Nitride Photonic Integrated Circuits via Silicon Hardmask Etching.* ACS Photonics, 2025. **12**(2): p. 1039-1046.
173. Pfeiffer, M.H.P., et al., *Ultra-smooth silicon nitride waveguides based on the Damascene reflow process: fabrication and loss origins.* Optica, 2018. **5**(7): p. 884-892.
174. Ji, X., et al., *Compact, spatial-mode-interaction-free, ultralow-loss, nonlinear photonic integrated circuits.* Communications Physics, 2022. **5**(1): p. 84.
175. Zhang, L., et al., *Ultrahigh-Q silicon racetrack resonators.* Photonics Research, 2020. **8**(5): p. 684-689.
176. Dumon, P., et al., *Low-loss SOI photonic wires and ring resonators fabricated with deep UV lithography.* IEEE Photonics Technology Letters, 2004. **16**(5): p. 1328-1330.
177. Zhang, L., et al., *Ultralow-Loss Silicon Photonics beyond the Singlemode Regime.* Laser & Photonics Reviews, 2022. **16**(4): p. 2100292.
178. Bian, K., et al., *Acousto-Optic Modulation of a Microring Resonator on Thin-Film AlScN Photonic Platform.* IEEE Photonics Technology Letters, 2025. **37**(16): p. 917-920.
179. Friedman, B., et al., *Measured optical losses of Sc doped AlN waveguides.* Optics Express, 2024. **32**(4): p. 5252-5260.
180. Li, Z., et al., *Demonstration of Integrated AlScN Photonic Devices on 8-Inch Silicon Substrate.* Journal of Lightwave Technology, 2024. **42**(14): p. 4933-4938.
181. Liu, J., et al. *Ferroelectric ScAlN: Epitaxy, Properties, and Emerging Photonic Device Applications*. in *2022 IEEE Photonics Conference (IPC)*. 2022.
182. Xu, T., et al., *Silicon-integrated scandium-doped aluminum nitride electro-optic modulator.* Photonics Research, 2025. **13**(2): p. 477-487.
183. Chen, H., et al., *Study of crystalline defect induced optical scattering loss inside photonic waveguides in UV-visible spectral wavelengths using volume current method.* Optics Express, 2019. **27**(12): p. 17262-17273.

184. Bose, D., et al., *Anneal-free ultra-low loss silicon nitride integrated photonics.* Light: Science & Applications, 2024. **13**(1): p. 156.
185. Zhang, S., et al., *Low-Temperature Sputtered Ultralow-Loss Silicon Nitride for Hybrid Photonic Integration.* Laser & Photonics Reviews, 2024. **18**(4): p. 2300642.
186. Dimitrov, R., et al., *Two-dimensional electron gases in Ga-face and N-face AlGaN/GaN heterostructures grown by plasma-induced molecular beam epitaxy and metalorganic chemical vapor deposition on sapphire.* Journal of Applied Physics, 2000. **87**(7): p. 3375-3380.
187. Keller, S., et al., *Metalorganic chemical vapor deposition of high mobility AlGaN/GaN heterostructures.* Journal of Applied Physics, 1999. **86**(10): p. 5850-5857.
188. Bouzid-Driad, S., et al., *AlGaN/GaN HEMTs on Silicon Substrate With 206-GHz F_{MAX}.* IEEE Electron Device Letters, 2013. **34**(1): p. 36-38.
189. Palacios, T., et al., *High-performance E-mode AlGaN/GaN HEMTs.* IEEE Electron Device Letters, 2006. **27**(6): p. 428-430.
190. Lu, H., et al., *A review of GaN RF devices and power amplifiers for 5G communication applications.* Fundamental Research, 2025. **5**(1): p. 315-331.
191. Nidhi, et al., *Study of Impact of Access Resistance on High-Frequency Performance of AlGaN/GaN HEMTs by Measurements at Low Temperatures.* IEEE Electron Device Letters, 2006. **27**(11): p. 877-880.
192. Yu, E.T., et al., *Measurement of piezoelectrically induced charge in GaN/AlGaN heterostructure field-effect transistors.* Applied Physics Letters, 1997. **71**(19): p. 2794-2796.
193. Cao, Y. and D. Jena, *High-mobility window for two-dimensional electron gases at ultrathin AlN/GaN heterojunctions.* Applied Physics Letters, 2007. **90**(18).
194. Dabiran, A.M., et al., *Very high channel conductivity in low-defect AlN/GaN high electron mobility transistor structures.* Applied Physics Letters, 2008. **93**(8).
195. Holec, D., et al., *Equilibrium critical thickness for misfit dislocations in III-nitrides.* Journal of Applied Physics, 2008. **104**(12).
196. Medjdoub, F., et al. *Can InAlN/GaN be an alternative to high power / high temperature AlGaN/GaN devices?* in *2006 International Electron Devices Meeting*. 2006.
197. Crespo, A., et al., *High-Power Ka-Band Performance of AlInN/GaN HEMT With 9.8-nm-Thin Barrier.* IEEE Electron Device Letters, 2010. **31**(1): p. 2-4.
198. Tirelli, S., et al., *AlInN-Based HEMTs for Large-Signal Operation at 40 GHz.* IEEE Transactions on Electron Devices, 2013. **60**(10): p. 3091-3098.
199. Bernardini, F. and V. Fiorentini, *Nonlinear Behavior of Spontaneous and Piezoelectric Polarization in III–V Nitride Alloys.* physica status solidi (a), 2002. **190**(1): p. 65-73.
200. Casamento, J., et al. *FerroHEMTs: High-Current and High-Speed All-Epitaxial AlScN/GaN Ferroelectric Transistors*. in *2022 International Electron Devices Meeting (IEDM)*. 2022.
201. Green, A.J., et al., *ScAlN/GaN High-Electron-Mobility Transistors With 2.4-A/mm Current Density and 0.67-S/mm Transconductance.* IEEE Electron Device Letters, 2019. **40**(7): p. 1056-1059.
202. Green, A.J., et al., *RF Power Performance of Sc(Al,Ga)N/GaN HEMTs at Ka-Band.* IEEE Electron Device Letters, 2020. **41**(8): p. 1181-1184.
203. Hasan, M.T., et al., *Effect of temperature on the performance of ScAlN/GaN high-electron mobility transistor.* Applied Physics Letters, 2024. **125**(21).

204. Krause, S., et al., *AlScN/GaN HEMTs Grown by Metal-Organic Chemical Vapor Deposition With 8.4 W/mm Output Power and 48 % Power-Added Efficiency at 30 GHz.* IEEE Electron Device Letters, 2023. **44**(1): p. 17-20.
205. Liu, J., et al., *E-mode AlGaN/GaN HEMT with ScAlN/ScN charge trap-coupled ferroelectric gate stacks.* Applied Physics Letters, 2025. **126**(1).
206. Wang, D., et al., *Fully epitaxial, monolithic ScAlN/AlGaN/GaN ferroelectric HEMT.* Applied Physics Letters, 2023. **122**(9).
207. Wang, P., et al., *N-polar ScAlN and HEMTs grown by molecular beam epitaxy.* Applied Physics Letters, 2021. **119**(8).
208. Ambacher, O., et al., *Polarization induced interface and electron sheet charges of pseudomorphic ScAlN/GaN, GaAlN/GaN, InAlN/GaN, and InAlN/InN heterostructures.* Journal of Applied Physics, 2021. **129**(20).
209. Caro, M.A., et al., *Piezoelectric coefficients and spontaneous polarization of ScAlN.* Journal of Physics: Condensed Matter, 2015. **27**(24): p. 245901.
210. Dinh, D.V., et al., *Lattice parameters of $Sc_xAl_{1-x}N$ layers grown on GaN(0001) by plasma-assisted molecular beam epitaxy.* Applied Physics Letters, 2023. **122**(15).
211. Liu, J., et al., *UWBG ferroelectric ScAlN/AlGaN high-electron mobility transistor.* Applied Physics Letters, 2025. **126**(25).
212. Si, M., et al., *BEOL Compatible Indium-Tin-Oxide Transistors: Switching of Ultrahigh-Density 2-D Electron Gas Over 0.8 × 10^{14}/cm2 at Oxide/Oxide Interface by the Change of Ferroelectric Polarization.* IEEE Transactions on Electron Devices, 2021. **68**(7): p. 3195-3199.
213. Ye, H., et al., *ScAlInN/GaN heterostructures grown by molecular beam epitaxy.* Applied Physics Letters, 2024. **125**(12).
214. Zhang, J., et al., *High-temperature memory devices based on ferroelectric ScAlN/AlGaN/GaN high-electron-mobility transistors.* Device, 2025. **3**(9).
215. Wang, J., et al., *Unveiling interfacial dead layer in wurtzite ferroelectrics.* Nature Communications, 2025. **16**(1): p. 6069.
216. Wang, R., et al., *Composition-Graded Nitride Ferroelectrics Based Multi-Level Non-Volatile Memory for Neuromorphic Computing.* Advanced Materials, 2025. **37**(5): p. 2414805.
217. Jin, E.N., et al., *Band Alignment of $Sc_xAl_{1-x}N$/GaN Heterojunctions.* ACS Applied Materials & Interfaces, 2020. **12**(46): p. 52192-52200.
218. Waldrop, J.R. and R.W. Grant, *Measurement of AlN/GaN (0001) heterojunction band offsets by x-ray photoemission spectroscopy.* Applied Physics Letters, 1996. **68**(20): p. 2879-2881.
219. Casamento, J., et al., *Transport properties of polarization-induced 2D electron gases in epitaxial AlScN/GaN heterojunctions.* Applied Physics Letters, 2022. **121**(19).
220. Hardy, M.T., et al., *Epitaxial ScAlN grown by molecular beam epitaxy on GaN and SiC substrates.* Applied Physics Letters, 2017. **110**(16).
221. Streicher, I., et al., *Effect of AlN and AlGaN Interlayers on AlScN/GaN Heterostructures Grown by Metal–Organic Chemical Vapor Deposition.* Crystal Growth & Design, 2023. **23**(2): p. 782-791.
222. Li, H., et al., *Improved properties of high-Al-composition AlGaN/GaN high electron mobility transistor structures with thin GaN cap layers.* Japanese Journal of Applied Physics, 2014. **53**(9): p. 095504.

223. Waltereit, P., et al., *Impact of GaN cap thickness on optical, electrical, and device properties in AlGaN/GaN high electron mobility transistor structures.* Journal of Applied Physics, 2009. **106**(2).
224. Zanato, D., et al., *The effect of interface-roughness and dislocation scattering on low temperature mobility of 2D electron gas in GaN/AlGaN.* Semiconductor Science and Technology, 2004. **19**(3): p. 427.
225. Ridley, B.K., B.E. Foutz, and L.F. Eastman, *Mobility of electrons in bulk GaN and$Al_xGa_{1-x}N$/GaN heterostructures.* Physical Review B, 2000. **61**(24): p. 16862-16869.
226. Frayssinet, E., et al., *High electron mobility in AlGaN/GaN heterostructures grown on bulk GaN substrates.* Applied Physics Letters, 2000. **77**(16): p. 2551-2553.
227. Smorchkova, I.P., et al., *Polarization-induced charge and electron mobility in AlGaN/GaN heterostructures grown by plasma-assisted molecular-beam epitaxy.* Journal of Applied Physics, 1999. **86**(8): p. 4520-4526.
228. Cheng, J., et al., *Breakdown Voltage Enhancement in ScAlN/GaN High-Electron-Mobility Transistors by High-k Bismuth Zinc Niobate Oxide.* IEEE Transactions on Electron Devices, 2021. **68**(7): p. 3333-3338.
229. Engel, Z., et al., *Overcoming metal-rich surface chemistry limitations of ScAlN for high electrical performance heterostructures.* Journal of Applied Physics, 2022. **132**(18).
230. Frei, K., et al., *Investigation of growth parameters for ScAlN-barrier HEMT structures by plasma-assisted MBE.* Japanese Journal of Applied Physics, 2019. **58**(SC): p. SC1045.
231. Ligl, J., et al., *Metalorganic chemical vapor phase deposition of AlScN/GaN heterostructures.* Journal of Applied Physics, 2020. **127**(19).
232. Manz, C., et al., *Improved AlScN/GaN heterostructures grown by metal-organic chemical vapor deposition.* Semiconductor Science and Technology, 2021. **36**(3): p. 034003.
233. Tahhan, M.B., et al., *Passivation Schemes for ScAlN-Barrier mm-Wave High Electron Mobility Transistors.* IEEE Transactions on Electron Devices, 2022. **69**(3): p. 962-967.
234. Yin, Y., et al., *Boosting the two-dimensional electron gas density of $Al_{0.20}Ga_{0.80}N$/GaN heterostructures by regrowth of an epitaxial $Sc_{0.18}Al_{0.82}N$ layer.* Applied Physics Letters, 2024. **125**(19).
235. Behbahani, A. and K. Semega, *Sensing Challenges for Controls and PHM in the Hostile Operating Conditions of Modern Turbine Engine*, in *44th AIAA/ASME/SAE/ASEE Joint Propulsion Conference & Exhibit*. 2008, American Institute of Aeronautics and Astronautics.
236. Blosser, M.L., *Fundamental Modeling and Thermal Performance Issues for Metallic Thermal Protection System Concept.* Journal of Spacecraft and Rockets, 2004. **41**(2): p. 195-206.
237. Johnson, R.W., et al., *The changing automotive environment: high-temperature electronics.* IEEE Transactions on Electronics Packaging Manufacturing, 2004. **27**(3): p. 164-176.
238. Neudeck, P.G., R.S. Okojie, and C. Liang-Yu, *High-temperature electronics—a role for wide bandgap semiconductors?* Proceedings of the IEEE, 2002. **90**(6): p. 1065-1076.
239. Neudeck, P.G., et al., *Demonstration of 4H-SiC Digital Integrated Circuits Above 800 °C.* IEEE Electron Device Letters, 2017. **38**(8): p. 1082-1085.
240. Carey, P.H., et al., *Extreme Temperature Operation of Ultra-Wide Bandgap AlGaN High Electron Mobility Transistors.* IEEE Transactions on Semiconductor Manufacturing, 2019. **32**(4): p. 473-477.

241. Hassan, A., Y. Savaria, and M. Sawan, *GaN Integration Technology, an Ideal Candidate for High-Temperature Applications: A Review.* IEEE Access, 2018. **6**: p. 78790-78802.
242. Yoder, M.N., *Wide bandgap semiconductor materials and devices.* IEEE Transactions on Electron Devices, 1996. **43**(10): p. 1633-1636.
243. Hoo Teo, K., et al., *Emerging GaN technologies for power, RF, digital, and quantum computing applications: Recent advances and prospects.* Journal of Applied Physics, 2021. **130**(16).
244. Meneghini, M., et al., *GaN-based power devices: Physics, reliability, and perspectives.* Journal of Applied Physics, 2021. **130**(18).
245. Islam, A.E., et al., *Effect of High Temperature on the Performance of AlGaN/GaN T-Gate High-Electron Mobility Transistors With ~140-nm Gate Length.* IEEE Transactions on Electron Devices, 2024. **71**(3): p. 1805-1811.
246. Maier, D., et al., *InAlN/GaN HEMTs for Operation in the 1000 °C Regime: A First Experiment.* IEEE Electron Device Letters, 2012. **33**(7): p. 985-987.
247. Lee, H., et al., *Stable High Temperature Operation of p-GaN Gate HEMT With Etch-Stop Layer.* IEEE Electron Device Letters, 2024. **45**(3): p. 312-315.
248. Kargarrazi, S., et al., *Stable Operation of AlGaN/GaN HEMTs for 25 h at 400°C in air.* IEEE Journal of the Electron Devices Society, 2019. **7**: p. 931-935.
249. Hatano, M., et al., *Superior DC and RF Performance of AlGaN-Channel HEMT at High Temperatures.* IEICE Transactions on Electronics, 2012. **E95.C**(8): p. 1332-1336.
250. Mikolajick, T., et al., *Next generation ferroelectric materials for semiconductor process integration and their applications.* Journal of Applied Physics, 2021. **129**(10).
251. Ambacher, O., et al., *Wurtzite ScAlN, InAlN, and GaAlN crystals, a comparison of structural, elastic, dielectric, and piezoelectric properties.* Journal of Applied Physics, 2021. **130**(4).
252. Islam, M.R., et al., *On the exceptional temperature stability of ferroelectric $Al_{1-x}Sc_xN$ thin films.* Applied Physics Letters, 2021. **118**(23).
253. Jönsson, A., et al., *Ferroelectric-Gated $HfZrO_2$/AlGaN/GaN High-Electron-Mobility Transistors with Regrown Contacts for Radio Frequency and Millimeter-Wave Switch Applications.* physica status solidi (a), 2024. **221**(13): p. 2300654.
254. Guo, J., et al., *MBE-Regrown Ohmics in InAlN HEMTs With a Regrowth Interface Resistance of 0.05 Ω·mm.* IEEE Electron Device Letters, 2012. **33**(4): p. 525-527.
255. Suria, A.J., et al., *DC characteristics of ALD-grown Al_2O_3/AlGaN/GaN MIS-HEMTs and HEMTs at 600 °C in air.* Semiconductor Science and Technology, 2016. **31**(11): p. 115017.
256. Khan, M.A., et al., *Insulating gate III-N heterostructure field-effect transistors for high-power microwave and switching applications.* IEEE Transactions on Microwave Theory and Techniques, 2003. **51**(2): p. 624-633.
257. Yafune, N., et al., *AlN/AlGaN HEMTs on AlN substrate for stable high-temperature operation.* Electronics Letters, 2014. **50**(3): p. 211-212.
258. Lee, H., et al., *High Temperature Operation of E-Mode and D-Mode AlGaN/GaN MIS-HEMTs With Recessed Gates.* IEEE Journal of the Electron Devices Society, 2023. **11**: p. 167-173.
259. Yuan, M., et al. *High Temperature Robustness of Enhancement-Mode p-GaN-Gated AlGaN/GaN HEMT Technology*. in *2022 IEEE 9th Workshop on Wide Bandgap Power Devices & Applications (WiPDA)*. 2022.

260. Niroula, J., et al., *High temperature stability of regrown and alloyed Ohmic contacts to AlGaN/GaN heterostructure up to 500 °C.* Applied Physics Letters, 2024. **124**(20).
261. Xie, Q., et al., *Device and material investigations of GaN enhancement-mode transistors for Venus and harsh environments.* Applied Physics Letters, 2024. **124**(17).
262. Khan, A.I., A. Keshavarzi, and S. Datta, *The future of ferroelectric field-effect transistor technology.* Nature Electronics, 2020. **3**(10): p. 588-597.
263. Salahuddin, S., K. Ni, and S. Datta, *The era of hyper-scaling in electronics.* Nature Electronics, 2018. **1**(8): p. 442-450.
264. Kim, K.-H., et al., *Wurtzite and fluorite ferroelectric materials for electronic memory.* Nature Nanotechnology, 2023. **18**(5): p. 422-441.
265. Böscke, T.S., et al., *Ferroelectricity in hafnium oxide thin films.* Applied Physics Letters, 2011. **99**(10).
266. Noheda, B., P. Nukala, and M. Acuautla, *Lessons from hafnium dioxide-based ferroelectrics.* Nature Materials, 2023. **22**(5): p. 562-569.
267. Pešić, M., et al., *Physical Mechanisms behind the Field-Cycling Behavior of HfO_2-Based Ferroelectric Capacitors.* Advanced Functional Materials, 2016. **26**(25): p. 4601-4612.
268. Pradhan, D.K., et al., *A scalable ferroelectric non-volatile memory operating at 600 °C.* Nature Electronics, 2024. **7**(5): p. 348-355.
269. Kim, K.-H., et al., *Scalable CMOS back-end-of-line-compatible AlScN/two-dimensional channel ferroelectric field-effect transistors.* Nature Nanotechnology, 2023. **18**(9): p. 1044-1050.
270. Mondal, S., et al., *ScAlN-Based ITO Channel Ferroelectric Field-Effect Transistors With Large Memory Window.* IEEE Transactions on Electron Devices, 2023. **70**(9): p. 4618-4621.
271. Jena, D., et al., *The new nitrides: layered, ferroelectric, magnetic, metallic and superconducting nitrides to boost the GaN photonics and electronics eco-system.* Japanese Journal of Applied Physics, 2019. **58**(SC): p. SC0801.
272. Yang, J.Y., et al., *Pulsed E-/D-Mode Switchable GaN HEMTs With a Ferroelectric AlScN Gate Dielectric.* IEEE Electron Device Letters, 2023. **44**(8): p. 1260-1263.
273. Zhao, Z., et al., *The incorporation of AlScN ferroelectric gate dielectric in AlGaN/GaN-HEMT with polarization-modulated threshold voltage.* Applied Physics Express, 2023. **16**(3): p. 031002.
274. Han, S.W., et al., *GaN based negative capacitance heterojunction field-effect transistors with <30 mV/dec subthreshold slope for steep switching operation.* Results in Physics, 2020. **16**: p. 102950.
275. Wu, C., et al., *$Hf_{0.5}Zr_{0.5}O_2$-Based Ferroelectric Gate HEMTs With Large Threshold Voltage Tuning Range.* IEEE Electron Device Letters, 2020. **41**(3): p. 337-340.
276. Yang, J.Y., et al., *Reconfigurable Radio-Frequency High-Electron Mobility Transistors via Ferroelectric-Based Gallium Nitride Heterostructure.* Advanced Electronic Materials, 2022. **8**(9): p. 2101406.
277. Zhu, J., et al., *Ferroelectric Gate AlGaN/GaN E-Mode HEMTs With High Transport and Sub-Threshold Performance.* IEEE Electron Device Letters, 2018. **39**(1): p. 79-82.
278. Chen, S.-M., et al., *GaN high electron mobility transistors (HEMTs) with self-upward-polarized AlScN gate dielectrics toward enhancement-mode operation.* Japanese Journal of Applied Physics, 2022. **61**(SH): p. SH1007.

279. Döring, P., et al., *Voltage-margin limiting mechanisms of AlScN-based HEMTs.* Applied Physics Letters, 2023. **123**(3).
280. Li, Z., et al., *A 3D Vertical-Channel Ferroelectric/Anti-Ferroelectric FET With Indium Oxide.* IEEE Electron Device Letters, 2022. **43**(8): p. 1227-1230.
281. Jeong, S., et al., *All-Sputter-Deposited $Hf_{0.5}Zr_{0.5}O_2$ Double-Gate Ferroelectric Thin-Film Transistor With Amorphous Indium–Gallium–Zinc Oxide Channel.* IEEE Electron Device Letters, 2023. **44**(5): p. 749-752.
282. Aabrar, K.A., et al. *BEOL Compatible Superlattice FerroFET-based High Precision Analog Weight Cell with Superior Linearity and Symmetry*. in *2021 IEEE International Electron Devices Meeting (IEDM)*. 2021.
283. Kim, I.J., M.K. Kim, and J.S. Lee, *Design Strategy to Improve Memory Window in Ferroelectric Transistors With Oxide Semiconductor Channel.* IEEE Electron Device Letters, 2023. **44**(2): p. 249-252.
284. Luo, C., et al., *Ferroelectric $Hf_{0.5}Zr_{0.5}O_2$-gated synaptic transistors with large conductance dynamic range and multilevel states.* Science China Materials, 2023. **66**(6): p. 2372-2382.
285. Yang, J.Y., et al., *Ferroelectric α-In_2Se_3 Wrapped-Gate β-Ga_2O_3 Field-Effect Transistors for Dynamic Threshold Voltage Control.* Advanced Electronic Materials, 2021. **7**(8): p. 2100306.
286. Chen, C.K., et al. *First Demonstration of Ultra-low Dit Top-Gated Ferroelectric Oxide-Semiconductor Memtransistor with Record Performance by Channel Defect Self-Compensation Effect for BEOL-Compatible Non-Volatile Logic Switch*. in *2022 International Electron Devices Meeting (IEDM)*. 2022.
287. Saitoh, M., et al. *HfO2-based FeFET and FTJ for Ferroelectric-Memory Centric 3D LSI towards Low-Power and High-Density Storage and AI Applications*. in *2020 IEEE International Electron Devices Meeting (IEDM)*. 2020.
288. Lin, Z., et al. *High-Peformance BEOL-Compatible Atomic-Layer-Deposited In_2O_3 Fe-FETs Enabled by Channel Length Scaling down to 7 nm: Achieving Performance Enhancement with Large Memory Window of 2.2 V, Long Retention > 10 years and High Endurance > 10^8 Cycles*. in *2021 IEEE International Electron Devices Meeting (IEDM)*. 2021.
289. Choi, S.-N., S.-E. Moon, and S.-M. Yoon, *Impact of oxide gate electrode for ferroelectric field-effect transistors with metal-ferroelectric-metal-insulator-semiconductor gate stack using undoped HfO_2 thin films prepared by atomic layer deposition.* Nanotechnology, 2021. **32**(8): p. 085709.
290. Hasan, M.M., et al., *Improvement of Amorphous InGaZnO Thin-Film Transistor With Ferroelectric ZrO_x/HfZrO Gate Insulator by 2 Step Sequential Ar/O_2 Treatment.* IEEE Electron Device Letters, 2022. **43**(5): p. 725-728.
291. Persson, A.E.O., et al., *Integration of Ferroelectric $Hf_xZr_{1-x}O_2$ on Vertical III-V Nanowire Gate-All-Around FETs on Silicon.* IEEE Electron Device Letters, 2022. **43**(6): p. 854-857.
292. Mo, F., et al., *Low-Voltage Operating Ferroelectric FET with Ultrathin IGZO Channel for High-Density Memory Application.* IEEE Journal of the Electron Devices Society, 2020. **8**: p. 717-723.
293. Kim, M.-K., I.-J. Kim, and J.-S. Lee, *Oxide semiconductor-based ferroelectric thin-film transistors for advanced neuromorphic computing.* Applied Physics Letters, 2021. **118**(3).

294. Sun, C., et al., *Temperature-Dependent Operation of InGaZnO Ferroelectric Thin-Film Transistors With a Metal-Ferroelectric-Metal-Insulator- Semiconductor Structure.* IEEE Electron Device Letters, 2021. **42**(12): p. 1786-1789.
295. Liao, J., et al., *Van der Waals Ferroelectric Semiconductor Field Effect Transistor for In-Memory Computing.* ACS Nano, 2023. **17**(6): p. 6095-6102.
296. Li, Q., et al., *High-performance ferroelectric field-effect transistors with ultra-thin indium tin oxide channels for flexible and transparent electronics.* Nature Communications, 2024. **15**(1): p. 2686.
297. Kim, W.-S., et al., *Abnormal behavior with hump characteristics in current stressed a-InGaZnO thin film transistors.* Solid-State Electronics, 2017. **137**: p. 22-28.
298. Mativenga, M., M. Seok, and J. Jang, *Gate bias-stress induced hump-effect in transfer characteristics of amorphous-indium-galium-zinc-oxide thin-fim transistors with various channel widths.* Applied Physics Letters, 2011. **99**(12).
299. Tan, A.J., et al., *Ferroelectric HfO_2 Memory Transistors With High-κ Interfacial Layer and Write Endurance Exceeding 10^{10} Cycles.* IEEE Electron Device Letters, 2021. **42**(7): p. 994-997.
300. Wang, X.D., et al., *The Study of Self-Heating and Hot-Electron Effects for AlGaN/GaN Double-Channel HEMTs.* IEEE Transactions on Electron Devices, 2012. **59**(5): p. 1393-1401.
301. Gaska, R., et al., *Self-heating in high-power AlGaN-GaN HFETs.* IEEE Electron Device Letters, 1998. **19**(3): p. 89-91.
302. Hwang, I., et al., *Impact of Channel Hot Electrons on Current Collapse in AlGaN/GaN HEMTs.* IEEE Electron Device Letters, 2013. **34**(12): p. 1494-1496.
303. Yang, F., et al., *The Impact of Hot Electrons and Self-Heating During Hard-Switching in AlGaN/GaN HEMTs.* IEEE Transactions on Electron Devices, 2020. **67**(3): p. 869-874.
304. Felbinger, J.G., et al., *Comparison of GaN HEMTs on Diamond and SiC Substrates.* IEEE Electron Device Letters, 2007. **28**(11): p. 948-950.
305. Liao, P.Y., et al., *Transient Thermal and Electrical Co-Optimization of BEOL Top-Gated ALD In_2O_3 FETs Toward Monolithic 3-D Integration.* IEEE Transactions on Electron Devices, 2023. **70**(4): p. 2052-2058.
306. Zhang, Y., et al., *GaN FinFETs and trigate devices for power and RF applications: review and perspective.* Semiconductor Science and Technology, 2021. **36**(5): p. 054001.
307. Liao, P.Y., et al., *Realization of Maximum 2 A/mm Drain Current on Top-Gate Atomic-Layer-Thin Indium Oxide Transistors by Thermal Engineering.* IEEE Transactions on Electron Devices, 2022. **69**(1): p. 147-151.
308. Wang, P., et al., *Investigating Ferroelectric Minor Loop Dynamics and History Effect—Part I: Device Characterization.* IEEE Transactions on Electron Devices, 2020. **67**(9): p. 3592-3597.
309. Lin, W., et al., *Oxygen-assisted synthesis of hBN films for resistive random access memories.* Applied Physics Letters, 2019. **115**(7).
310. Chiu, F.-C., *A Review on Conduction Mechanisms in Dielectric Films.* Advances in Materials Science and Engineering, 2014. **2014**(1): p. 578168.
311. Wu, Y., C.-Y. Chen, and J.A. del Alamo, *Electrical and structural degradation of GaN high electron mobility transistors under high-power and high-temperature Direct Current stress.* Journal of Applied Physics, 2015. **117**(2).

312. Gong, N. and T.P. Ma, *Why Is FE–HfO_2 More Suitable Than PZT or SBT for Scaled Nonvolatile 1-T Memory Cell? A Retention Perspective.* IEEE Electron Device Letters, 2016. **37**(9): p. 1123-1126.
313. Gong, N. and T.P. Ma, *A Study of Endurance Issues in HfO_2-Based Ferroelectric Field Effect Transistors: Charge Trapping and Trap Generation.* IEEE Electron Device Letters, 2018. **39**(1): p. 15-18.
314. Ma, T.P. and H. Jin-Ping, *Why is nonvolatile ferroelectric memory field-effect transistor still elusive?* IEEE Electron Device Letters, 2002. **23**(7): p. 386-388.
315. Baliga, B.J., *Gallium nitride devices for power electronic applications.* Semiconductor Science and Technology, 2013. **28**(7): p. 074011.
316. Chiamori, H., et al., *Characterization of gallium nitride microsystems within radiation and high-temperature environments*. SPIE MOEMS-MEMS. Vol. 8975. 2014: SPIE.
317. Zheng, Z., et al., *Gallium nitride-based complementary logic integrated circuits.* Nature Electronics, 2021. **4**(8): p. 595-603.
318. Eisner, S.R., et al. *Extended Exposure of Gallium Nitride Heterostructure Devices to a Simulated Venus Environment*. in *2021 IEEE Aerospace Conference (50100)*. 2021.
319. Lv, G., et al., *A Dual-Band GaN MMIC Power Amplifier With Hybrid Operating Modes for 5G Application.* IEEE Microwave and Wireless Components Letters, 2019. **29**(3): p. 228-230.
320. Parikh, P., et al., *650 Volt GaN Commercialization Reaches Automotive Standards.* ECS Transactions, 2017. **80**(7): p. 17.
321. Scott, M.J., et al., *Merits of gallium nitride based power conversion.* Semiconductor Science and Technology, 2013. **28**(7): p. 074013.
322. Saito, W., et al., *Recessed-gate structure approach toward normally off high-Voltage AlGaN/GaN HEMT for power electronics applications.* IEEE Transactions on Electron Devices, 2006. **53**(2): p. 356-362.
323. Cai, Y., et al., *High-performance enhancement-mode AlGaN/GaN HEMTs using fluoride-based plasma treatment.* IEEE Electron Device Letters, 2005. **26**(7): p. 435-437.
324. Hwang, I., et al. *1.6kV, 2.9 mΩ cm^2 normally-off p-GaN HEMT device*. in *2012 24th International Symposium on Power Semiconductor Devices and ICs*. 2012.
325. Hwang, I., et al., *p-GaN Gate HEMTs With Tungsten Gate Metal for High Threshold Voltage and Low Gate Current.* IEEE Electron Device Letters, 2013. **34**(2): p. 202-204.
326. Anderson, T.J., et al., *Characterization of Recessed-Gate AlGaN/GaN HEMTs as a Function of Etch Depth.* Journal of Electronic Materials, 2010. **39**(5): p. 478-481.
327. Ťapajna, M., et al., *Gate Reliability Investigation in Normally-Off p-Type-GaN Cap/AlGaN/GaN HEMTs Under Forward Bias Stress.* IEEE Electron Device Letters, 2016. **37**(4): p. 385-388.
328. Albany, F., et al., *Stability of the threshold voltage in fluorine-implanted normally-off AlN/GaN HEMTs co-integrated with commercial normally-on GaN HEMT technology.* Microelectronics Reliability, 2021. **126**: p. 114291.
329. Favero, D., et al., *Trade-off between gate leakage current and threshold voltage stability in power HEMTs during ON-state and OFF-state stress.* Microelectronics Reliability, 2023. **150**: p. 115129.
330. Hasegawa, F., et al., *Proposal and simulated results of a normally off AlGaN/GaN HFET structure with a charged floating gate.* physica status solidi c, 2009. **6**(S2): p. S940-S943.

331. Lee, B., et al., *Normally-off AlGaN/GaN MOSHFET using ALD SiO_2 tunnel dielectric and ALD HfO_2 charge storage layer for power device application.* physica status solidi c, 2012. **9**(3-4): p. 868-870.
332. Wu, J.S., et al., *Hf-Based and Zr-Based Charge Trapping Layer Engineering for E-Mode GaN MIS-HEMT Using Ferroelectric Charge Trap Gate Stack.* IEEE Journal of the Electron Devices Society, 2022. **10**: p. 525-531.
333. Wu, C.H., et al., *High-Performance Normally-OFF GaN MIS-HEMTs Using Hybrid Ferroelectric Charge Trap Gate Stack (FEG-HEMT) for Power Device Applications.* IEEE Electron Device Letters, 2018. **39**(7): p. 991-994.
334. Casamento, J., et al., *Perspectives and progress on wurtzite ferroelectrics: Synthesis, characterization, theory, and device applications.* Applied Physics Letters, 2024. **124**(8).
335. Gall, D., et al., *Growth of poly- and single-crystal ScN on MgO(001): Role of low-energy N2+ irradiation in determining texture, microstructure evolution, and mechanical properties.* Journal of Applied Physics, 1998. **84**(11): p. 6034-6041.
336. Bai, X., D.M. Hill, and M.E. Kordesch, *IIIB- Nitride Semiconductors for High Temperature Electronic Applications.* MRS Proceedings, 1999. **572**: p. 529.
337. Hájek, B., V. Brožek, and P.H. Duvigneaud, *Dilatation thermique des produits d'oxydation du scandium.* Journal of the Less Common Metals, 1973. **33**(3): p. 385-386.
338. Su, M., C. Chen, and S. Rajan, *Prospects for the application of GaN power devices in hybrid electric vehicle drive systems.* Semiconductor Science and Technology, 2013. **28**(7): p. 074012.
339. Lee, C.T., et al., *GaN-Based Enhancement-Mode Metal–Oxide–Semiconductor High-Electron Mobility Transistors Using $LiNbO_3$ Ferroelectric Insulator on Gate-Recessed Structure.* IEEE Transactions on Electron Devices, 2015. **62**(8): p. 2481-2487.
340. Taur, Y. and T.H. Ning, *Fundamentals of modern VLSI devices*. 2021: Cambridge university press.
341. Drury, D., et al., *High-Temperature Ferroelectric Behavior of $Al_{0.7}Sc_{0.3}N$.* Micromachines, 2022. **13**(6): p. 887.
342. Baca, A.G., et al., *Al-rich AlGaN based transistors.* Journal of Vacuum Science & Technology A, 2020. **38**(2).
343. Klein, B.A., A.A. Allerman, and A.M. Armstrong, *Al-rich AlGaN high electron mobility transistor gate metallization study up to 600 °C in air.* Applied Physics Letters, 2024. **124**(10).
344. Tsao, J.Y., et al., *Ultrawide-Bandgap Semiconductors: Research Opportunities and Challenges.* Advanced Electronic Materials, 2018. **4**(1): p. 1600501.
345. Muhtadi, S., et al., *Selective area deposited n-$Al_{0.5}Ga_{0.5}N$ channel field effect transistors with high solar-blind ultraviolet photo-responsivity.* Applied Physics Letters, 2017. **110**(17).
346. Razzak, T., et al., *$BaTiO_3/Al_{0.58}Ga_{0.42}N$ lateral heterojunction diodes with breakdown field exceeding 8 MV/cm.* Applied Physics Letters, 2020. **116**(2).
347. Nanjo, T., et al., *First Operation of AlGaN Channel High Electron Mobility Transistors.* Applied Physics Express, 2008. **1**(1): p. 011101.
348. Gaevski, M., et al., *Ultrawide bandgap $Al_xGa_{1-x}N$ channel heterostructure field transistors with drain currents exceeding 1.3 A mm^{-1}.* Applied Physics Express, 2020. **13**(9): p. 094002.

349. Maeda, R., et al., *AlN/$Al_{0.5}Ga_{0.5}N$ HEMTs with heavily Si-doped degenerate GaN contacts prepared via pulsed sputtering.* Applied Physics Express, 2022. **15**(3): p. 031002.
350. Maeda, R., et al., *Temperature-Dependent Characteristics of AlN/$Al_{0.5}Ga_{0.5}N$ High Electron Mobility Transistors with Highly Degenerate n-Type GaN Regrown Ohmic Contacts.* physica status solidi (a), 2024. **221**(21): p. 2300848.
351. Zhu, Y., et al., *Heterostructure and interfacial engineering for low-resistance contacts to ultra-wide bandgap AlGaN.* Applied Physics Letters, 2025. **126**(6).
352. Tokuda, H., et al., *High Al Composition AlGaN-Channel High-Electron-Mobility Transistor on AlN Substrate.* Applied Physics Express, 2010. **3**(12): p. 121003.
353. Kumar, J.S.R., et al., *Investigations of ScAlN/AlGaN split barrier inspired high electron mobility transistor.* AIP Conference Proceedings, 2023. **2901**(1).
354. Nomoto, K., et al., *AlScN/GaN HEMTs with 4 A/mm on-current and maximum oscillation frequency >130 GHz.* Applied Physics Express, 2025. **18**(1): p. 016506.
355. Miller, S.L. and P.J. McWhorter, *Physics of the ferroelectric nonvolatile memory field effect transistor.* Journal of Applied Physics, 1992. **72**(12): p. 5999-6010.
356. Chen, L., et al., *Hetero-integration of quasi two-dimensional $PbZr_{0.2}Ti_{0.8}O_3$ on AlGaN/GaN HEMT and non-volatile modulation of two-dimensional electron gas.* Applied Physics Letters, 2019. **115**(19).
357. Mizutani, T., et al., *A study on current collapse in AlGaN/GaN HEMTs induced by bias stress.* IEEE Transactions on Electron Devices, 2003. **50**(10): p. 2015-2020.
358. Rowberg, A.J.E., et al., *Structural, electronic, and polarization properties of YN and LaN.* Physical Review Materials, 2021. **5**(9): p. 094602.
359. Lee, D.S., et al., *Nanowire Channel InAlN/GaN HEMTs With High Linearity of g_m and f_T.* IEEE Electron Device Letters, 2013. **34**(8): p. 969-971.
360. Chen, Y.-L., et al., *On-state performance enhancement of AlGaN/GaN Fin-HEMTs by using arcuate sidewalls.* Applied Physics Letters, 2024. **125**(6).